

COMPUTATIONAL STUDY OF THE DEPOSITION OF METAL-OXIDE THIN FILMS ON  
STRONTIUM TITANATE: MORPHOLOGY AND GROWTH MODES

By

JENNIFER LYNNE WOHLWEND

A DISSERTATION PRESENTED TO THE GRADUATE SCHOOL  
OF THE UNIVERSITY OF FLORIDA IN PARTIAL FULFILLMENT  
OF THE REQUIREMENTS FOR THE DEGREE OF  
DOCTOR OF PHILOSOPHY

UNIVERSITY OF FLORIDA

2009

1

© 2009 Jennifer Lynne Wohlwend

To my family

## ACKNOWLEDGMENTS

I wish to thank my graduate advisor and mentor, Prof. Susan B. Sinnott who has given her kind guidance and advice throughout my time here. Dr. Sinnott has been a source of strength during difficult times and life changing events. I also wish to thank Dr. Simon Phillpot for his advice and for always having an open door when I struggled with writing code.

Many thanks to the past and present members of the Computational Focus Group for their kindness and friendship. I came to UF without knowledge of coding or simulation and my fellow group members were always willing to answer questions and offer support. Specifically to Rakesh Behera, who has been a never ending resource. I also thank Cosima Boswell for her contributions to this work. Finally, I would like to thank the professors at Clemson University in the ceramic and materials science and engineering department who laid the foundation and gave me inspiration to continue my education.

I express my deepest thanks to my family. My parents, Gregory and Katherine McKillip, made this accomplishment possible and have always been by my side. I thank my husband, Michael Wohlwend, for all he has given me. I am forever grateful for his never-ending support especially during the past year.

# TABLE OF CONTENTS

	<u>page</u>
ACKNOWLEDGMENTS.....	4
LIST OF TABLES.....	7
LIST OF FIGURES .....	8
ABSTRACT .....	11
CHAPTER	
1 INTRODUCTION.....	13
General Introduction .....	13
Strontium Titanate and Component Oxides Structure and Applications.....	13
Experimental Strontium Titanate and Component Oxides Deposition and Growth.....	17
Computational Studies of Deposition and Growth .....	20
Growth: Effects of Mobility and Diffusion .....	23
2 COMPUTATIONAL METHODS .....	27
Molecular Dynamics .....	27
Periodic Boundary Conditions.....	28
Velocity Rescaling Thermostat.....	29
Gear 5 <sup>th</sup> Order Predictor-Corrector .....	30
Interatomic Potential.....	32
Buckingham potential .....	32
Coulomb potential .....	33
Temperature Accelerated Dynamics.....	36
3 STRONTIUM OXIDE AND TITANIUM DIOXIDE THIN FILM DEPOSITION ON STRONTIUM TITANATE .....	41
Simulation Set-up.....	41
Results.....	42
Strontium Oxide Deposition .....	42
Titanium Dioxide Deposition.....	45
Discussion.....	46
Conclusions .....	52
4 PARTICULATE DEPOSITION OF HOMOEPITAXIAL STRONTIUM TITANATE THIN FILMS .....	54
Simulation Set-up.....	54
Results.....	55

Alternating Particle Deposition .....	55
Alternating Monolayer Deposition.....	59
Discussion.....	61
Conclusions .....	64
5 STRONTIUM TITANATE CLUSTER DEPOSITION .....	65
Simulation Set-up.....	65
Results.....	68
Discussion.....	77
Conclusions .....	78
6 TEMPERATURE ACCELERATED DYNAMICS .....	79
Simulation Set-up.....	79
Results.....	82
Discussion.....	87
Conclusions .....	89
7 GENERAL CONCLUSIONS .....	91
APPENDIX: ANALYSIS CODES .....	93
REFERENCE LIST .....	107
BIOGRAPHICAL SKETCH .....	119

LIST OF TABLES

<u>Table</u>		<u>page</u>
2-1	Parameters used in the Buckingham and Coulombic potentials. ....	34
2-2	Comparison of calculated and experimental structure and elastic properties for SrTiO <sub>3</sub> . ....	35
2-3	Comparison of the results of current calculations, experimental data, and previous calculations for the structural properties of anatase and rutile TiO <sub>2</sub> , and rocksalt SrO. ....	35
3-1	Nearest neighbor distances of Ti with O for bulk STO, rutile, and anatase. ....	46
3-2	Comparison of the works of adhesion of anatase TiO <sub>2</sub> , rutile TiO <sub>2</sub> , and rocksalt SrO, respectively, on STO. ....	51
3-3	Diffusion coefficients (D) of an SrO or TiO <sub>2</sub> particle on each STO termination ....	53
5-1	Average Ti-O bonding in STO clusters compared to bulk STO. ....	67
5-2	Cluster deposition schemes investigated. ....	68

## LIST OF FIGURES

<u>Figure</u>	<u>page</u>
1-1 SrTiO <sub>3</sub> illustrating the alternating SrO/TiO <sub>2</sub> planes. ....	15
1-2 Bulk SrO exhibits a structure similar to the SrO plane in SrTiO <sub>3</sub> with a smaller Sr-O bond.....	16
1-3 TiO <sub>2</sub> polymorphs.....	16
1-4 RHEED oscillations and the corresponding surface coverage.....	24
1-5 Schematic illustration of structures produced by differing growth modes.....	24
1-6 Atomic force microscopy images of SrTiO <sub>3</sub> thin films illustrating different growth modes observed. ....	26
2-1 Schematic of simulation steps.....	27
2-2 Schematic of periodic boundary conditions. ....	28
2-3 STO substrate illustrating thermostat and active regions. ....	29
2-4 Schematic of transition state theory. ....	37
2-5 Schematic illustration of the extrapolation of T <sub>high</sub> time to T <sub>low</sub> time. ....	39
2-6 Flowchart illustrating the temperature accelerated dynamics procedure. ....	40
3-1 SrO layers that are deposited with an incident energy of 1.0 eV/atom on TiO <sub>2</sub> -terminated STO. ....	43
3-2 Sr-O planar pair distribution function for SrO layers on STO.....	44
3-3 Sr-O planar pair distribution function showing an obvious correlation between the STO termination layer and SrO deposited film structure. ....	44
3-4 Sr-O planar pair distribution function showing the second SrO layer grown on TiO <sub>2</sub> -terminated STO corresponding to the first SrO layer grown on the SrO-terminated STO. ....	45
3-5 TiO <sub>2</sub> particle deposition.....	47
3-6 Ti-O pair distribution function showing the influence of termination layer. ....	48
3-7 Mean square displacement curve for an SrO particle on TiO <sub>2</sub> terminated STO at 973 K showing the adequate linearity needed to calculate the diffusion coefficient from the slope of the curve. ....	53

4-1	Alternating particle deposition .....	56
4-2	Alternating particle deposition metal atom percentages.....	57
4-3	Pair distribution functions for alternating particle deposition.....	58
4-4	Alternating monolayer deposition.....	60
4-5	Metal atom percentages for alternating monolayer deposited films. ....	61
4-6	Pair distribution functions for alternating monolayer deposited films. ....	62
5-1	STO cluster geometries displaying bond-lengths and symmetry.....	67
5-2	Representative snapshots of films deposited on SrO-terminated STO showing layer segregation and order within the first layer. ....	69
5-3	Pair distribution function of the second deposited layer comparing mono- and mixed-size cluster deposition on SrO-terminated STO illustrating the similar structural order between the two deposition methods. ....	70
5-4	Percentage of metal atoms in the first two deposited layers on SrO-terminated STO. ....	71
5-5	Representative snapshots of films deposited on TiO <sub>2</sub> -terminated STO showing layer segregation and order within layers one and two shown in the lower figures. ....	72
5-6	Pair distribution function of the second deposited layer comparing mono- and mixed-size cluster deposition on TiO <sub>2</sub> -terminated STO illustrating the similar structural order between the two deposition methods. ....	73
5-7	Percentages of metal atoms in the first two deposited layers on TiO <sub>2</sub> -terminated STO.....	74
5-8	First layer of each film deposited on TiO <sub>2</sub> termination illustrating the 4-fold site vacancies, TiO <sub>2</sub> inclusions and Ti substitutions.....	75
5-9	Defects present in deposited films on TiO <sub>2</sub> termination.....	75
5-10	Defect percentages. ....	76
6-1	Initial 2ML deposited on TiO <sub>2</sub> -terminated STO structure.....	80
6-2	Adsorption sites.....	81
6-3	Final 2ML relaxed structure. ....	81
6-4	Oxygen adatom exchange mechanism on TiO <sub>2</sub> -terminated STO. ....	83
6-5	Oxygen adatom hop mechanism on SrO-terminated STO. ....	84

6-6	SrO diffusion mechanism on TiO <sub>2</sub> -terminated STO.....	85
6-7	SrO ad-dimer surface diffusion on SrO termination.....	86
6-8	Structure formed when Ti, TiO or TiO <sub>2</sub> is adsorbed, surface O bonds with Ti to make Ti 4 coordinated. ....	87

Abstract of Dissertation Presented to the Graduate School  
of the University of Florida in Partial Fulfillment of the  
Requirements for the Degree of Doctor of Philosophy

COMPUTATIONAL STUDY OF THE DEPOSITION OF METAL-OXIDE THIN FILMS ON  
STRONTIUM TITANATE: MORPHOLOGY AND GROWTH MODES

By

Jennifer Lynne Wohlwend

August 2009

Chair: Susan B. Sinnott

Major: Materials Science and Engineering

Thin films of strontium titanate, as well as one of its component oxides,  $\text{TiO}_2$ , have been of great interest due to their applicability in electronic devices. Here, classical molecular dynamics simulations are used to examine the growth of  $\text{SrTiO}_3$  (STO), SrO and  $\text{TiO}_2$  thin films on STO. In particular, the simulations consider the deposition of SrO and  $\text{TiO}_2$  molecules and stoichiometric STO clusters at incident energies of 0.1, 0.5, and 1.0 eV/atom onto the (001) surface of STO. The role of surface termination layer (SrO vs.  $\text{TiO}_2$ ), incident energy and in the case of STO deposition incident particle size and deposition scheme is investigated. In the case of SrO deposition, smooth, ordered films are produced for all incident energies considered and for both surface terminations. In contrast, in the case of  $\text{TiO}_2$  deposition, three-dimensional islands are formed under all conditions. Growth modes predicted are, as shown, a consequence of the mobility and interaction energy of each particle (SrO or  $\text{TiO}_2$ ) with the substrate.

For STO thin film deposition three schemes are investigated, alternating particle deposition (APD), alternating monolayer deposition (AMD) and cluster deposition. For APD, a beam of alternating SrO and  $\text{TiO}_2$  molecules is deposited on the (001) surface of STO with incident kinetic energies of 0.1, 0.5 or 1.0 eV/atom. AMD consists of the deposition of alternating SrO and  $\text{TiO}_2$  monolayers, where both have incident energies of 1.0 eV/atom.  $\text{SrTiO}_3$  cluster

deposition considers the deposition of 1, 2, 3, and 4-unit STO stoichiometric clusters having incident energies of 1.0 eV/atom. On the whole, some layer-by-layer growth is predicted to occur on both SrO- and TiO<sub>2</sub>-terminated STO for each type of deposition scheme. The prevalent defects observed in the first deposited layer on TiO<sub>2</sub>-terminated STO are Sr vacancies, TiO<sub>2</sub> inclusions and Ti substitutions, these are characterized and their effect on additional deposited layers is investigated.

Temperature accelerated dynamics (TAD) is used to predict energy barriers associated with diffusion mechanisms of adatoms and ad-dimers on (100) SrTiO<sub>3</sub> as well as energy barriers associated with the relaxation of a 2ML (1 SrO ML and 1 TiO<sub>2</sub> ML) film deposited using traditional MD simulations. We observe two differing surface ad-atom/ad-dimer diffusion mechanisms depending on substrate termination. On TiO<sub>2</sub> termination, an oxygen exchange mechanism is favored whereas on SrO termination, hopping mechanisms dominate.

In summary, the major contributions of this work to the literature are the simulated thin film growth of TiO<sub>2</sub>, SrO and STO using particulate and cluster deposition along with the investigation of ad-particle surface diffusion to elucidate the mechanisms involved during the first stages of deposition. This work has been published in Surface Science and the Journal of Materials Research Society along with two additional publications in preparation.

## CHAPTER 1 INTRODUCTION

### General Introduction

Strontium titanate is the archetype perovskite that has inspired countless experimental and theoretical studies. SrTiO<sub>3</sub> (STO) possesses several properties that make it useful in electronic device applications. For example, STO's high dielectric constant and low dielectric loss make it an attractive material in ferroelectric thin film capacitors,<sup>1,2</sup> microwave applications<sup>3</sup>, tunable resonant circuits<sup>4</sup> and dynamic random access memory applications.<sup>5</sup> Due to its lattice compatibility, STO is a desirable substrate material for high T<sub>c</sub> superconductors; moreover, the growth of atomically smooth films on these substrates is critically important for the epitaxy and performance of heterostructures.<sup>6-9</sup> This has motivated extensive examination of thin film growth on STO. Of particular interest here, the way in which STO and its components are deposited, can be used to control its surface structure and the properties of the resulting thin films.<sup>10</sup>

### Strontium Titanate and Component Oxides Structure and Applications

STO is isostructural with the mineral perovskite (CaTiO<sub>3</sub>), hence the nomenclature<sup>11</sup> and has a lattice constant of 0.3903 nm. This structure, having space group  $Pm\bar{3}m$  is based on a cubic close-packed lattice of SrO<sub>3</sub> (AO<sub>3</sub>) atoms with a Ti atom in the middle of the cubic configuration<sup>12</sup>, as shown in Figure 1-1. The large Sr<sup>2+</sup> cations are 12-fold coordinated and sit on the corner sites while the smaller Ti<sup>4+</sup> ion occupy all of the octahedral interstices surrounded by O<sup>2-</sup> ions<sup>11</sup>. At room temperature, STO exists in the cubic phase with a transition to the tetragonal antiferrodistortive phase at temperatures below its Curie point of 105 K<sup>13</sup> (110 K<sup>14</sup>). This phase transition involves symmetry changes in the crystal structure as a consequence of lattice energy minimization<sup>11</sup>. This structural optimization typically leads to small lattice distortions, in the case of STO in the form of a rotation of the oxygen octahedral about a <001> axis in opposite

directions in alternate unit cells. Experimentally, this is shown by changes in lattice spacing and conductivity as a function of temperature. This behavior is characteristic of antiferrodistortive materials<sup>13</sup>. Due to symmetry constraints arising from the cubic structure, STO displays paraelectric behavior at room temperature. This eliminates the problem of fatigue and aging experienced with other materials in the ferroelectric class that display spontaneous polarization at regular operating temperatures; such as BaTiO<sub>3</sub> with a Curie temperature of approximately 400K.

STO plays a major role in electronic applications due to its excellent electronic properties<sup>15, 16</sup>. The most impressive property is its large dielectric constant at 300. Such a high constant allows high storage capacity that is almost an order of magnitude higher than other gate dielectrics such as SiO<sub>2</sub> and Ta<sub>2</sub>O<sub>5</sub><sup>17</sup>. STO also has superior temperature, composition, and chemical stability compared to its fellow perovskites. These properties make STO an attractive material for use as Dynamic Random Access Memory (DRAM)<sup>18, 19</sup>, high-frequency integrated circuits<sup>20</sup>, and, due to its optical transparency, as insulating layers in thin film electroluminescent displays (TFELs)<sup>21</sup>.

STO thin films have also become the model material for use as substrates for the deposition high-T<sub>c</sub> superconductor thin films such as YBa<sub>2</sub>Cu<sub>3</sub>O<sub>7-δ</sub>, (YBCO) due to the chemical and structural compatibility between STO and YBCO thereby reducing interfacial strain related to the lattice parameter mismatch of the YBCO thin film with the substrate.<sup>22</sup> For use in high-T<sub>c</sub> superconductors, the interface quality is of utmost importance because of the ~2 nm coherence length where any precipitates or wrinkles can fatally impact the device.<sup>23</sup>

STO is comprised of alternating planes of SrO and TiO<sub>2</sub> (illustrated in Figure 1-1) approximately 2 Å apart. Thin films of SrO and TiO<sub>2</sub> have also been of interest. Atomic-layer

deposition of SrO on STO is shown to create atomically smooth STO surface for use in heterostructures<sup>8,24</sup> as well as buffer layers<sup>25,26</sup>. Buffer layers are utilized to suppress the strain created due to the lattice mismatch between substrate and film.<sup>27</sup> Bulk SrO, illustrated in Figure 1-2, has the rocksalt structure where each Sr atom is coordinated with 6 O atoms and each O atom is coordinated with 6 Sr atoms having an Sr-O bond length of 2.58 Å. Bulk SrO has a lattice constant of 5.16 Å and therefore has a lattice mismatch of ~24% with STO.<sup>28</sup>

TiO<sub>2</sub> thin films, however, have significant applications in their own right. For example, TiO<sub>2</sub> is important for catalytic applications.<sup>29</sup> The two most stable TiO<sub>2</sub> polymorphs are rutile and anatase, in both, each Ti atom is coordinated with 6 O atoms and each O atom is coordinated with 3 Ti atoms. Experimentally, anatase (its structure is shown in Figure 1-3 A) is the dominant phase produced when TiO<sub>2</sub> is deposited on STO (001) due to the smaller lattice mismatch of ~3% with the underlying substrate; in contrast, the more thermodynamically stable rutile phase (its structure is shown in Figure 1-3 B) has a mismatch of ~15%.<sup>30</sup> Anatase thin films are useful because of their efficiency in photocatalysis<sup>31</sup> while rutile films are used in optical applications such as solar cells<sup>32</sup> and anti-reflective coatings.<sup>33</sup>

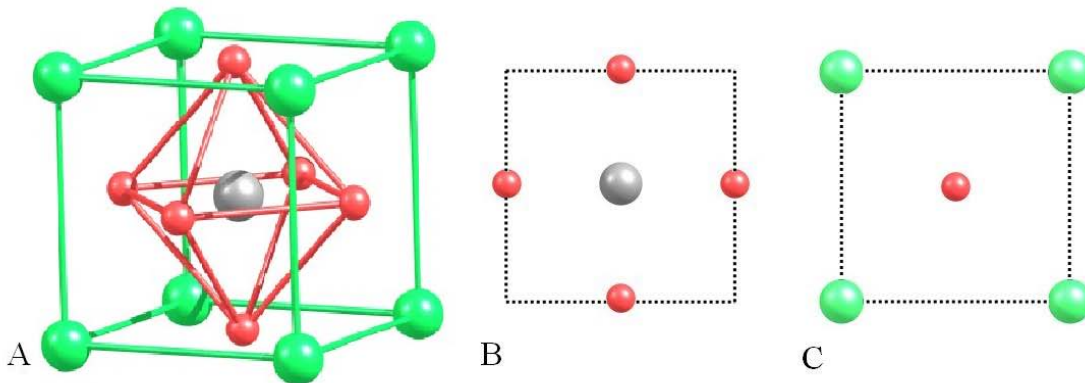


Figure 1-1 SrTiO<sub>3</sub> illustrating the alternating SrO/TiO<sub>2</sub> planes; Sr-lime, Ti-silver, O-red.

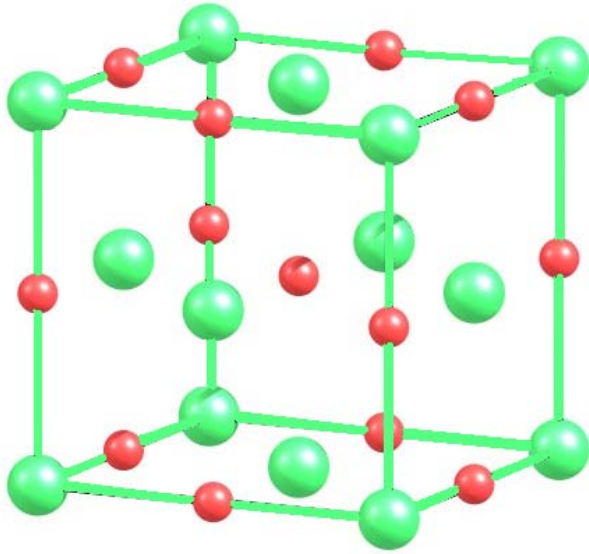


Figure 1-2 Bulk SrO exhibits a structure similar to the SrO plane in STO with a smaller Sr-O bond; Sr-lime, O-red.

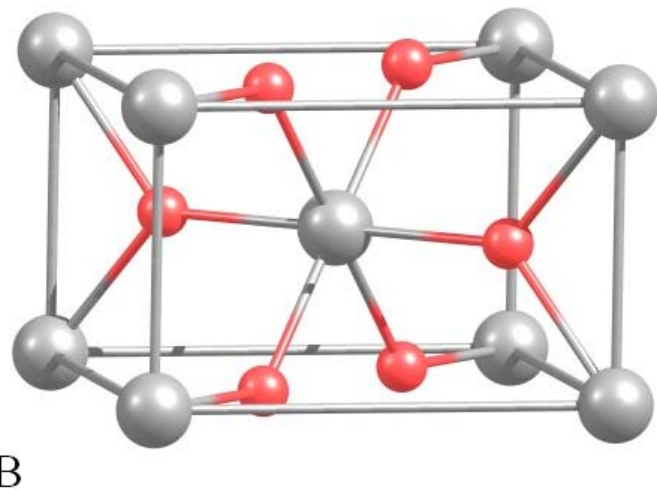
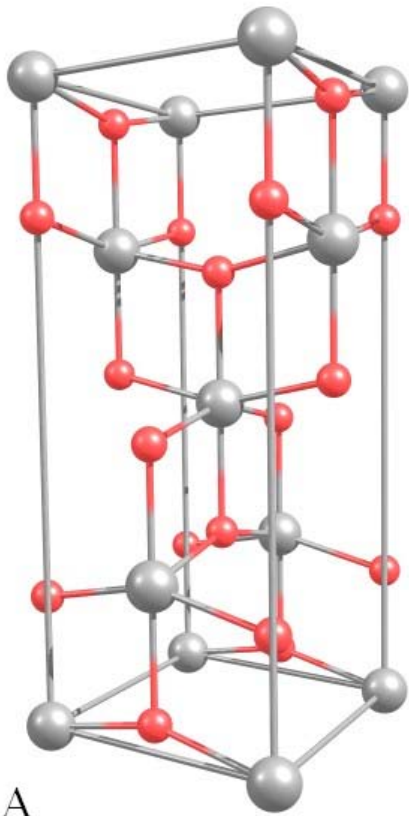


Figure 1-3 TiO<sub>2</sub> polymorphs A) Anatase, B) Rutile. Ti-silver, O-red.

## **Experimental Strontium Titanate and Component Oxides Deposition and Growth**

In the semiconductor industry thin film deposition is central in device fabrication.<sup>34</sup> Two key classes of thin film deposition are chemical vapor deposition (CVD) and physical vapor deposition (PVD). In CVD, reactive precursors are introduced to the substrate surface where they undergo a chemical reaction forming the thin film. CVD can be characterized based on the type of chemical reactions by which the thin film is created and by the operating conditions. A few CVD methods include: aerosol assisted CVD (precursors are atomized and transported to the substrate in a liquid or gas aerosol)<sup>35</sup>, metal organic chemical vapor deposition (MOCVD), (utilizing organometallic precursors)<sup>36</sup>, and ultra-high vacuum chemical vapor deposition (UHV-CVD); the benefits of UHV include the ability to clean and characterize substrates prior to deposition as well as perform in situ characterization along with the reduction of impurities.<sup>37</sup> The main benefits of most CVD methods are large area coverage, ability to coat complex geometries, high deposition rates and epitaxial growth; the main limitations are high start-up costs and toxicity or volatile nature of precursors and/or by-products.<sup>38</sup>

Physical vapor deposition utilizes thermally activated particles which bombard the surface and condense. These methods are categorized based on the method of vaporization of the target. One class of PVD, sputter deposition, removes the target material by bombarding the target surface and ballistically removing material. It has the advantage of low substrate temperature regardless of the melting temperature of the target material and some disadvantages are the lack of atomic-layer control and the incorporation of impurities in the film from the “sputtering” gasses. STO and component oxides have been successfully grown using excimer laser sputtering,<sup>39</sup> magnetron sputtering<sup>40-42</sup> and ion beam sputtering.<sup>43</sup>

As opposed to sputter techniques, the second class includes methods where the target material is evaporated instead of ballistically removed. Two main types of evaporation PVD

methods used to deposit STO and its component oxides are pulsed laser deposition (PLD) and molecular beam epitaxy (MBE). PLD is a widely researched method for homogeneous thin film fabrication and is an attractive technique to produce in situ stoichiometric ferroelectric thin films.<sup>5, 44</sup> Deposition is accomplished by focusing short, high-energy laser pulses onto a stoichiometric target in a vacuum chamber. The energy from the laser is transferred to the particles and evaporation occurs creating a plume that contains species ranging from atoms and molecules to clusters having a range in size from 0.1 to 50  $\mu\text{m}$ .<sup>45, 46</sup> Several advantages of using PLD when growth parameters have been optimized, include reproducibility<sup>47</sup>, single-phase purity and accurate stoichiometry<sup>48</sup>.

MBE is also viable technique to deposit thin films. This method has the ability to deposit monolayers by utilizing elemental sources, allowing for high compositional accuracy of the deposited thin film; these factors make it an attractive method for the design of complex systems.<sup>49</sup> The disadvantages of both PLD and MBE are the difficulty in large-scale deposition.

Experimentally, SrO thin films have been successfully deposited on hydrogen-terminated Si (100) for use as a buffer layer between Si and STO.<sup>25</sup> Also, one atomic layer of SrO has been deposited on TiO<sub>2</sub>-terminated STO by MBE in order to change the surface termination<sup>50</sup> and thereby eliminate precipitates during the deposition of YBCO.<sup>6</sup> In addition, growth dynamics studies of epitaxial SrO films grown on STO (001) substrates carried out by Takahashi et al. indicated that after deposition of the first SrO layer, subsequent layer-by-layer growth of SrO occurred with the atoms occupying positions consistent with bulk SrO.<sup>51</sup>

In situ reflection high-energy electron diffraction (RHEED) measurements during laser-MBE of TiO<sub>2</sub> films on STO (001) substrates performed by Ong and coworkers indicated various growth modes of TiO<sub>2</sub> films.<sup>52</sup> Well ordered and atomically flat anatase thin films have been

successfully grown in a layer-by-layer fashion on Nb-doped STO using oxygen plasma assisted molecular beam epitaxy at a growth rate of approximately  $0.03 \text{ \AA/s}$ .<sup>53</sup> A study on the sputter deposition of  $\text{TiO}_2$  thin films discussed the presence of  $\text{TiO}_2$  clusters in the gaseous phase given that the separation distance between the target material and the substrate was larger than the mean free path of the sputtered species (which is the average distance a particle travels before colliding with another particle). This gives the atomic species and small molecules in the gas phase time to combine and form clusters.<sup>54</sup> The size of the clusters and subsequently deposited film were shown to be dependent on the target to substrate distance. In particular, a larger distance (250 mm) promoted the growth of larger clusters (3 nm in diameter) and yielded an amorphous type  $\text{TiO}_2$  thin film whereas the shorter distance (50 mm) allowed only smaller clusters (less than 2 nm diameter) to form producing a crystalline film. This illustrates the impact of the type and size of the incident species on the morphology of the resulting films.

In addition to examining the deposition of the components of STO, numerous experimental studies have been conducted to better understand STO thin film growth under varying conditions. For example, Khodan and coworkers<sup>55</sup> investigated the PLD of epitaxial STO films. They observed the formation of smooth multilayer films at temperatures above 873 K. Additionally, they concluded that, although annealing in an oxygen environment at 1373 K improves the functional properties of the STO films significantly, only films deposited at pressures below  $10^3 \text{ Pa}$  exhibited low dielectric losses and high agility.

Similar results were obtained by Ohtomo and Hwang<sup>56</sup> who examined the dynamics of STO homoepitaxial films grown by PLD. They found that by controlling the oxygen partial pressure and growth temperature, two-dimensional layer-by-layer growth could be achieved.

## Computational Studies of Deposition and Growth

Molecular dynamics (MD) simulations are a powerful way to predict the deposition characteristics of STO and its component oxides. MD allows one to view the atomic level mechanisms involved in the initial stages of deposition and will be discussed in detail in Chapter 2. For example, MD simulations of epitaxial SrO film growth on STO indicated that only one layer of SrO can be deposited on TiO<sub>2</sub>-terminated STO before a change in structure occurs.<sup>57</sup> Such a change in structure corresponds to the continuation of the SrO-TiO<sub>2</sub> stacking sequence found in STO. The effect of temperature and termination on SrO migration was also investigated, it was found that the higher the temperature, the more mobile the deposited particles on the SrO-terminated surface, and that SrO is not mobile on the TiO<sub>2</sub>-terminated substrate.

TiO<sub>2</sub> thin film deposition on Fe<sub>2</sub>O<sub>3</sub>, Al<sub>2</sub>O<sub>3</sub>, and SiO<sub>2</sub> has been simulated using MD and predicted 3D island formation with a mixture of amorphous and polycrystalline structures within the 3 nm deposited film.<sup>58</sup> MD simulations have also been carried out to elucidate the mechanisms involved during deposition of Ti<sup>4+</sup>, TiO<sup>2+</sup>, TiO<sub>2</sub>, and Sr<sub>4</sub>Ti<sub>4</sub>O<sub>12</sub> on STO.<sup>59</sup> When simulating the deposition of Ti<sup>4+</sup>, TiO<sup>2+</sup>, TiO<sub>2</sub>, the study includes a corresponding vacancy on the substrate. This vacancy is then shown to be filled in by the incident species but the deposition of several TiO<sub>2</sub> units was not investigated. In the same study, when looking into the homoepitaxial growth of STO, a 2-unit STO “cluster” is used. This cluster, however, has the unit cell geometry of bulk STO, thereby building the STO structure into the deposited film.

Cluster deposition has been extensively simulated for metals<sup>60-63</sup>, investigating the impact of size, from 1 to hundreds of thousands of atoms, and incident kinetic energy, from meV/cluster to MeV/cluster.<sup>64</sup> Järvi et al. utilized MD to study the effect of temperature on the maximum cluster size able to exhibit complete alignment between the cluster and the substrate (epitaxy).<sup>63</sup> Small metallic clusters ( $\leq 100$  atoms/cluster) are found to become epitaxial from the energy

released by initial impact due to melting and resolidification. Larger clusters (100-1000 atoms/cluster) require additional thermal energy to enable the diffusion of twin dislocations within the clusters which was found to be the mechanism responsible for attaining epitaxy.

While MD simulations are able to predict the initial stages of deposition, including non-equilibrium structures created, they have two significant limitations: the time and length-scales are many orders of magnitude smaller than those that are important in most experiments. To overcome this limitation other computational methods are used to determine the equilibrium structure of the deposited film, including Monte Carlo<sup>65</sup> (MC), hybrid approaches<sup>66, 67</sup>, kinetic MC<sup>68</sup>, and accelerated dynamics.<sup>69</sup>

For example, STO thin film growth was investigated using the MC technique, a stochastic method where SrO, TiO<sub>2</sub> and STO units are randomly placed on an STO lattice and allowed to diffuse according to an Arrhenius relationship between hopping rate and temperature.<sup>70</sup> While these simulations include an experimentally obtained diffusion barrier, as opposed to MD simulations, these results do not incorporate the physics of atomic interactions. The growth of the film is determined using statistical probabilities and therefore is insufficient to describe the mechanisms involved at the atomic scale during the initial stages of deposition.

Hybrid approaches to study film growth are comprised of utilizing the benefits of MD during the initial deposition event and MC during the relaxation between deposition events.<sup>71</sup> In this approach, an atom is chosen randomly and displaced by a distance,  $\alpha(\zeta)$  (where  $\alpha$  is the maximum allowed displacement and  $\zeta$  is a random number between -1 and 1). Next, the change in energy ( $\Delta E$ ) due to the displacement is calculated. If the move is energetically favorable ( $\Delta E$  is -) it is accepted, if  $\Delta E$  is (+) the move is accepted with probability  $\exp(-\Delta E/kT)$ , where  $k$  is the Boltzmann constant and  $T$  is the temperature.<sup>72</sup> This approach allows the non-equilibrium

dynamics of the deposition event to be described adequately using MD while extending the time-scale simulated using the stochastic, MC method.

Kinetic Monte Carlo (kMC) is another simulation technique frequently utilized to model deposition and growth of thin films simulating deposition methods such as PLD<sup>73-75</sup> and MBE,<sup>76</sup> the general process includes creating a list possible transition events then choosing an event based on a probability proportional to its rate. The list is then modified according to the current configuration and the process continues.<sup>77</sup> kMC parameters are based on rate constants and sticking coefficients obtained from MD and experiment.<sup>78, 79</sup> Such simulated deposition involves having *a priori* knowledge of the possible kinetic events and rate constants which could occur,<sup>80</sup> this is one of the main drawbacks of kMC. Unless a mechanism is listed as a possible event it will not be predicted using kMC, this limitation was made evident after the discovery of the ‘replacement’ (commonly known as exchange) mechanism for Al surface diffusion on Al (100) instead of the hopping mechanism previously believed to dominate.<sup>81</sup> Therefore, kMC methods without prior knowledge of the exchange mechanism would not predict the correct dynamics of diffusion.<sup>68</sup> This has led to the development of accelerated MD simulations where there is no need for prior knowledge of possible events.

Accelerated dynamics methods, in principle, increase the rate of transitions while accurately describing the physics of the system. One such method, hyperdynamics, is based on incorporating a bias potential to the potential energy function in regions away from the potential dividing surfaces (or saddles) between two states, escalating the rate of transitions from one potential minima to another and thereby extending the simulated time scale.<sup>82</sup> This method requires no previous knowledge of transition states but the development and implementation of the bias is non-trivial and many other studies have made modifications to reduce the

complexity.<sup>83, 84</sup> Another accelerated method is parallel replica dynamics that is similar, in principle, to parallel computing where the atoms of a system are spatially distributed between processors. In this technique the system is replicated and MD is performed simultaneously on each system therefore increasing the time-scale studied proportional to the number of processors used.<sup>69, 85</sup> A third accelerated method is temperature accelerated dynamics (TAD) and is based on performing MD at high temperatures thereby increasing the rates of transitions while keeping the lower temperature dynamics of the system and will be discussed in detail in Chapter 2.

### **Growth: Effects of Mobility and Diffusion**

Surface mobility of incident species have an impact on the growth mode and quality of film formed. Lower mobility, sometimes associated with lower temperatures, leads to the occurrence of defects in deposited films, while higher temperatures yield defect free smooth films due to the opposite trends in mobility.<sup>86</sup> Reflection high-energy electron diffraction (RHEED) is commonly used, *in-situ*, to monitor the growth-modes of deposited thin films. The period of RHEED oscillations corresponds to the time needed to go from a smooth surface to a rough surface and back to the smooth surface which indicates the growth of one monolayer, this is depicted along with corresponding surface coverage in Figure 1-4.<sup>2</sup> These provide a wealth of information enabling one to observe growth mode transitions and calculate surface diffusion parameters.<sup>87</sup> kMC simulations have also been developed to simulate RHEED intensities to gain a better understanding of the surface morphology evolution.<sup>88, 89</sup>

Three main types of film growth are Frank-van der Merwe (FM), Stranski-Krastanov (SK), and Volmer-Weber (VW) along with two types of limited diffusion growth modes, polycrystalline and columnar, these are illustrated in Figure 1-5.<sup>90</sup> FM is associated with 2D layer-by-layer growth, SK is described as layer-by-layer with island growth and VW is characterized by 3D island growth. One RHEED oscillation corresponds to one unit cell thereby

indicating layer-by-layer growth. Three of the major processes occurring during the initial states of growth are adatom diffusion, nucleation, and interlayer mass transport of which adatom surface diffusion is considered the most important.<sup>91</sup>

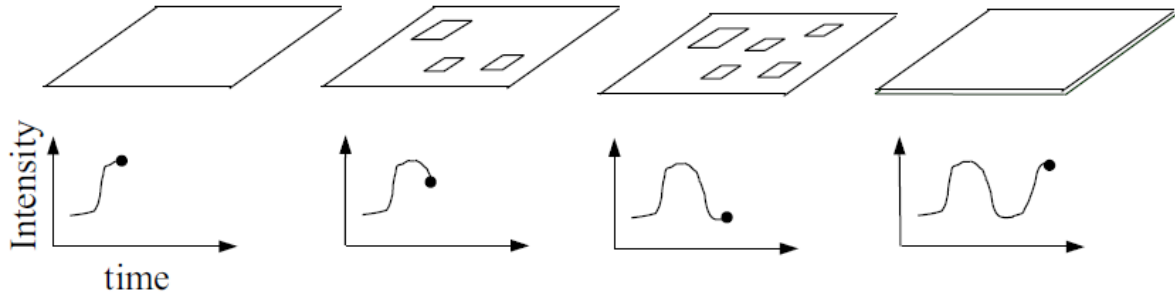


Figure 1-4 RHEED oscillations and the corresponding surface coverage.<sup>2</sup>

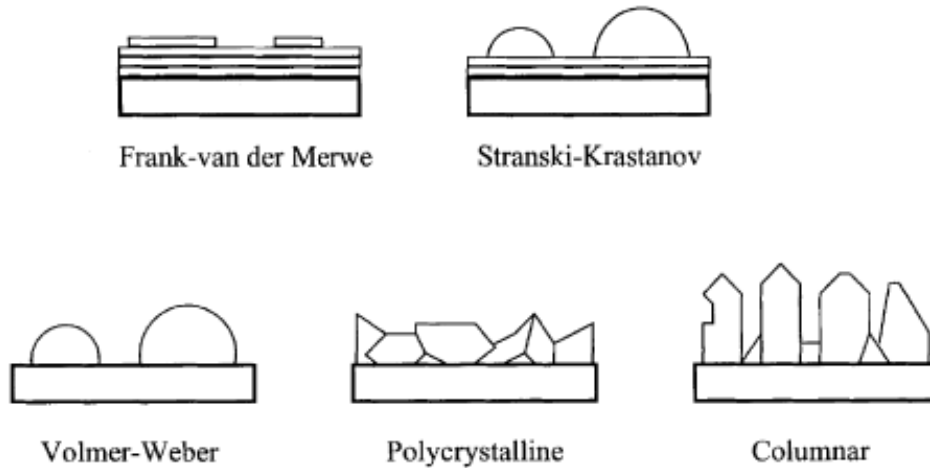
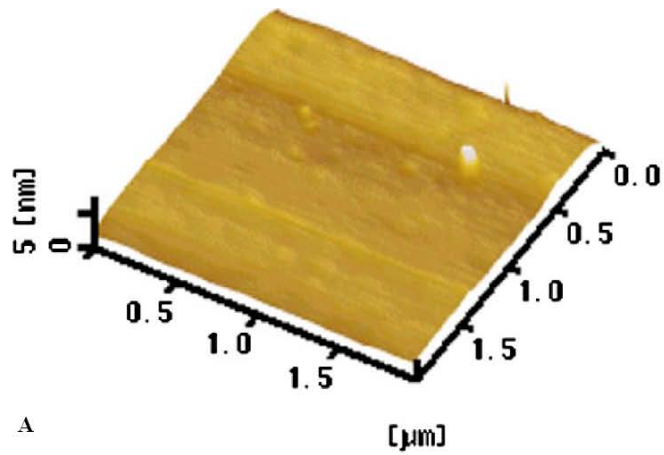


Figure 1-5 Schematic illustration of structures produced by FW, S, VW, polycrystalline and columnar growth.<sup>90</sup>

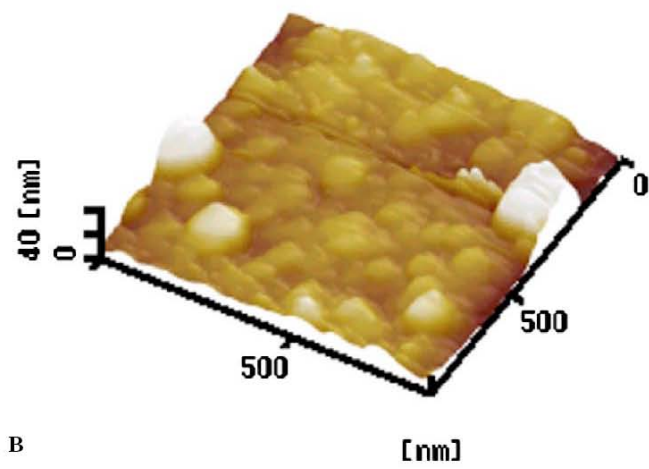
Multiple studies have investigated the different growth modes exhibited by STO deposition. Atomic force microscopy (AFM) images of STO thin films exhibiting each growth mode are shown in Figure 1-6.<sup>92</sup> One study of the impact of substrate temperature on growth mode during the deposition of STO using PLD<sup>93</sup> shows that island growth prevails for low

temperature deposition due to the decreased mobility of the incoming species this is indicated by a lack of clear RHEED oscillations. Temperatures between 560 and 770 °C produce layer-by-layer growth and step-flow growth occurs at temperatures above 800 °C. Step-flow growth is characterized by the recovery of the RHEED intensity after deposition has ceased. In this study, the time required for recovery is approximately 7 seconds illustrating the time-scale needed for complete relaxation of the deposited films. Step-flow growth has been shown to produce STO homoepitaxial films which are indistinguishable from the substrate and therefore yield higher quality films.<sup>94</sup> One study of STO homoepitaxial deposition found columnar structures which were attributed to diffusion-limited mobility.<sup>95</sup> This illustrates the importance of surface diffusion in thin film growth therefore understanding the mechanisms involved on the atomic level are essential.

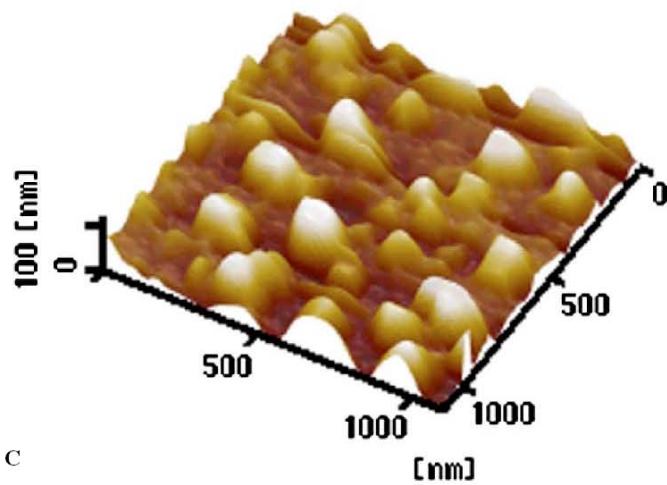
In this work, MD simulations are used to examine the deposition of STO, SrO and TiO<sub>2</sub> on the (100) surface of STO at incident energies of 0.1, 0.5 and 1.0 eV/atom. Of particular interest is the resulting morphology of thin films after deposition. Under consideration are the effects of surface termination (SrO vs. TiO<sub>2</sub>), incident energy of the deposited particles, and beam composition on the morphology and growth of STO, SrO and TiO<sub>2</sub> thin films. Included in this work is the deposition of SrO dimers, TiO<sub>2</sub> trimers as well as stoichiometric STO clusters. To better correlate STO thin film growth with experiment, we relax the clusters in vacuum where the resulting structure has little to no comparison to bulk STO. Temperature accelerated dynamics (TAD) is then used to extend the time-scale reached by the annealing of the deposited STO thin films. TAD is also utilized to understand the diffusion mechanisms involved with adatom and ad-dimer surface diffusion on (100) STO. The diffusion barriers obtained are able to explain the differing growth modes observed.



A



B



C

Figure 1-6 AFM images of SrTiO<sub>3</sub> thin films illustrating different growth modes observed. A) layer-by-layer growth mode, B) Stranski-Krastanov (S.K.) growth mode (layer-by-layer plus 3D island growth) and C) 3D island growth mode.<sup>92</sup>

## CHAPTER 2 COMPUTATIONAL METHODS

Molecular Dynamics (MD) has progressed by leaps and bounds since it was introduced in 1957 where Alder and Wainwright stated ‘The [MD] method consists of solving exactly (to the number of significant figures carried) the simultaneous classical equations of motion of several hundred particles by means of fast electronic computers.’<sup>96</sup> Their study reported that ‘large’ systems of 108, 256, and 500 particles took one hour for 2000, 1000, and 500 collisions, respectively, to occur using the first commercial computer, the UNIVersal Automatic Computer (UNIVAC).<sup>96</sup> This study is archaic by today’s standards where 5 billion particles have been simulated by Roth on a CRAY T3E-1200.<sup>97</sup>

### Molecular Dynamics

The main goal for classical MD simulations is to evolve a system of interacting atoms through time while describing the atoms in a classical manner.<sup>98</sup> It is a computer simulation technique which numerically solves Newton’s equations of motion and, for this study, can be outlined as illustrated in Figure 2-1<sup>99</sup>:

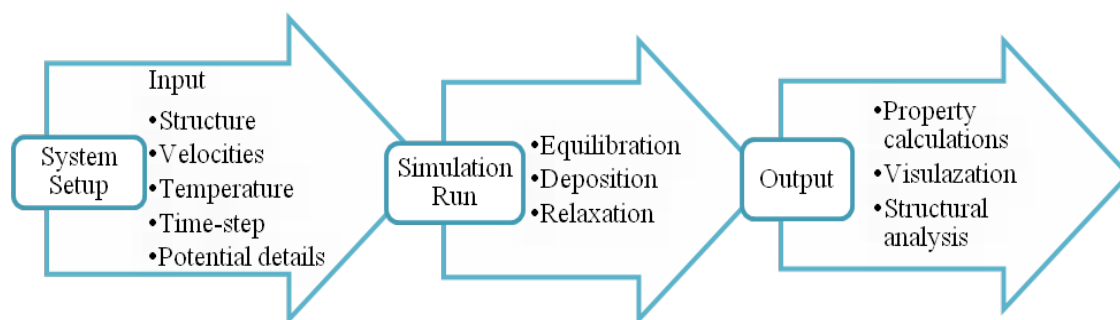


Figure 2-1 Schematic of simulation steps

This method allows a system’s time-dependent properties to be determined, thus enabling the study of complex, dynamic processes such as deposition. Here, Newton’s equations of

motion,  $F = ma$ , are integrated using the Gear 5<sup>th</sup> order predictor-corrector algorithm with a time step,  $\delta t$ , of 1 fs. The time step is a pivotal parameter in MD simulations. It must be small enough so as to encompass the phonon relaxation process of the system on an atomic scale, but large enough to be computationally efficient.

### Periodic Boundary Conditions

The system considered consists of two components, an STO substrate and a beam of incident particles. The free surface for deposition is simulated by adding vacuum along the depositing direction  $\langle 100 \rangle$ . To minimize substrate size effects and to simulate an infinite surface, periodic boundary conditions<sup>100</sup> (PBCs) are imposed along the  $\langle 010 \rangle$  and  $\langle 001 \rangle$  directions.

The system of interest is placed in a central cell which is replicated in all directions forming an infinite lattice. If a particle leaves its primitive cell, it is translated to the opposite face thereby keeping the number of atoms constant. A schematic of two-dimensional PBCs is shown in Figure 2-2 where the primitive cell is shaded. The central particle within the circle interacts with all other particles within the cutoff,  $R_c$ , chosen based on parameterization of the potential, all other interactions are neglected. The system size,  $L$ , must be at least twice  $R_c$  to ensure a particle does not interact with its replicated image.

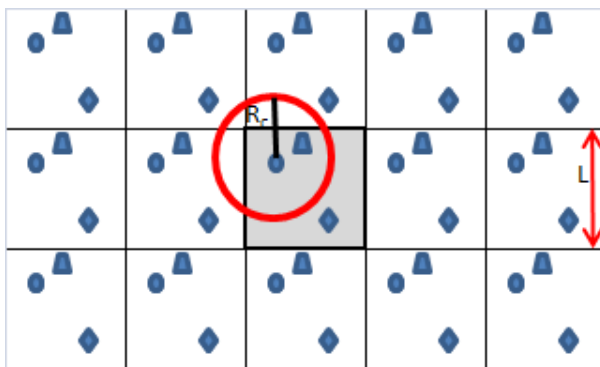


Figure 2-2 Schematic of periodic boundary conditions.<sup>101</sup>

## Velocity Rescaling Thermostat

Deposition involves the transfer of energy from the incident particles to the deposition site. This transferred kinetic energy can cause undesirable temperature increases in the system over time. For this reason a thermostat was utilized to simulate energy dissipation and to better model experimental conditions, where energy dissipation occurs through phonon vibrations over distances larger than those available in the simulation system. The thermostat involves rescaling the velocities of the atoms outside the region in which deposition takes place so as to maintain the desired temperature in this region. The arrangement of thermostat atoms relative to “active” atoms, i.e., atoms which are allowed to evolve in time with no constraints, is shown schematically in Figure 2-3. The lateral dimensions of the unit cell are fixed to those determined for STO described by this potential at the simulation temperature.

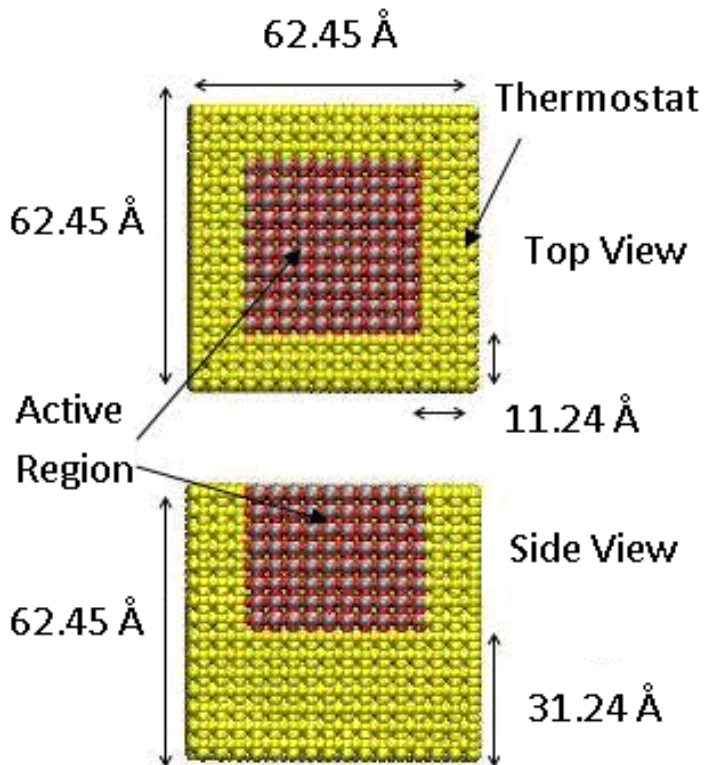


Figure 2-3 STO substrate illustrating thermostat and active regions.

In MD, temperature is defined in terms of the kinetic energy of the system, (Equation 2-1).

$$E_k = \frac{1}{2} \sum_{i=1}^N m_i v_i^2 = \frac{3}{2} N k_B T . \quad (2-1)$$

Here,  $m_i$  and  $v_i$  are the mass and velocity, respectively, of atom  $I$ ,  $N$  is the total number of atoms in the system,  $k_B$  is the Boltzmann constant. Temperature is determined by rearranging equation (2-1) as follows:

$$T = \frac{1}{3Nk_B} \sum_{i=1}^N m_i v_i^2 . \quad (2-2)$$

The desired temperature is maintained by multiplying the velocity of the thermostated atoms by  $\sqrt{T_{target} / T_{current}}$ .

### **Gear 5<sup>th</sup> Order Predictor-Corrector**

In this work, Newton's equations of motion are integrated utilizing the Gear 5<sup>th</sup> order predictor-corrector algorithm. This integrator propagates particle positions and velocities from time,  $t$ , to a time,  $t + \delta t$ , by utilizing a finite difference scheme.<sup>97</sup> The order of the predictor-corrector algorithm corresponds to the order of the Taylor expansion used to integrate the equations of motion. The higher the order, the less energy fluctuation there is in the system; this results in higher accuracy for the predictor. By this integration, positions and accelerations are predicted to allow the time evolution of the system to be observed.

The integration scheme begins with the prediction of positions,  $\mathbf{x}^p$ , velocities,  $\mathbf{v}^p$ , and accelerations,  $\mathbf{a}^p$ , at  $t = t + \delta t$  from the initial positions,  $\mathbf{x}(t)$  and velocities  $\mathbf{v}(t)$  (Equation 2-3)<sup>101</sup>:

$$\begin{aligned} \vec{x}^p(t + dt) = & \vec{x}(t) + \vec{v}(t)dt + \frac{1}{2} \vec{a}(t)dt^2 + \frac{1}{3!} \frac{d^3 \vec{x}}{dt^3}(t)dt^3 + \frac{1}{4!} \frac{d^4 \vec{x}}{dt^4}(t)dt^4 \\ & + \frac{1}{5!} \frac{d^5 \vec{x}}{dt^5}(t)dt^5 , \end{aligned} \quad (2-3)$$

$$\vec{v}^p = \vec{v}(t) + \vec{a}(t)dt + \frac{1}{2}\alpha(t)dt^2 + \frac{1}{3!}\beta(t)dt^3 ,$$

$$\vec{a}^p = \vec{a}(t) + \vec{\alpha}(t)dt + \frac{1}{2}\vec{\beta}(t) ,$$

$$\vec{\alpha}^p = \vec{\alpha}(t) + \vec{\beta}(t)dt ,$$

where,

$$\vec{v}(t) = \frac{d\vec{x}}{dt}(t) , \quad \vec{a}(t) = \frac{d^2\vec{x}}{dt^2}(t) ,$$

$$\vec{\alpha}(t) = \frac{d^3\vec{x}}{dt^3}(t) , \quad \vec{\beta}(t) = \frac{d^4\vec{x}}{dt^4}(t) , \quad \vec{\gamma}(t) = \frac{d^5\vec{x}}{dt^5}(t) .$$

The second step is the calculation of the force acting on each atom by calculating the potential function at the predicted positions giving the correct acceleration. After evaluating the forces of the particles at the predicted positions, accelerations are computed and compared to the ‘predicted acceleration’. The error (Equation 2-4) in the predicted values is proportional to the difference between the predicted and correct acceleration.

$$\Delta a(t + dt) = a^c(t + dt) - a^p(t + dt) . \quad (2-4)$$

The corrections imposed are proportional to this error. The final step is the correction of the predicted positions and velocities<sup>101</sup> (Equation 2-5):

$$x^c(t + dt) = x^p(t + dt) + \frac{3dt^2}{16} \Delta a(t + dt) ,$$

$$v^c(t + dt) = v^p(t + dt) + \frac{251dt}{360} \Delta a(t + dt) ,$$

$$\alpha^c(t + dt) = \alpha^p(t + dt) + \frac{11}{18dt} \Delta a(t + dt) , \quad (2-5)$$

$$\beta^c(t + dt) = \beta^p(t + dt) + \frac{1}{6dt^2} \Delta a(t + dt) ,$$

$$\gamma^c(t + dt) = \gamma^p(t + dt) + \frac{1}{60dt^3} \Delta a(t + dt) .$$

## Interatomic Potential

Particles within the system interact with each other through interatomic interactions and forces. Such forces are obtained by using an expression that describes the potential energy between and among atoms (the “potential”) and are the gradient of the potential with respect to atomic displacements.<sup>100</sup> In order to validate a model, it must be compared to experimental data and crystal properties. There are parameters within the potential that are fitted to experimental data; this is the necessary link between simulation and experimentation.

The interatomic potentials used here take the traditional form for ionic materials of long-ranged electrostatic interactions plus a short-ranged empirical interaction term. Short-range forces can be described as van der Waals and repulsive interactions resulting from electron-cloud overlap. Long range forces dominate when particles are beyond a predetermined cutoff. They can be further subdivided into electrostatic, induction and dispersion contributions. The first of which is due to the permanent charge distribution and the other two encompass fluctuation charge contributions.<sup>102</sup> In this work these forces are represented by a Coulombic term. In ionic systems, short-ranged interactions are commonly modeled using the Buckingham potential.<sup>103</sup> The potential energy is the sum of both the long- and short-range contributions. After the interactions in the STO system are parameterized, it is possible to generate a list of energies at different separation distances which can consequently be used during the simulation increasing the computational efficiency.

### Buckingham potential

The Buckingham (Equation 2-6) potential is comprised of two parts, a short-ranged repulsive term and an attractive term.<sup>104</sup>

$$V_{Buck} = A_{ij} \exp\left(-\frac{r_{ij}}{\rho_{ij}}\right) - \left(\frac{C_{ij}}{r_{ij}^6}\right). \quad (2-6)$$

Here,  $r_{ij}$  is the distance between any pair of atoms of species  $i$  and  $j$ . The first term corresponds to the repulsive interactions resulting from electron cloud overlap and the second term corresponds to attractive van der Waals interactions.<sup>103</sup> The potential parameters,  $A_{ij}$ ,  $\rho_{ij}$  and  $C_{ij}$ , are related to the ionic stiffness, radii, and strength of the van der Waals interactions between ions. Several parameter sets were tested; the potential parameters from Sekiguchi *et al.*<sup>105</sup> (see Table 2-1) were chosen as the most appropriate for the system of interest. Of particular importance for these simulations, within this partial charge model the SrO and TiO<sub>2</sub> formula units are individually charge neutral; thus the deposited particles and substrate are at all times charge neutral. Pertinent material properties calculated with this potential are compared to experimental values and previous computational calculations (see Tables 2-2 and 2-3).

The current potential produces bulk lattice parameters which are in good agreement with experimental results; the elastic properties, however, show a rather large deviation from experimental results in the case of rutile and anatase. These differences are a consequence of using a potential developed for STO as opposed to a potential parameterized specifically for TiO<sub>2</sub>. It is also noted that this potential predicts the bulk moduli of SrO fairly well.

### **Coulomb potential**

Long range forces can be further subdivided into electrostatic, induction and dispersion contributions. The first of which is due to the permanent charge distribution and the other two encompass fluctuation charge contributions.<sup>102</sup> In this study these forces are represented by a Coulombic term, (Equation 2-7).

$$V_{Coul} = \frac{1}{2} \sum_{i=1}^N \sum_{j \neq i=1}^{\infty} \left( \frac{q_i q_j}{r_{ij}} \right). \quad (2-7)$$

Here,  $q_i$  and  $q_j$  correspond the charges on atoms  $i$  and  $j$ , respectively,  $r_{ij}$  is the distance between them, and  $N$  is the total number of atoms.

It is well-known that the pairwise  $r^{-1}$  sum in the Coulomb potential is conditionally convergent,<sup>100</sup> meaning in order for the potential to converge to zero there must be an infinite value for  $r_{ij}$ . This is not possible for the simulated system sizes, thus the potential requires special treatment. Traditionally the Ewald summation<sup>106</sup> technique is used to carry out this sum; it is accurate but scales, at best, as  $O(N^{3/2})$ , where  $N$  is the number of atoms in the system. For this reason, the charged neutralized direct summation technique<sup>107</sup> is used (Equation 2-8).

$$V_{Coul} = \frac{1}{2} \sum_{i=1}^N \left( \sum_{\substack{j \neq i \\ (r_{ij} < R_c)}} \frac{q_i q_j}{r_{ij}} - \frac{q_i \Delta q_i(R_c)}{R_c} \right). \quad (2-8)$$

The first term is the  $1/r$  pairwise potential in Equation 2-7 and the second term is the Coulomb interaction of ion  $i$  with the surface charge, and  $\Delta q_i(R_c)$  is the net charge within the cutoff sphere ( $R_c$ ) of ion  $i$ ; here  $R_c$  is chosen to be 10.148 Å. This approach creates equal and opposite counter charges for each ion within this cutoff, thereby allowing the spherical truncation to be charged neutralized. The total potential energy is the sum of both the long- and short-range contributions; the forces used to predict the atomic trajectory are simply the first derivative of the potential energy. To improve convergence, an additional damping term is added in the manner described by Wolf *et al.*<sup>107</sup>

Table 2-1 Parameters used in the Buckingham and Coulombic potentials obtained from Sekiguchi *et al.*<sup>105</sup>

Interaction	A (eV)	$\rho$ (Å)	C (eV*Å <sup>6</sup> )
Sr <sup>1.331+</sup> -O <sup>1.331-</sup>	139621.961934	0.1963	2.33222
Ti <sup>2.662+</sup> -O <sup>1.331-</sup>	18476.946631	0.1963	0.0
O <sup>1.331-</sup> -O <sup>1.331-</sup>	21943.289277	0.2226	4.14616

Table 2-2 Comparison of calculated and experimental structure and elastic properties for SrTiO<sub>3</sub>.

	Calculated	Experimental	Error
Lattice Parameter STO (Å)	3.918	3.905	0.3%
C <sub>11</sub> (GPa)	405.18	335	21%
C <sub>12</sub> (GPa)	131.1	105	25%
C <sub>44</sub> (GPa)	131.1	127	3%

Table 2-3 Comparison of the results of current calculations, experimental data, and previous calculations for the structural properties of anatase and rutile TiO<sub>2</sub>, and rocksalt SrO. Where GULP is the General Utility Lattice Program

Anatase TiO <sub>2</sub>	Calculated (this work)	Calculated	Experiment <sup>b</sup>
Lattice Parameter (Å)	9.779	9.063 (GULP) <sup>a</sup>	9.514
	3.783	3.85 (GULP) <sup>a</sup>	3.786
Bulk(GPa)	231	176 (GULP) <sup>a</sup>	360±20
Cohesive energy (eV/TiO <sub>2</sub> )	56.13	21.54 (PBE) <sup>d</sup> 24.46 (LDA) <sup>d</sup>	
Rutile TiO <sub>2</sub>	Calculated (this work)	Calculated	Experiment <sup>b</sup>
Lattice Parameter (Å)	4.528	4.587(GULP) <sup>a</sup>	4.593
	3.038	2.958(GULP) <sup>a</sup>	2.958
Bulk(GPa)	298	229(GULP) <sup>a</sup>	211±7
Cohesive energy (eV/TiO <sub>2</sub> )	44.34	21.44 (PBE) <sup>d</sup> 24.44 (LDA) <sup>d</sup> 20.27 (BLYP) <sup>d</sup>	19.9 <sup>d</sup>
Rocksalt SrO	Calculated (this work)	Calculated	Experiment <sup>c,f</sup>
Lattice Parameter (Å)	5.257	5.19 (GGA) <sup>e</sup>	5.16
Bulk(GPa)	96	85.9 (GGA) <sup>e</sup>	91
Cohesive energy (eV/SrO)	12.54	11.80 (LDA) <sup>g</sup>	10.45 <sup>h</sup>

<sup>a</sup> Ref. <sup>108</sup>

<sup>b</sup> Ref. <sup>109</sup>

<sup>c</sup> Ref. <sup>110</sup>

<sup>d</sup> Ref. <sup>111</sup>

<sup>e</sup> Ref. <sup>112</sup>

<sup>f</sup> Ref. <sup>113</sup>

<sup>g</sup> Ref. <sup>114</sup>

<sup>h</sup> Ref. <sup>115</sup>

## Temperature Accelerated Dynamics

Thin film growth is mainly comprised of phenomena occurring in two time-scale regimes. The first encompasses the initial kinetic behavior of the depositing particles: collision and short-term relaxation, which occurs in the ps time range. The second involves the subsequent relaxation and diffusion of the deposited particles between deposition events, this happens on a time-scale of  $\mu\text{s}$ -s.<sup>71</sup> Conventional MD simulations are limited by a time-scale of ns therefore restricting the comprehensive modeling of thin film growth. Recently, there has been considerable attention to accelerated MD methods which have been able to extend the time-scale studied to orders-of-magnitude larger than traditional MD.<sup>116</sup>

The basic event examined is the transition from one state to another connected by a minimum energy pathway (MEP) as illustrated in Figure 2-4. This pathway contains a transition state at a maximum along the MEP, also known as a saddle configuration. Temperature accelerated dynamics (TAD) enlists two main assumptions: events of interest are considered infrequent or rare and harmonic transition state theory is applicable for the system of interest. This method takes advantage of accelerated transitions at higher temperatures in order to accelerate the “pace” of system evolution, yet still preserving the correct order of transitions at the temperature of interest. This is done by filtering the transitions to only allow those that would occur at the actual temperature of interest.<sup>117</sup>

Infrequent event systems are characterized by well defined transitions between states occurring on a time-scale of several vibrational periods. While the actual transition event occurs rapidly, the time between events can be orders of magnitude longer.<sup>118</sup> Since harmonic transition state theory is also assumed (no correlated events) an Arrhenius expression for the rate constant going from state A to B,  $k_{A-B}$  (Equation 2-9) is obtained.<sup>117</sup>

$$k_{A-B} = v_0 \exp\left(-\frac{1}{k_B T} E_a\right), \quad (2-9)$$

where  $E_a$  is the energy barrier between the saddle configuration and the minimum (State A) and  $v_0$  is a pre-exponential factor calculated using the Vineyard formula (Equation 2-10).<sup>119</sup>

$$v_0 = \prod_{i=1}^{3N} \nu_i / \prod_{j=1}^{3N-1} \nu_j. \quad (2-10)$$

Here,  $\{\nu_i\}$  is the set of vibrational frequencies at the minimum (State A) and  $\{\nu_j\}$  are the set of real-frequencies at the saddle point configuration.<sup>120</sup> This relationship is a consequence of assuming HTST, that the frequencies of both minimum and saddle configurations can be approximated by a harmonic oscillator. It is a measure of the width of the harmonic oscillators at the saddle versus the minimum.

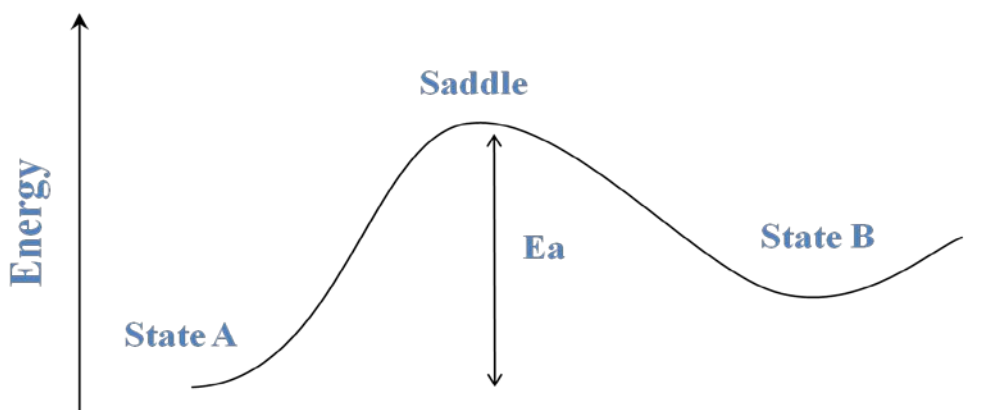


Figure 2-4 Schematic of transition state theory.

TAD utilizes basin-constrained MD, confining the trajectory to a particular potential energy basin. If the particle attempts to leave the basin it is reflected back to the original state and the time of the attempted escape is documented creating a list of ‘waiting times’ of attempted escapes.<sup>117</sup> At each state the system is evolved at  $T_{\text{high}}$  until a transition (or ‘escape’) is detected noting the waiting times and the saddle point, corresponding to the energy maximum of the MEP from state A to B, is found.<sup>69</sup> The nudged elastic band method was used to find the MEPs

between known initial and final states by first optimizing the initial and final state and then systematically creating and optimizing structures along the reaction pathway.

Using the energy barrier between the initial state and saddle configuration, the waiting times at  $T_{high}$  ( $t_{high}$ ), are then extrapolated to corresponding waiting times at  $T_{low}$  (the temperature of interest), ( $t_{low}$ ) given by (Equation 2-11).

$$t_{low} = t_{high} \exp \left( E_a \left( \frac{1}{k_B T_{low}} - \frac{1}{k_B T_{high}} \right) \right). \quad (2-11)$$

This procedure is illustrated in Figure 2-5. The simulation continues following the dashed line to the first detected transition at  $t_{high}$ , denoted by the red star. This time is then extrapolated along the line with a slope of  $-E_a$  (for said event) into a corresponding  $t_{low}$ , denoted by the black star. An additional assumption that there exists a minimum pre-exponential factor,  $v_{min}$ , enables one to impose a stopping time,  $t_{high,stop}$ , where the probability that a shorter  $t_{low}$  would replace the shortest-time transition recorded, represented by the blue circle, is less than  $\delta$ .<sup>69</sup> Both  $v_{min}$  and  $\delta$  are input parameters on the order of  $10^{-12}$  and 0.01 respectively. This continues until  $t_{high,stop}$ , (Equation 2-12), is reached (indicated by the open circle) and the event with the shortest time at the low temperature is accepted, blue circle, and the process repeats with the new position.

$$t_{high,stop} \equiv \frac{\ln\left(\frac{1}{\delta}\right)}{v_{min}} \left( \frac{v_{min} t_{low,short}}{\ln\left(\frac{1}{\delta}\right)} \right)^{T_{low}/T_{high}}. \quad (2-12)$$

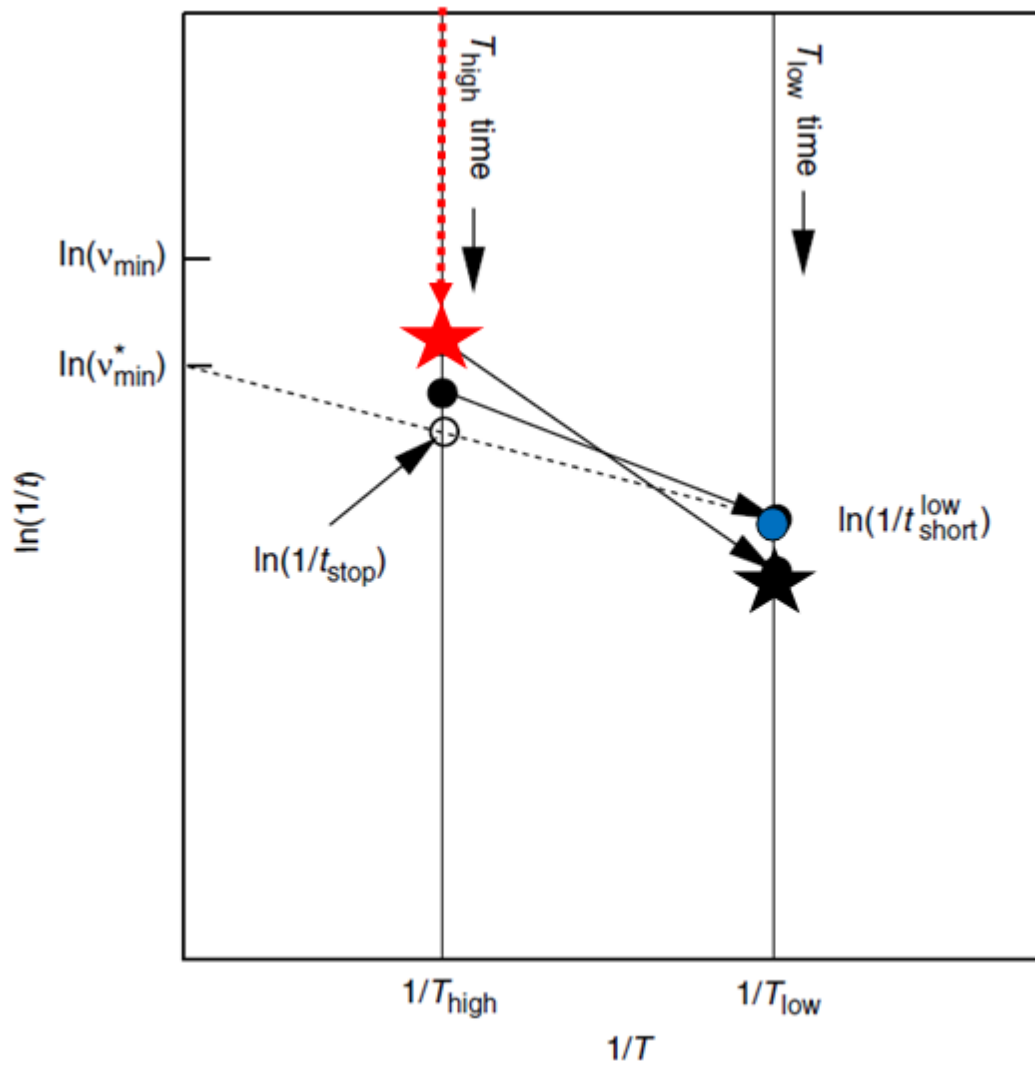


Figure 2-5 Schematic illustration of the extrapolation of  $T_{\text{high}}$  time to  $T_{\text{low}}$  time.<sup>121</sup>

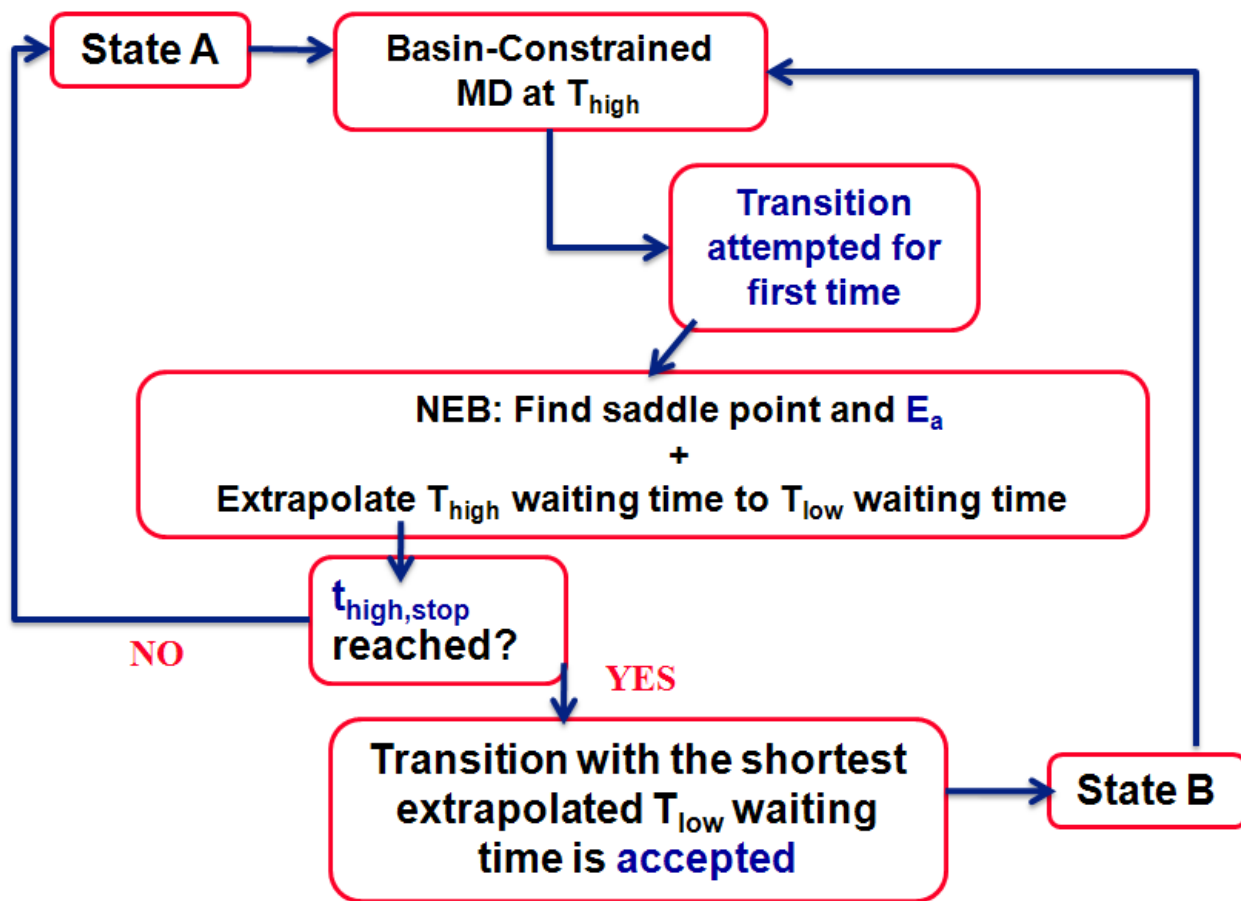


Figure 2-6 Flowchart illustrating the TAD procedure.

## CHAPTER 3 STRONTIUM OXIDE AND TITANIUM DIOXIDE THIN FILM DEPOSITION ON STRONTIUM TITANATE

To understand the deposition of STO, it is first beneficial to evaluate the growth of the component oxides, SrO and TiO<sub>2</sub>. By understanding the processes which dominate during the growth of these thin films, one can better understand the reasoning behind the morphology and growth of STO thin films. This work has been published in Surface Science.<sup>122</sup>

### **Simulation Set-up**

The system considered consists of two components, an STO substrate and a beam of incident particles. To model the substrate, a 16 x 16 x 16 cubic STO lattice is primarily used; this contains a total of 20,480 atoms. The free surface for deposition is simulated by adding vacuum along the depositing direction <100>. Before deposition begins, the substrate is equilibrated until minimum energy fluctuations are observed (corresponding to 100 ps) at the desired temperature of 973 K, which has been shown experimentally to produce crystalline films.<sup>123</sup> TiO<sub>2</sub> deposition was also carried out on an expanded substrate with dimensions of 30 x 30 x 16 to evaluate the impact of surface size.

To model deposition, each incident particle is assigned a velocity directly towards the surface along the [100] direction that corresponds to a kinetic energy of 0.1, 0.5, or 1.0 eV/atom. The particles in the beam are initially given random orientations and random positions over the substrate. Along the deposition direction they are approximately 30 Å apart, which corresponds to roughly 3 ps between each deposition event. This interval between deposition events allows the structure of the deposited film to, at least partially, equilibrate before the next particle is deposited, and gives the thermostat time to dissipate the excess energy. Each particle is deposited individually in a manner similar to that in MBE which, as mentioned in Chapter 1, is a widely used method to deposit STO. After depositing 60 incident particles (of either SrO or TiO<sub>2</sub>) the

system is annealed at an elevated temperature of 1100 K for approximately 50 ps to allow the films to equilibrate. Although the energies of individual deposited particles are consistent with experimental values, the short time scales available to MD simulation require that the interval between deposition events is much shorter than in experiment. As a result the total particle flux,  $1 \times 10^{11}$  particles/sec, is much higher than in experiment. Thus, while the deposited structures analyzed are in equilibrium on the timescales of tens of picoseconds, any experimental structural equilibrations associated with longer timescales are absent in the simulations.

## Results

### Strontium Oxide Deposition

A typical deposited SrO film is shown in Figure 3-1. Figures 3-1 A, B and C of the three partially grown layers show the extremely high level of order within each layer. The quality of the grown surface and the absence of any ions in any layer above the third indicate that there must be a significant amount of surface transport taking place. This is also a strong indication that the system has been able to reach equilibrium despite the high flux and short equilibration time.

To quantitatively analyze the structure of the SrO deposited films, a planar pair distribution function (PPDF) is determined for each deposited layer after a high temperature annealing (2000 K) and subsequent quench to remove thermal fluctuations. The PPDF is then compared with the corresponding PPDF for SrO layers in the bulk STO and in the bulk SrO. The analysis shown in Figures 3-2 and 3-3 shows distribution of distances of the oxygen neighbors of the strontium within each SrO layer. The first peak (between 2.5 and 3.5 Å) is the nearest neighbors, the second peak (between 5.5 and 6.0 Å) is the second neighbor peak. Previous computational work has shown that only one epitaxial SrO layer can be deposited on TiO<sub>2</sub>-terminated STO before the structural order of the SrO film breaks down.<sup>57</sup>

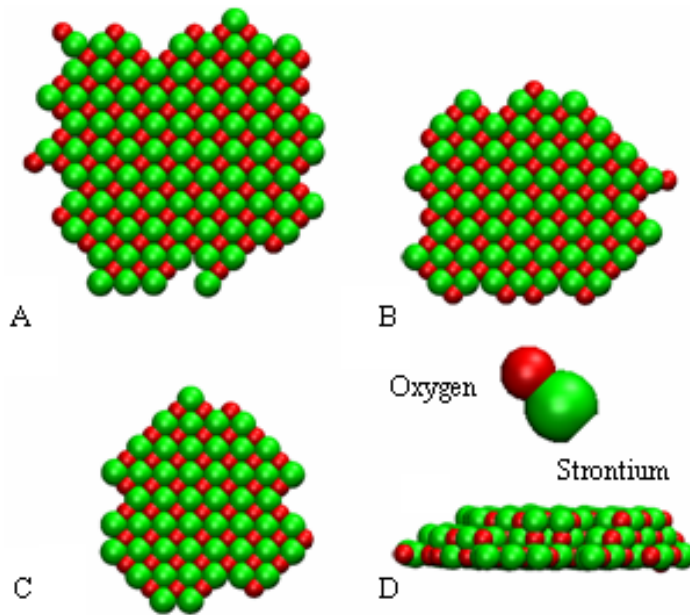


Figure 3-1 SrO layers that are deposited with an incident energy of 1.0 eV/atom on  $\text{TiO}_2$ -terminated STO A) first deposited layer B) second deposited layer C) third deposited layer D) side view.

As seen in Figure 3-2, we find that the first deposited layer (denoted by the number 1) on a  $\text{TiO}_2$ -terminated STO substrate displays Sr-O distances that are almost the same as in STO; however, even for this layer the first nearest neighbor peak contains a smaller peak at the distance corresponding to the Sr-O distance in rocksalt. The second deposited layer nearest neighbor peaks (denoted 2) is shifted towards the rocksalt peaks and the third deposited layer (denoted 3) shifts even more. This shift is illustrated by the arrow, and is consistent with Kubo's earlier simulation results.<sup>57</sup>

Figure 3-3 illustrates the effect of surface termination on the structure of the first deposited layer. In contrast to SrO on the  $\text{TiO}_2$  surface (Peak A, which is the same as Peak 1 in Figure 3-2), the first SrO layer grown on the SrO-terminated surface (Peak B) exhibits a structure in between that of the SrO layer in STO and the SrO layer in bulk rocksalt SrO.

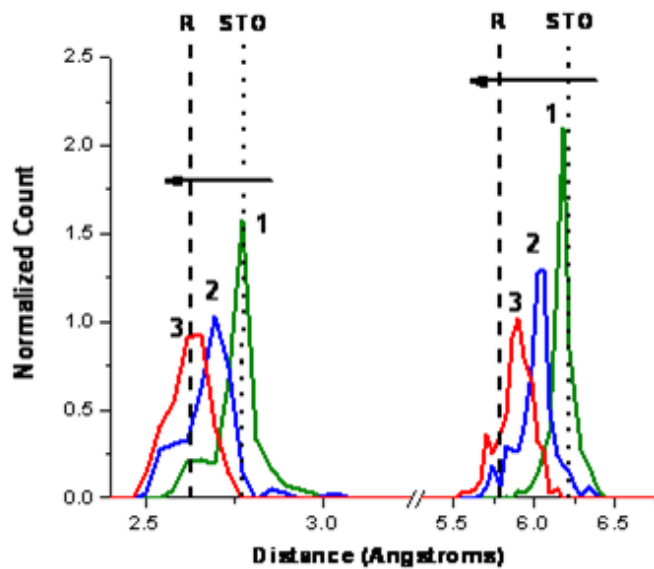


Figure 3-2 Sr-O PPDF for SrO layers on STO. As the deposited layers increase, the nearest neighbor distances approach that of bulk SrO.

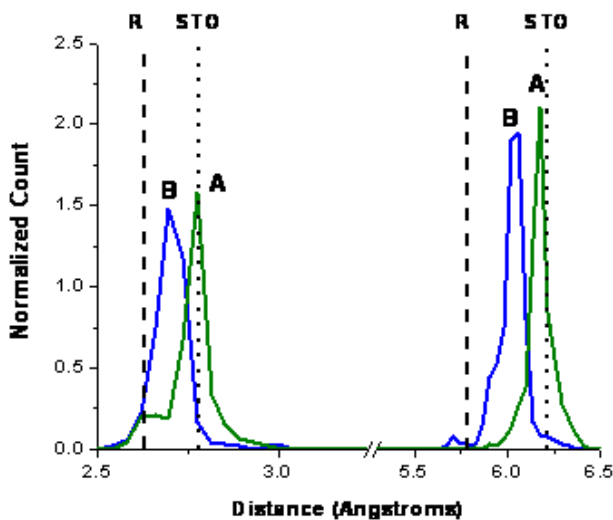


Figure 3-3 Sr-O PPDF showing an obvious correlation between the STO termination layer and SrO deposited film structure.

Crystallographically, the second SrO layer grown on  $\text{TiO}_2$ -terminated STO (shown in red) should be identical to the first SrO layer grown on the SrO-terminated STO (shown in black) as Figure 3-4 shows. The reduction in peak height is due to the smaller number of Sr atoms present

in the second SrO layer grown on TiO<sub>2</sub>-terminated compared to the first layer deposited on the SrO termination. This again indicates that the kinetics of the system are rapid and that the structures generated are in good thermal equilibrium.

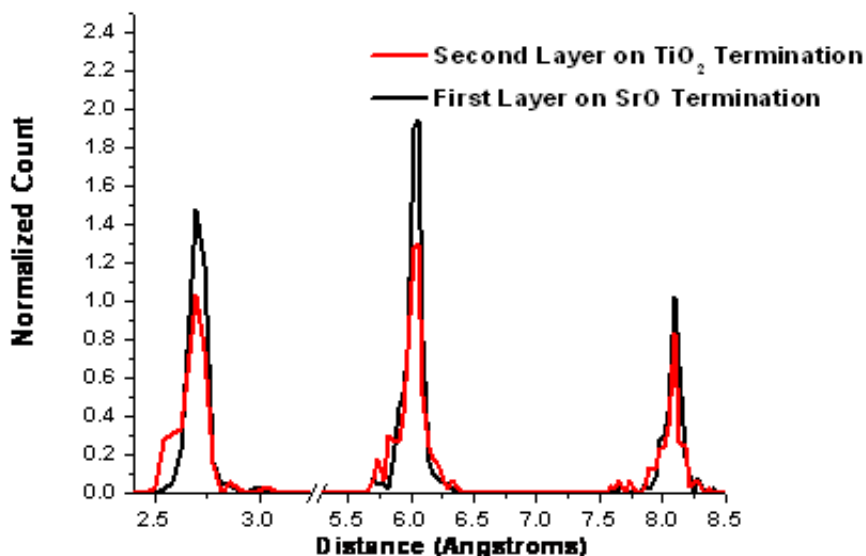


Figure 3-4 Sr-O PPDF showing the second SrO layer grown on TiO<sub>2</sub>-terminated STO corresponding to the first SrO layer grown on the SrO-terminated STO.

### Titanium Dioxide Deposition

The corresponding simulations have been performed for the deposition of TiO<sub>2</sub>. As can be seen from Figure 3-5 the growth morphology for the TiO<sub>2</sub> films is very different from the SrO films. In particular, there is no obvious ordering in the deposited layer and no obvious layering. Quantitative structural analysis was also performed for the case of TiO<sub>2</sub> deposition. The Ti-O first nearest neighbor distances for rutile, anatase, and STO are very similar (see Table 3-1), and thus do not provide a sensitive probe of the structure. Indeed, as Figure 3-6 shows, the Ti-O nearest neighbor distances are sharply peaked around the expected values. In contrast, the second and third nearest Ti-O neighbor distances are very different in the three structures (see Table 3-1), and thus should constitute a more sensitive probe of the crystallographic structure.

The most obvious feature of the PDFs in Figure 3-6 is the strong broadening of the 2<sup>nd</sup> and 3<sup>rd</sup> neighbor peaks; indeed, for the TiO<sub>2</sub>-terminated surface, the third neighbor peak is almost completely washed out. These broad peaks are indicative of the absence of a well-defined crystallographic TiO<sub>2</sub> phase. Another feature in Figure 3-6 B is the emergence of a shoulder at approximately 3.7 Å; this distance is similar to that of the second neighbor peak of bulk anatase.

Table 3-1 Nearest neighbor distances of Ti with O for bulk STO, rutile, and anatase.

Bulk Structure	First Nearest Neighbor Distance(s) (Å)	Second Nearest Neighbor Distance(s) (Å)	Third Nearest Neighbor Distance(s) (Å)
STO	1.96	4.38	5.87
Rutile (TiO <sub>2</sub> )	1.95, 1.99	3.49, 3.57	4.09
Anatase (TiO <sub>2</sub> )	1.94, 1.98	3.86	4.26, 4.28

### Discussion

For SrO deposition, all incident energies examined (0.1, 0.5, and 1.0 eV/atom) and both terminations (SrO and TiO<sub>2</sub>) yield layer-by-layer growth with no clustering or agglomeration, as illustrated in Figure 3-1. In Figure 3-2 it is apparent that the termination of the substrate influences the structure of the deposited film. There is no noticeable difference between the structures of the first deposited layer for the different incident energies for either termination. These findings are consistent with the results found by Kubo *et al.*<sup>57</sup> and with experiment.<sup>6, 50</sup> The SrO deposition results in Frank-Van der Merwe growth where the SrO particles impact the substrate and subsequently move to preferred adsorption sites and grow in a layer-by-layer manner. The TiO<sub>2</sub> deposited films also do not show a structural order dependence on incident energy or surface size, for the energies and size studied. The lack of variance with system size is an indication of the adequacy of the primary system size of 16 x 16. As with the SrO films, the TiO<sub>2</sub> films illustrate a termination effect with the SrO termination yielding a longer ranged ordered film.

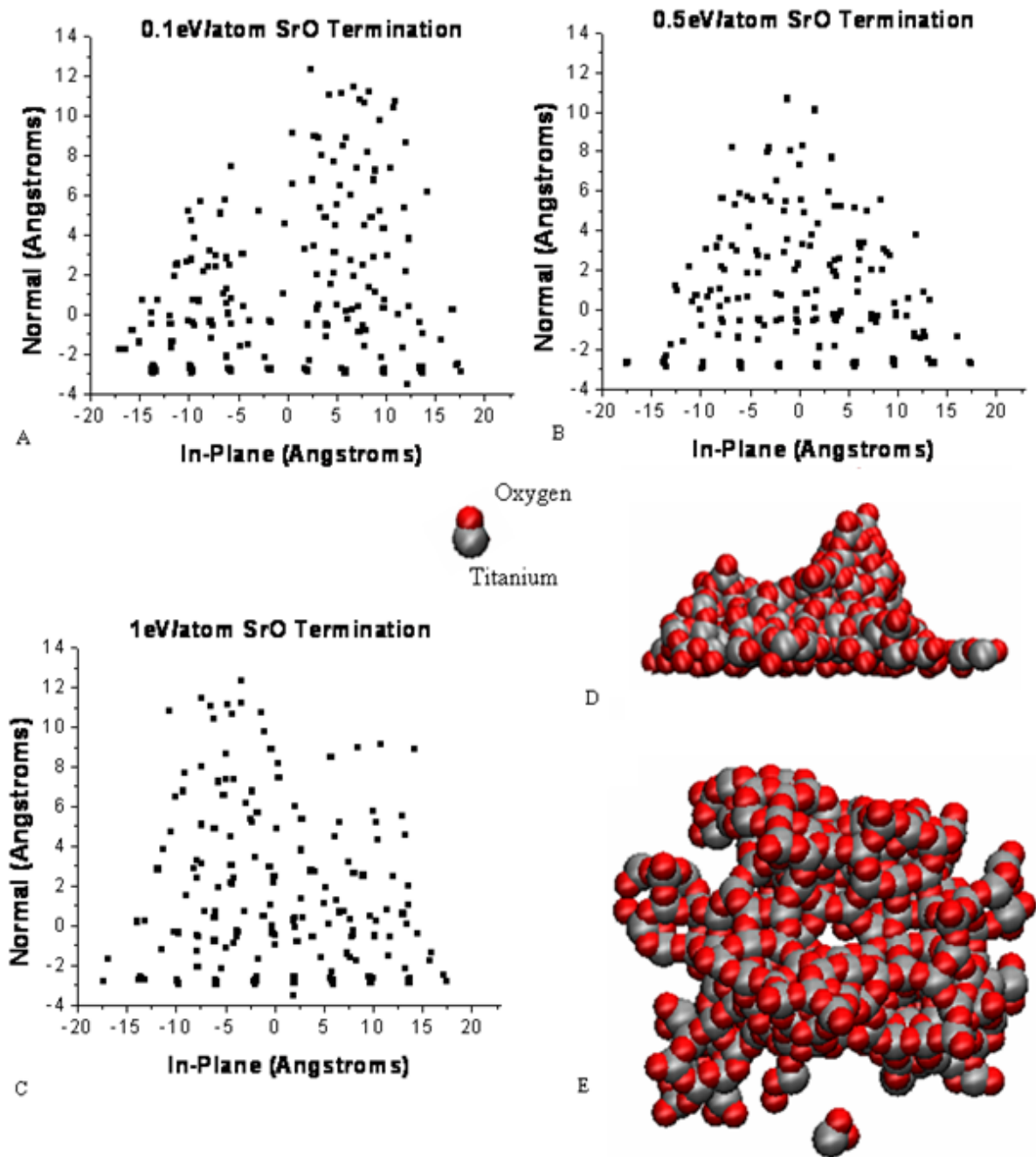


Figure 3-5 TiO<sub>2</sub> particle deposition: A)-C) represent plots of Ti atoms in the deposited film showing variations of island height with incident energy: A) 15.9 Å, B) 13.6 Å, and C) 11.5 Å for 0.1, 0.5 and 1.0 eV/atom, respectively for films deposited on SrO-terminated STO, D) and E) illustrate the top and side view morphology of the deposited film at 0.1 eV/atom on TiO<sub>2</sub>-terminated STO which is characteristic of the morphology found in all the deposited films.

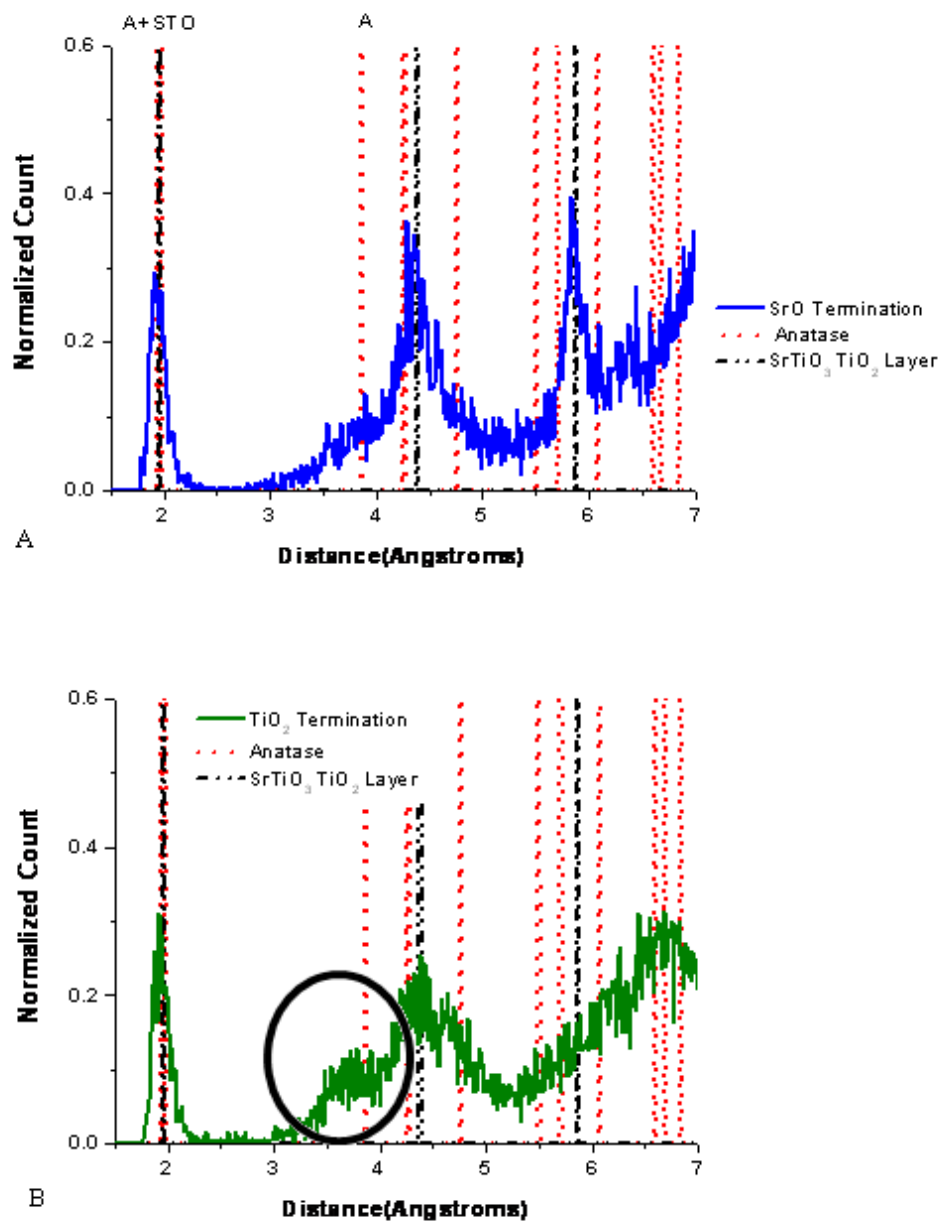


Figure 3-6 Ti-O PDF showing the influence of termination layer, A) SrO termination and B) TiO<sub>2</sub> termination, on film structure where the TiO<sub>2</sub> film on SrO-terminated substrate has a longer ranged order compared to the deposited film on the TiO<sub>2</sub>-terminated substrate.

It has been experimentally demonstrated that TiO<sub>2</sub> deposited on STO does not produce smooth, layer-by-layer, ordered, single-crystalline films at high growth rates; indeed, the exact form of the deposited TiO<sub>2</sub> varies with deposition conditions. For example, one study found

rough surfaces and possible rutile inclusions present for anatase TiO<sub>2</sub> thin films deposited on STO substrates; in contrast, surfaces were smooth and films had higher crystallinity for deposition on LaAlO<sub>3</sub> using MBE in pure ozone ambients.<sup>124</sup> One study depositing TiO<sub>2</sub> on STO using laser-MBE found a transition from island growth to 2D growth around 3 nm, illustrating a possible link between the current observations and experiment.<sup>125</sup> Deposition rate is known to have a large effect on film quality.<sup>126</sup> Layer-by-layer growth of anatase films were successfully grown on Nb-doped STO in an oxygen rich atmosphere using OPAMBE with a growth rate of 0.03 Å/sec<sup>53</sup>. Comparing to the simulated growth rate of  $1 \times 10^{10}$  Å/s, this gives insight into the impact of deposition rate on the morphology and growth modes seen in this study. Additionally, it was found that the presence of islands is ‘expected and consistently observed’<sup>127</sup> for anatase TiO<sub>2</sub> grown on STO(001) using oxygen plasma assisted MBE. Furthermore, with higher growth rates, multiphase, polycrystalline films are created.<sup>127</sup> Even though single crystalline anatase TiO<sub>2</sub> films have been successfully grown on LaAlO<sub>3</sub>, approximately 2 nm thick amorphous regions were observed.<sup>127</sup> Each of these experimental studies indicates a strong dependence on growth rate and therefore can indicate the importance of diffusion between deposition events; however, the experimental growth rates are considerably slower than are accessible to simulation. Moreover, the simulations show strong adhesion of the TiO<sub>2</sub> particles to the STO substrate on impact.

The TiO<sub>2</sub>-deposited film morphology observed in the simulations corresponds to island build up which is analogous to the three-dimensional, Volmer-Weber growth mode, as illustrated in Figure 3-6. Although the films appear to have amorphous qualities, the structural analysis indicates some crystalline behavior due to the presence of additional neighbor peaks not seen in

amorphous bulk phase PDF. The morphology of the deposited films is consistent with the growth of polycrystalline, multiphase films found in experiment.<sup>124</sup>

When the incident particles begin to interact with the substrate, both TiO<sub>2</sub> and SrO particles reorient within the beam such that the oxygen atom faces the metal atom and vice versa. However, following initial impact the particles behave in vastly different ways. The simulations indicate that Volmer-Weber growth mode dominates because the deposited TiO<sub>2</sub> particles move very little from their initial, random impact site. In contrast, the SrO particles are mobile enough following impact to produce layer-by-layer growth.

In order to further analyze the differences between the growth modes of SrO and TiO<sub>2</sub> thin films, the work of adhesion ( $W_{ad}$ ) of each on STO were calculated. The work of adhesion is the energy required to separate a perfect thin film of material from the substrate, and is calculated by subtracting the total energy of the thin film on the substrate in vacuum from the total energies of the thin film in vacuum and substrate in vacuum:

$$W_{ad} = E_{film} + E_{substrate} - E_{film+substrate} \quad (3-1)$$

For this analysis it is sufficient to treat the film and film/substrate systems as ideal and only relax the system at 0 K. Due to statistical variations among the total energies of the relaxed systems, a linear fit of layer thickness versus energy is used to obtain  $E_{substrate}$  and  $E_{film+substrate}$ . The larger the  $W_{ad}$  the more work needed to separate the film from the substrate.

The calculated works of adhesion are given in Table 3-2. Not surprisingly, the results indicate that the anatase film adheres more strongly to STO than does rutile; this is due to the smaller lattice mismatch between anatase and the substrate (anatase~3%, rutile~15%). The SrO film has a higher  $W_{ad}$  on the TiO<sub>2</sub>-terminated substrate than on the SrO-terminated substrate. It also has an overall lower  $W_{ad}$  than anatase, which is an indicator of the higher wettability of TiO<sub>2</sub>

with the STO substrate. However, the larger calculated cohesive energy associated with the TiO<sub>2</sub> polymorphs, seen in Table 2-3 (Anatase: 56.13 eV/TiO<sub>2</sub>; Rutile: 44.34 eV/TiO<sub>2</sub>), compared to the cohesive energy of SrO (12.54 eV/SrO), is believed to be responsible for the three-dimensional growth of deposited TiO<sub>2</sub> particles. The difference in the interaction of a single TiO<sub>2</sub> particle with the substrate and a single SrO particle with the substrate is calculated to be approximately 0.7 eV, with the TiO<sub>2</sub> particle having a considerably stronger interaction of -2.5 eV. The energy barriers associated with particle motion on the substrate were also examined. TiO<sub>2</sub> is predicted to have larger diffusion barriers with a minimum of 0.5 eV compared to SrO, which has a minimum diffusion barrier of 0.1 eV.

Table 3-2 Comparison of the works of adhesion of anatase TiO<sub>2</sub>, rutile TiO<sub>2</sub>, and rocksalt SrO, respectively, on STO.

Anatase 3.09% Strain		Rutile 4.97% Strain	
SrO Termination 6.71 J/m <sup>2</sup>	TiO <sub>2</sub> Termination 4.93 J/m <sup>2</sup>	SrO Termination 0.750 J/m <sup>2</sup>	TiO <sub>2</sub> Termination 1.10 J/m <sup>2</sup>
Rocksalt			
-6.54% Strain		1.24% Strain	
SrO Termination 0.429 J/m <sup>2</sup>	TiO <sub>2</sub> Termination 1.33 J/m <sup>2</sup>	SrO Termination Dissociated	TiO <sub>2</sub> Termination 0.297 J/m <sup>2</sup>

To further elucidate the growth modes exhibited in SrO and TiO<sub>2</sub> deposition, the mobility of a single SrO or TiO<sub>2</sub> particle on both SrO and TiO<sub>2</sub> terminations was calculated for several temperatures. Diffusion coefficients were calculated from the slope of the mean square displacement (MSD) curve shown in Figure 3-7. These coefficients are reported in Table 3-3, which confirms that the SrO molecules are more mobile than the TiO<sub>2</sub> particles. In fact, starting at a temperature of 1800 K, which is lower than the experimental melting temperature of 2353 K, the SrO particle desorbs from the SrO-terminated STO. The data in Table 3-3 coincide with the

interaction energies of the two particles, with the higher interaction energies giving lower particle mobility. The higher mobility of the SrO is the origin of the layer-by-layer growth observed in the simulations for the SrO thin-film deposition while the lower mobility of the TiO<sub>2</sub> particle explains the three-dimensional growth seen in TiO<sub>2</sub> deposition.

### **Conclusions**

In conclusion, MD simulations have been used to examine the growth of SrO and TiO<sub>2</sub> thin films on STO substrates. The results indicate that SrO grows in a layer-by-layer manner that agrees well with experimental data. Structural analysis illustrates a shift from the perfect SrO layer structure found in STO to the SrO rocksalt planar structure as the number of deposited layers increase. Surface termination has been shown to significantly correlate to the deposited film structural order, with the SrO film deposited on the TiO<sub>2</sub> termination having a structure more closely resembling an SrO layer in STO. In contrast, TiO<sub>2</sub> deposition yields three-dimensional island/agglomerate growth at all incident energies for both STO terminations. This type of growth is consistent with experimental results for films grown at high deposition rates. Mobility data, work of adhesion results, and particle interaction energies elucidate the causes of the differing growth modes exhibited in SrO and TiO<sub>2</sub> deposition. The stronger interaction of the TiO<sub>2</sub> particle with the substrate explains the predicted three-dimensional growth, while the weaker interaction of the SrO particle permits the deposited SrO to move, upon deposition, about the substrate to preferable adsorption sites and grow in a layer-by-layer fashion.

Table 3-3 Diffusion coefficients (D) of an SrO or TiO<sub>2</sub> particle on each STO termination. Units are  $D \times 10^9 \text{ m}^2/\text{s}$ .

Temperature (K)	SrO Particle		TiO <sub>2</sub> Particle	
	TiO <sub>2</sub> Termination	SrO Termination	TiO <sub>2</sub> Termination	SrO Termination
973	2.75	3.62	1.75	3.00
1100	3.50	3.70	1.75	2.75
1300	4.17	4.30	1.92	3.88
1500	4.58	5.25	2.42	4.00
1700	5.33	5.75	2.92	4.38
1800	6.50	Desorption	3.17	5.00
1900	6.63		3.58	5.13
2000	6.67		4.00	5.50
2100	7.13		4.00	5.60
2200	7.25		4.25	5.63
2300	7.75		4.25	6.50
2400	8.13		4.75	8.00
2500	8.00		5.75	6.50

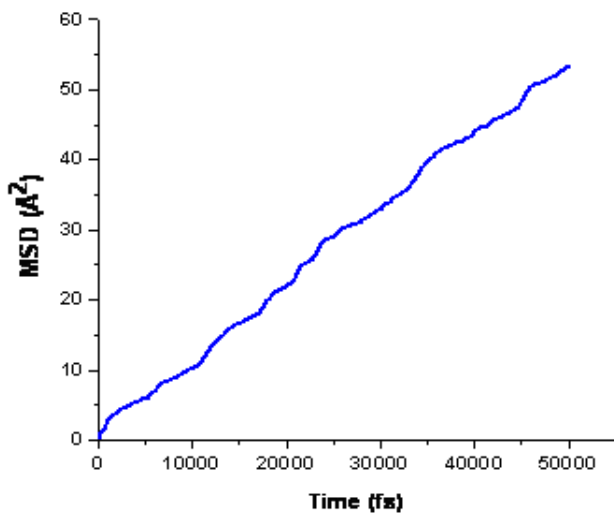


Figure 3-7 Mean square displacement (MSD) curve for an SrO particle on TiO<sub>2</sub> terminated STO at 973 K showing the adequate linearity needed to calculate the diffusion coefficient from the slope of the curve.

## CHAPTER 4 PARTICULATE DEPOSITION OF HOMOEPITAXIAL STRONTIUM TITANATE THIN FILMS

After gaining an understanding of the fundamental processes that occur during the deposition of STO component oxides, homoepitaxial STO thin films are deposited using SrO and TiO<sub>2</sub> particles. Two deposition schemes are evaluated, depositing alternating particles in a single beam and depositing alternating monolayers. The following deposition simulations were performed under my supervision and guidance by an undergraduate I mentored, Cosima Boswell.

### **Simulation Set-up**

Similar to the previous study of SrO and TiO<sub>2</sub> thin film deposition, STO deposition involves a substrate and beam of incident particles. The beam consists of a column of SrO and TiO<sub>2</sub> particles that land randomly on the deposition area and are separated from each other by  $\sim 30 \text{ \AA}$  in the direction perpendicular to the surface, such that there is some time for equilibration between each impact event. To model deposition conditions with incident energies of 0.1, 0.5, or 1.0 eV/atom, the particles are assigned corresponding velocities normal to the substrate as with the previous study. Two types of beams are created to model different deposition schemes, one where SrO and TiO<sub>2</sub> particles alternate within the beam (alternating particle deposition, APD) and one that consists of alternating monolayers of SrO and TiO<sub>2</sub> (alternating monolayer deposition, AMD). Each case results in stoichiometric STO thin films.

For APD, 60 particles are deposited, after which the system is equilibrated at 1100 K for 50 ps, which is sufficient time for the substrate to dissipate excess kinetic energy. This process is then repeated until a total of 200 particles (100 SrO and 100 TiO<sub>2</sub>) are deposited on the substrate which would correspond to approximately 4 layers of STO if perfect layer-by-layer growth was achieved. Following deposition, the system temperature is increased to a final temperature of 2000 K ramping from 1000 K to 2000 K at 100 degree intervals. This process takes

approximately 340 ps including a hold at 2000 K for ~100 ps with subsequent quenching of the system to remove thermal fluctuations, thereby simplifying the subsequent structural analysis.

As with the APD, AMD results in an overall 1:1 composition of SrO:TiO<sub>2</sub>. This is achieved by depositing alternating monolayers of SrO and TiO<sub>2</sub>. The first monolayers deposited consists of those that would continue the layering sequence of bulk STO, i.e., SrO particles are deposited on the TiO<sub>2</sub>-terminated substrate and TiO<sub>2</sub> particles are deposited on the SrO-terminated substrate. After one monolayer is deposited, the film is relaxed at 1100 K for 50 ps and then the second monolayer is deposited. This process is repeated until a total of 4 monolayers are deposited (2 TiO<sub>2</sub> monolayers and 2 SrO monolayers), and the system is equilibrated as described previously. Some simulations were repeated to determine statistical differences in the simulated depositions. The structures of the films, as determined with pair distribution functions, are essentially identical for the repeated simulations. However, the difference in the cation layering, described by the percentage of metal atoms (either Sr or Ti) located within each layer of each film, ranges from approximately 5 to 20% between the repeated simulations.

## **Results**

### **Alternating Particle Deposition**

The simulations of APD were performed at multiple incident energies on both SrO- and TiO<sub>2</sub>-terminated STO substrates. Representative films that were deposited at 0.1 eV/atom incident energy are shown in Figure 4-1, where the layers are rendered separated from one another to better illustrate their composition and ordering. Visual inspection of these layers provides an initial indication of the degree of ordering and cation layering of the deposited films.

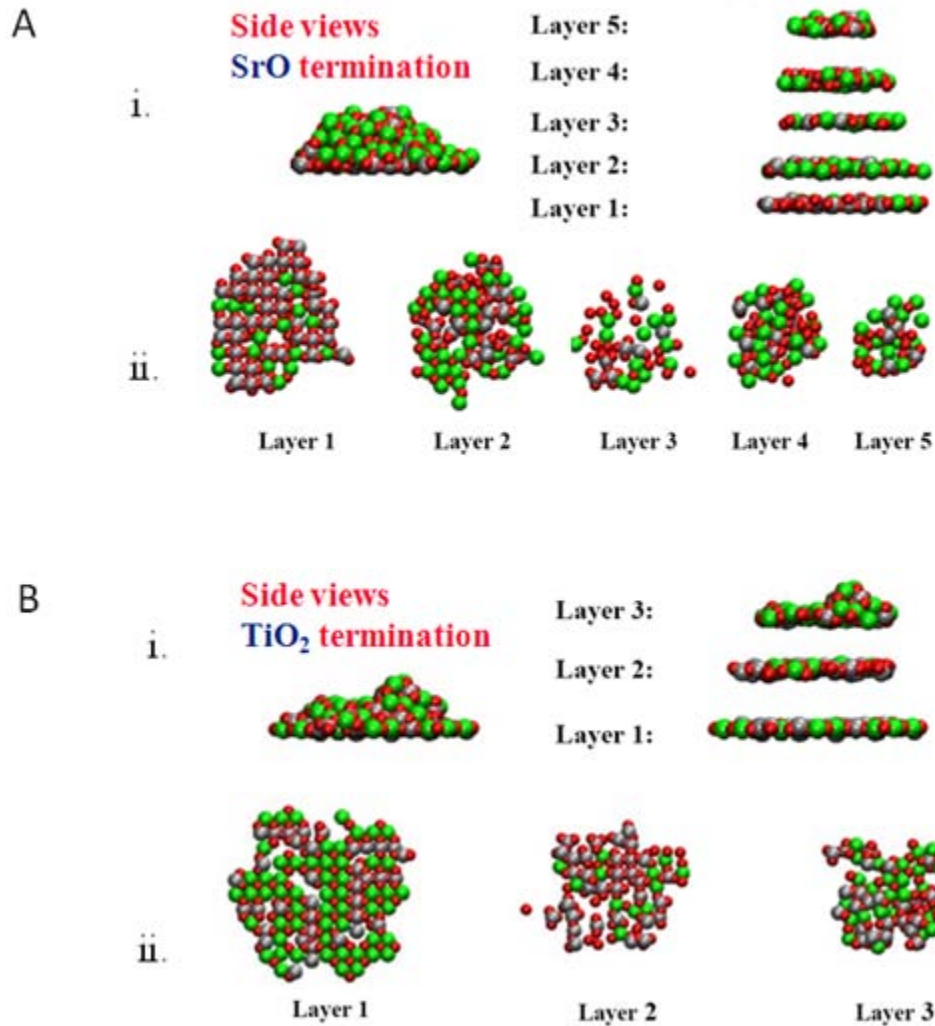


Figure 4-1 Alternating particle deposition exhibits cation layering. A) SrO termination: (i) Side view and assigned layers of 200 species deposited with an incident energy of 0.1 eV/atom. (ii) Bottom-up view of layers 1–5. B) TiO<sub>2</sub> termination: (i) Side view and assigned layers of 200 species deposited with an incident energy of 0.1 eV/atom. (ii) Bottom-up view of layers 1–3.

As illustrated in Figure 4-1, the thin film on the SrO-terminated substrate consists of five layers, whereas although the film deposited onto the TiO<sub>2</sub>-terminated substrate contains the same number of particles, it consists of only three layers. This is attributed to the fact that the first layer on TiO<sub>2</sub>-terminated STO is comprised primarily of SrO particles that have higher mobility than TiO<sub>2</sub> particles. This was discussed in the previous chapter. The SrO particles therefore

spread over a relatively larger surface area, reducing the number of layers in the film deposited on the  $\text{TiO}_2$  termination but increasing the number of atoms within each layer. In contrast, the first layer on the SrO-terminated substrate is comprised of mainly  $\text{TiO}_2$  particles that are more likely to adhere to wherever they first impact the surface due to their higher interaction energy. Consequently, the resulting film will have more layers with fewer atoms within each layer relative to the film on the  $\text{TiO}_2$ -terminated substrate.

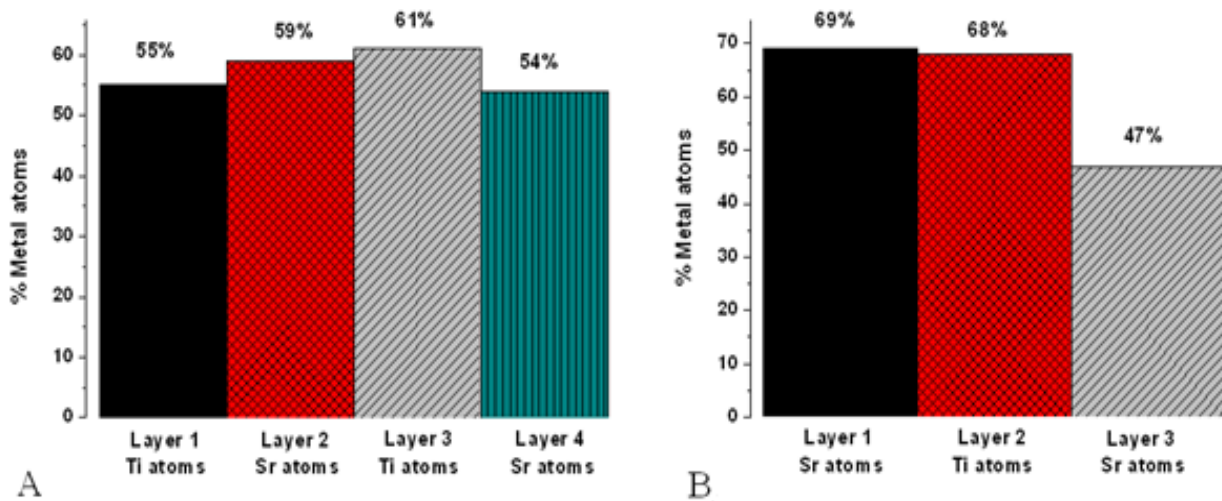


Figure 4-2 APD metal atom percentages. A) Percentage of the identity of the alternating particles deposited onto SrO-terminated STO starting with layer 1 (Ti percentage) and ending with layer 4 (Sr percentage). B) Percentage of the identity of the alternating particles deposited onto  $\text{TiO}_2$ -terminated STO starting with layer 1 (Sr percentage) and ending with layer 3 (Sr percentage).

Cation layering is quantified by calculating the percentage of each type of metal atom within each layer; these results for a representative case of 1.0 eV/atom incident energy are provided in Figure 4-2. In each case, the percentage of metal atoms (Sr or Ti) present in each layer is used as a measure of layer segregation within the film and the extent to which the atomic arrangement in the films matches that of bulk STO, which consists of alternating planes of SrO and  $\text{TiO}_2$ . In particular, Figure 4-2 A displays the percentages of cations expected in layers 1-4 (Ti, Sr, Ti, and Sr, respectively) for the film deposited on  $\text{TiO}_2$ -terminated STO. Figure 4-2 B

displays the percentages of Sr, Ti, and Sr atoms in layers 1-3, respectively, for films deposited on SrO-terminated STO. The results indicate that the expected majority metal atom in each layer is consistent with what one would expect in bulk STO.

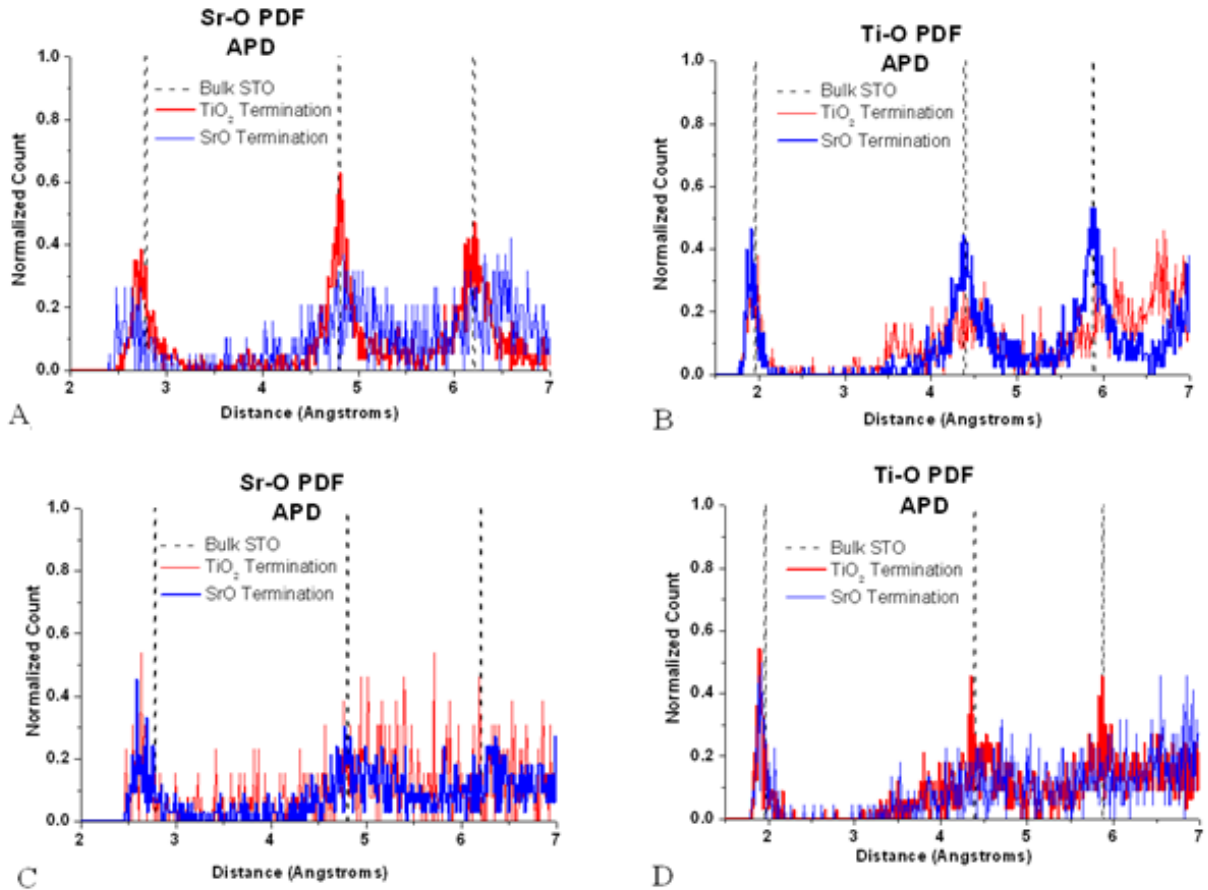


Figure 4-3 Pair distribution functions for alternating particle deposition. A) Sr-O PDF for first layer APD film that shows the highest degree of order for the film deposited on  $\text{TiO}_2$ -terminated STO. B) Ti-O PDF for first layer APD film that shows the film on SrO-terminated STO yields an ordered structure similar to that of bulk STO. C) Sr-O PDF for the second layer APD film that shows that neither termination yields ordering similar to that of bulk STO. D) Ti-O PDF for second layer APD film that shows that only the film deposited on  $\text{TiO}_2$ -terminated STO yields an ordered structure similar to that of bulk STO.

To illustrate the degree of structural order within the layers in more detail, three-dimensional plane-by-plane pair distribution functions (PDFs) are determined within each deposited layer. A Sr-O PDF, for example, shows the distances between each Sr atom in that

layer and neighboring O atoms. Each PDF is then compared to the PDF of the corresponding layer in bulk STO. Figure 4-3 summarizes the Sr-O and Ti-O PDFs for both the first and second APD layers that were deposited with representative energies of 0.1 eV/atom. As illustrated in Figure 4-3 A, layer 1 of the film deposited on the TiO<sub>2</sub>-terminated substrate shows close agreement with the Sr-O PDF of bulk STO, whereas layer 1 of the SrO-terminated deposition (Figure 4-3 B) matches the Ti-O nearest neighbor peaks in bulk STO. Resulting PDFs for layer 2 also show the expected trend. Here, the SrO-terminated deposition (Figure 4-3 C) Sr-O PDF shows closer agreement to bulk STO, while in the TiO<sub>2</sub>-terminated deposition, the Ti-O PDF (Figure 4-3 D) correlates with the Ti-O PDF of bulk STO. These results are consistent with the natural layering sequence of STO and are an indication of layer-by-layer growth of the deposited films. However, closer agreement with the corresponding bulk PDFs is observed within the film deposited on the TiO<sub>2</sub>-terminated substrate indicating superior layer-by-layer growth on this termination.

### **Alternating Monolayer Deposition**

Next, the simulations considered alternating monolayer deposition (AMD). AMD is analogous to molecular beam epitaxy (MBE) due to the similarities in incident species with MBE depositing elemental species in a monolayer fashion. Representative films produced by AMD with incident energies of 1.0 eV/atom on SrO- and TiO<sub>2</sub>-terminated STO are shown in Figure 4-4. Similar to APD, the film deposited on the TiO<sub>2</sub> termination covers a larger surface area compared to the film on SrO termination.

The percentages of metal atoms in each layer are indicated in Figure 4-5. The metal atoms in layer 1 of the film deposited on SrO-terminated STO, which is expected to consist of 100% Ti in the form of TiO<sub>2</sub>, is in fact 69% Ti. Interestingly, layer 2 has a smaller majority (58%) of Sr atoms in the form of SrO. The metal atom percentages of the film deposited on the TiO<sub>2</sub>-

terminated STO indicate that this film is substantially more ordered. In particular, 89% of the metal atoms in the first layer are Sr in the form of SrO, while 100% of the metal atoms in the second layer are Ti in the form of TiO<sub>2</sub>.

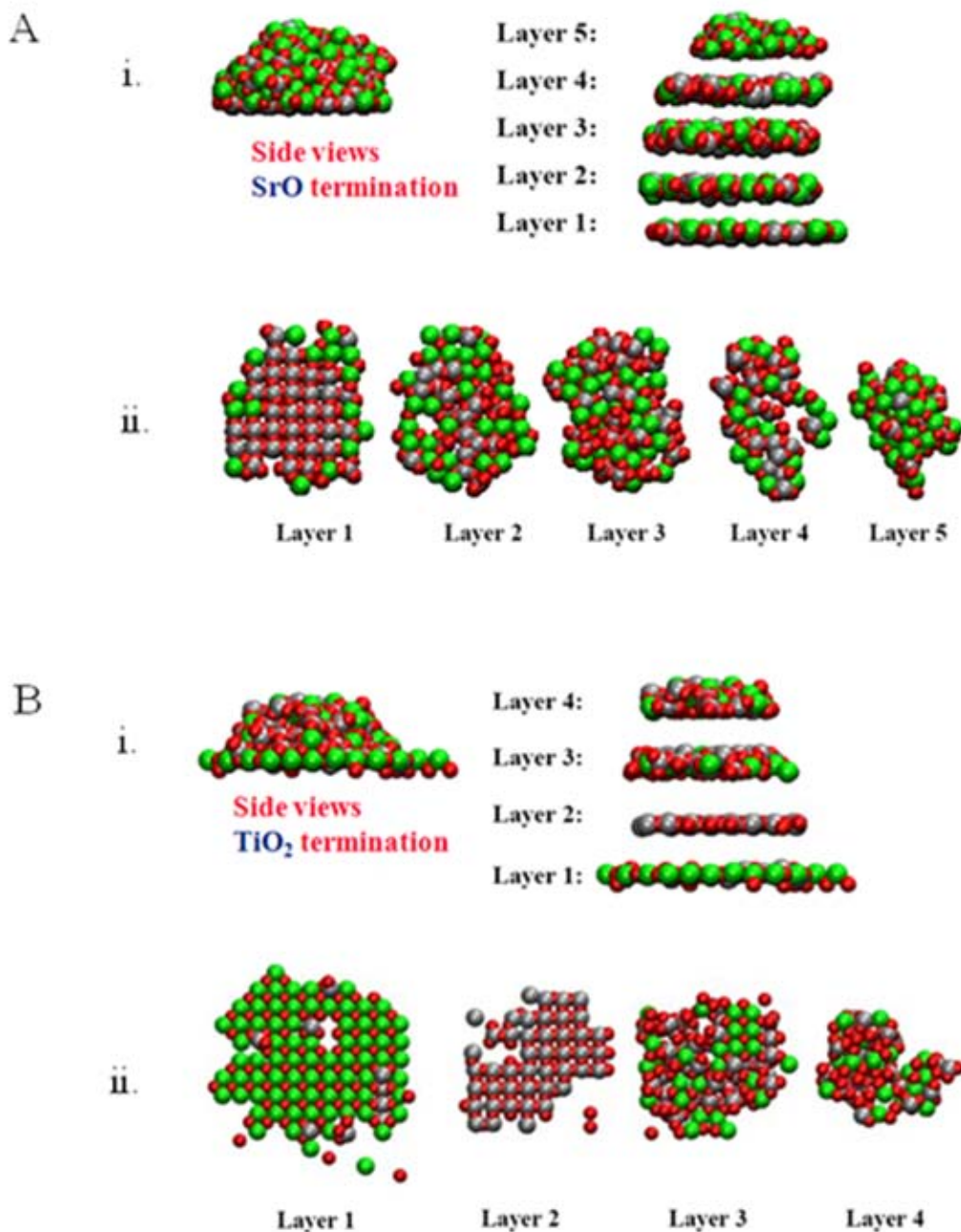


Figure 4-4 Alternating monolayer deposition. A) SrO-terminated STO: i) Side view and assigned layers; ii) Bottom-up views. B) TiO<sub>2</sub>-terminated STO: i) Side view and assigned layers; ii) Bottom-up view. Green-Sr; Red-O; Silver-Ti

PDFs of the first layer of each monolayer deposition are given in Figures 4-6 A and 4-6 B. As expected, the first layer of the film deposited on the  $\text{TiO}_2$ -terminated substrate shows close agreement with the nearest neighbor Sr-O peaks of bulk STO, whereas the first layer of the SrO-terminated deposition shows closer agreement with the Ti-O nearest neighbor peaks. PDFs of layer 2 are given in Figures 4-6 C and 4-6 D. Since the second layer of the film deposited on the  $\text{TiO}_2$  termination consists of only Ti and O atoms, no Sr-O PDF is observed. However, it can be seen from Figure 4-6 D that this layer exhibits Ti-O peaks that closely correspond to the  $\text{TiO}_2$  layer in bulk STO. On the SrO-terminated substrate, the expected second layer is SrO; however as seen in Figure 4-6 C, this layer does not yield an ordered structure. This once again indicates superior ordering of the depositions on the  $\text{TiO}_2$ -terminated substrate.

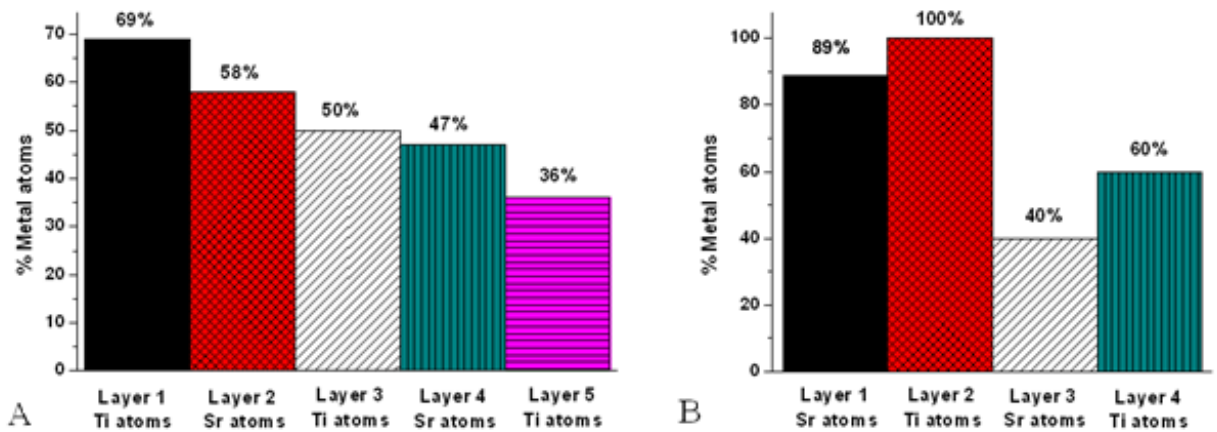


Figure 4-5 Metal atom percentages for AMD films. A) Percentage of the identity of alternating monolayers onto SrO-terminated STO starting with layer 1 (Ti percentage). B) Percentage of the identity of alternating monolayers onto  $\text{TiO}_2$ -terminated STO starting with layer 1 (Sr percentage).

### Discussion

The first layer of the APD films deposited on both substrate terminations shows a majority of the expected metal atoms and shows structural ordering that is illustrated in the PDFs. Layer 2 of the film deposited on the SrO termination shows a smaller percentage of the expected metal

atom (Sr) compared to the second layer on the TiO<sub>2</sub> termination; this is attributed to the relatively poor quality of layer 1. The first layer deposited on the TiO<sub>2</sub> termination is SrO; due to the aforementioned difference in mobility, this layer is more ordered than the first TiO<sub>2</sub> layer deposited on the SrO termination. This is consistent with experimental evidence of the importance of substrate surface quality on the deposited films<sup>128</sup>: if the surface quality is low, the quality of the deposited film will also be low. Also, although some ordering is observed in all APD films, the depositions on the TiO<sub>2</sub> termination exhibit superior ordering over SrO termination at all incident energies, suggesting a higher quality film is more likely produced when depositing on a TiO<sub>2</sub> termination due to the higher ordering of the first deposited layer.

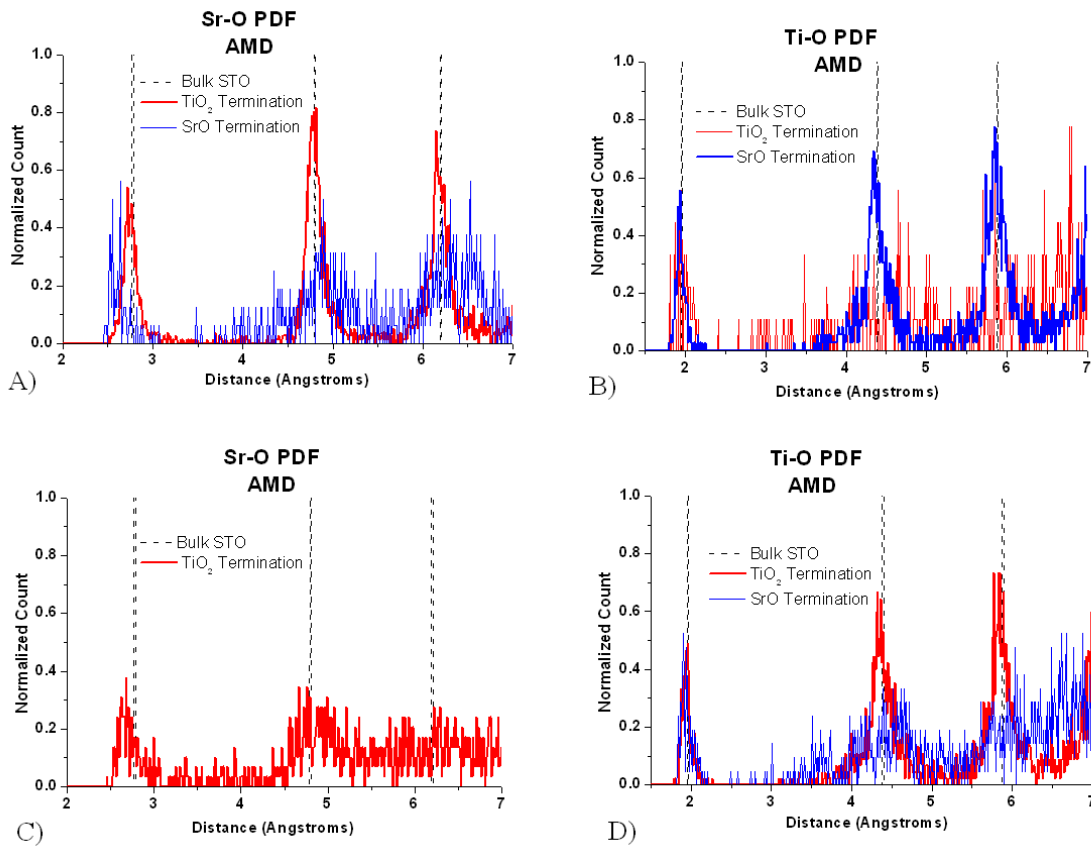


Figure 4-6 PDFs for AMD films. A) Sr-O PDF for the first layer on TiO<sub>2</sub>-terminated STO. B) Ti-O PDF for the first layer on SrO-terminated STO. C) Sr-O PDF for the second layer on TiO<sub>2</sub>-terminated STO. D) Ti-O PDF for the second layer on TiO<sub>2</sub>-terminated STO.

The first two layers of the AMD film on SrO-terminated STO consist of a majority of expected metal atoms indicating STO-type cation layering. Additionally, the pair distribution functions of the first two layers coincide with the bulk structure found in STO. However, subsequent layers show little correlation to bulk STO, possibly due to limited diffusion of the atoms post deposition.

The influence of incident kinetic energy on the resulting APD films was also examined. The simulations indicate that the considered range of incident energy, 0.1, 0.5 and 1.0 eV/atom, has no significant effect on the overall structure of the deposited films as evidenced by the PDFs. Additional simulations were performed on select incident energy depositions; these resulted in essentially identical PDFs but a 5-20% spread in the metal atom percentages within each layer. It was also noted that the SrO termination exhibited a ~6% standard deviation in the metal atom percentage in layer one whereas TiO<sub>2</sub> termination had a ~4% standard deviation. The overall film structure is qualitatively described as partially ordered with significant variation in the cation ordering within the film being observed for alternating particle depositions. However, there is no evidence that incident energy controls segregation, which is mainly controlled by substrate termination and whether alternating particles or alternating monolayers are deposited.

The large percentages of expected metal atoms present in each layer of the film deposited on TiO<sub>2</sub>-terminated STO and the high degree of order illustrated in the PDFs indicates that monolayer deposition on TiO<sub>2</sub>-terminated substrates results in layer-by-layer growth within the first few deposited monolayers. Once again this is attributable to the higher mobility of the SrO particles. Overall, better agreement with bulk-like structures is found for AMD compared to APD. The difference in mobility is also a reason for the higher quality films produced when depositing in a monolayer fashion as opposed to an alternating particle method. Several

experimental studies indicate the presence of islands at the initial stage of growth and the importance of diffusion and migration of the particles on the resultant films.<sup>95, 129</sup> As previously mentioned, molecular dynamics simulations are kinetically limited to 100's of ps as opposed to the seconds used to relax films experimentally as seen in RHEED analysis<sup>93, 130, 131</sup>; this is the reason only the first two layers exhibit an ordered structure similar to that of bulk STO.

### **Conclusions**

Both in monolayer and alternating particle depositions, the films deposited on TiO<sub>2</sub>-terminated STO show superior layer-by-layer growth. This is attributed to the difference in the intrinsic mobility of the two metal-oxide particles. TiO<sub>2</sub>, which has a lower mobility due to its stronger interaction with the surface, sticks wherever it impacts the substrate, whereas the higher mobility of SrO allows it to move and reorient into the preferred STO positions. This gives rise to the highest quality films deposited with AMD on TiO<sub>2</sub>-terminated STO since the first deposited species are the more mobile SrO particles. Additionally, subsequent layers deposited in this scheme are of higher quality due to the superior first layer. This work thus gives insight into the importance of surface quality on film production.

## CHAPTER 5 STRONTIUM TITANATE CLUSTER DEPOSITION

To further elucidate the initial deposition processes which occur during STO deposition, stoichiometric STO clusters of varying size are deposited on STO. Little examination of STO cluster deposition exists<sup>59, 70</sup> and the processes involved during the deposition of energetic STO clusters would provide significant insight into the pulsed laser deposition (PLD) of STO thin films. PLD involves evaporation of an STO target producing species ranging from atomic species to large molecules. Dimer and trimer (SrO and TiO<sub>2</sub>, respectively) deposition was discussed in Chapter 3 and 4; here, we continue the study to incorporate the effect of clusters on the morphology and growth of STO thin films.

### **Simulation Set-up**

The system utilized in the current study is consistent with the previous deposition simulations and uses the same substrate. Although clusters of metals and some oxides are prevalent in the literature<sup>60-64, 132-137</sup>, information on stoichiometric STO clusters is lacking. The existing studies of STO deposition use bulk-like STO clusters with similar structural parameters.<sup>59, 70</sup> Experimentally, TiO<sub>x</sub> clusters produced during Ti sputtering exist in a range of sizes with both spherical and cubic shapes depending on the oxygen partial pressure<sup>133</sup>, therefore depositing clusters with a bulk-like structure is believed to be an inadequate representation of the clusters involved in deposition. To further elucidate the initial deposition processes, stoichiometric STO clusters of varying size are deposited on the STO slab. To create the clusters that are ultimately deposited, an STO crystal was cut into one, two, three, and four-unit STO clusters. To attempt to ensure the cluster geometry is comparable to that found in the plume created during PLD, they were then equilibrated until minimal energy fluctuations were detected. This process reduces the possibility of building the STO crystal structure into the growing film

as the equilibrated clusters exhibit unique symmetry and surface-induced bond length variations as shown in Figure 5-1. The average Sr-O bond distance in all clusters is 2.6 Å compared to a bulk Sr-O distance of 2.77 Å. Clusters consisting of 2 or more STO units include two types of Ti-O bonds, Type I and Type II as shown in Table 5-1 and Figure 5-1.

For all deposition schemes studied, an incident kinetic energy of 1.0 eV/atom was allocated to each incident cluster by assigning a corresponding velocity. The particles in the beam were deposited at random orientations and positions, with respect to their center of mass, and the distance between particles was varied to better understand the effect of deposition rate.

The various systems studied are described in Table 5-2 including 6 unique deposition beams for each termination resulting in 12 unique systems. To analyze the effect of cluster size distribution, films were deposited by mono-sized clusters and mixtures of one-, two-, three- and four-unit STO clusters along with SrO and TiO<sub>2</sub> particles in a random sequence. In addition to the unique beams, some systems were repeated, changing the distance between each deposition event, as indicated in Table 5-2, to evaluate the impact of deposition rate. For 3-STO clusters the distance between particles was varied from 20 Å to 90 Å and 200 Å. Furthermore, 1 and 4-unit STO mono-beam deposition and the mixed-beam depositions were repeated for a total of 5 simulations each. No structural variance was seen and the quantitative film composition analysis yielded a 4-18% variance between the repeated simulations on TiO<sub>2</sub> termination and 8-25% variance between repeated simulations on SrO termination.

After depositing approximately 200 atoms (40 1-unit STO, 20 2-unit STO, 15 3-unit STO, 5 4-unit STO) the system was allowed to equilibrate at an elevated temperature of 1100 K for approximately 50 ps to allow the films to relax and after approximately 100-STO units,

corresponding to 4 ML (2 SrO, 2 TiO<sub>2</sub>), were deposited the system was ramped to 2000 K and held for 300 ps and then quenched to 0 K to eliminate thermal effects for analysis purposes.

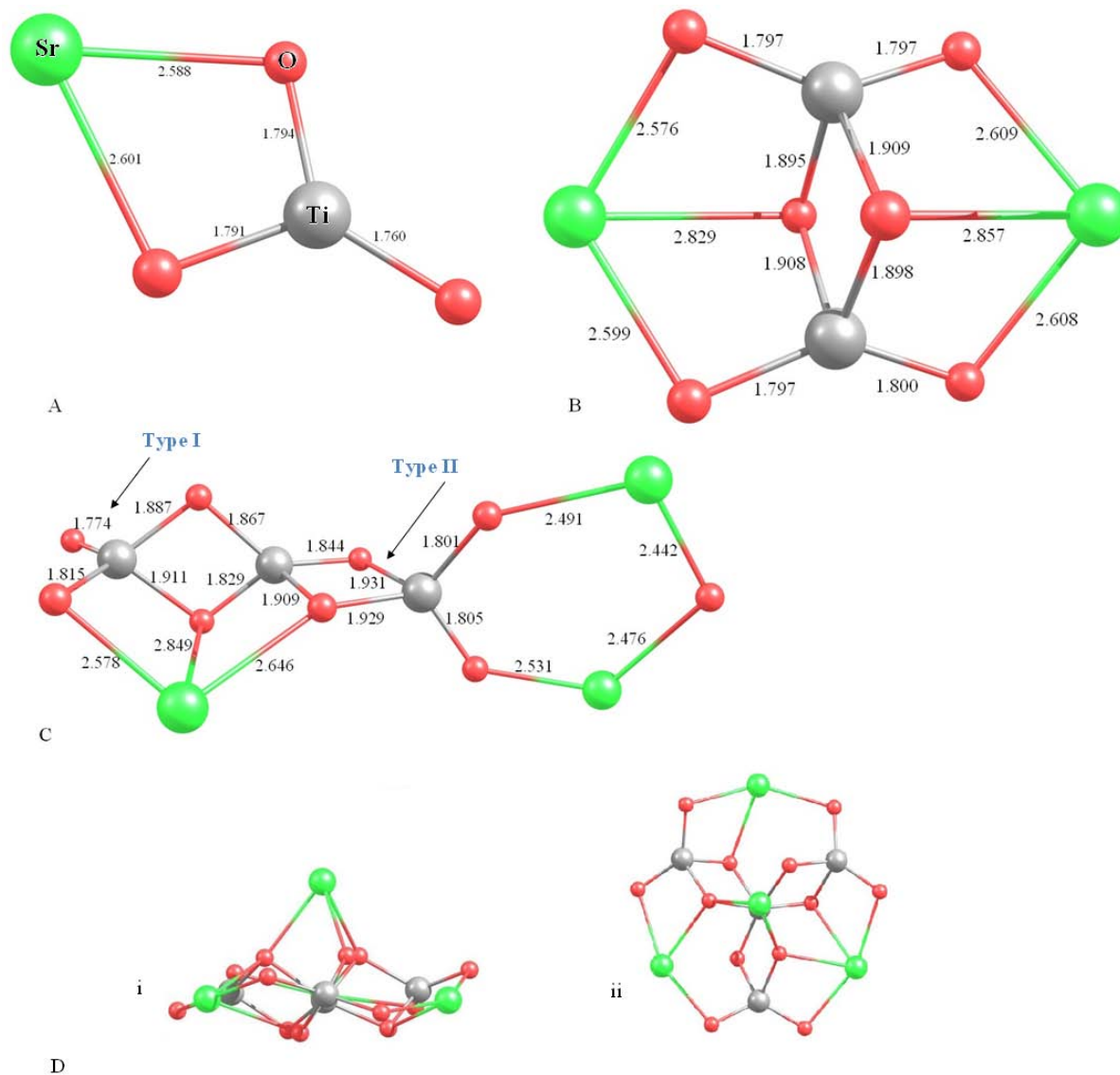


Figure 5-1 STO cluster geometries displaying bond-lengths and symmetry. A) 1 unit STO, B) 2 unit STO, C) 3 unit STO, D) 4 Unit STO (i: side, ii: top-down)

Table 5-1 Average Ti-O bonding in STO clusters compared to bulk STO.

	Ti-O Type I	Ti-O Type II	Ti-O in Bulk STO
Bond Length	1.9 Å	1.7 Å	1.95 Å
Coordination of O with Ti	2	1	2

Table 5-2 Cluster deposition schemes investigated. Each scheme was repeated for each termination. Subsections indicate simulations comparing different separation distances between incident clusters to evaluate the impact of deposition rate.

Deposition Scheme		
	Cluster Size (STO units)	Separation Distance
Mono Cluster Size	1	30 Å
	2	30 Å
	3	20, 30, 60, 90 and 200Å
	4	30 Å
Mixed Cluster Size	1-4 without SrO/TiO <sub>2</sub> particles	30 Å and 60 Å
	1-4 with SrO/TiO <sub>2</sub> particles	30 Å and 60 Å

## Results

Various analysis methods have been used to both qualitatively and quantitatively describe the deposited thin films. First, snapshots of the films with layer separation qualitatively illustrate the structural order and are compared to the layering sequence in bulk STO. The percentages of metal atoms present in each layer is also calculated as an indication of mixing within each layer and illustrate possible layer composition dependence on the differing deposition schemes studied. Since STO consists of alternating SrO/TiO<sub>2</sub> planes, the metal percentages of the first deposited layer on SrO termination should have predominately Ti cations whereas the first layer on TiO<sub>2</sub> termination should contain Sr cations.

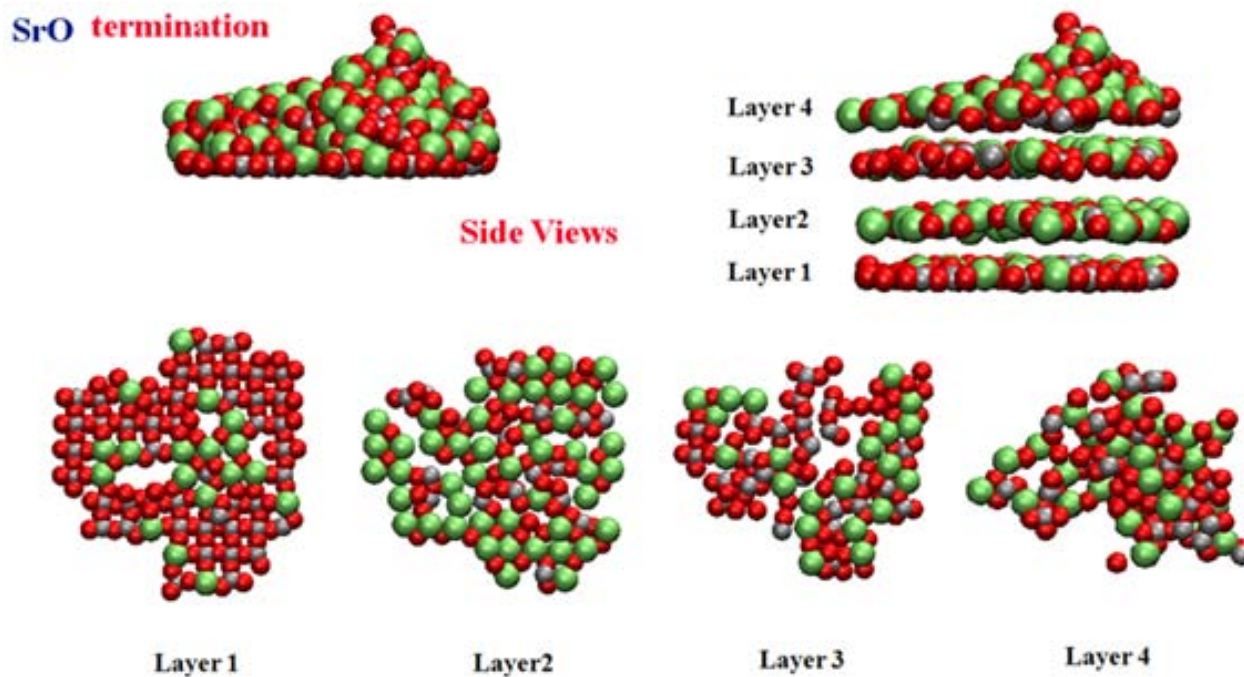


Figure 5-2 Representative snapshots of films deposited on SrO-terminated STO showing layer segregation and order within the first layer.

To quantitatively analyze the structural order of the deposited films, pair distribution functions (PDF) were calculated for each deposited layer. Ti-O PDF, for example, illustrates the nearest neighbor distances of Ti within each film with surrounding O atoms. For all film depositions, the first deposited layer produced PDFs consistent with bulk STO, meaning they had the same Sr-O and Ti-O neighbor distances as the corresponding SrO and TiO<sub>2</sub> planes in STO. The second deposited layer, however, showed deviation from bulk like structure. Therefore, the PDFs for the second deposited layer for all schemes investigated are analyzed and discussed.

STO thin films deposited on the SrO-terminated STO produced similar morphologies for each scheme, and a representative snapshot is shown in Figure 5-2 with the layers separated for visual impact. Each layer is approximately 2 Å thick, corresponding to half the lattice parameter. The figure shows areas of TiO<sub>2</sub> ordering separated by SrO molecules in the first layer with no

visually apparent order in the second deposited layer. PDFs were constructed comparing all the variables studied, including particle size, deposition rate and size distribution. A representative PDF of the second deposited layer comparing two different deposition schemes, mono-sized and mixed-sized deposition, is illustrated in Figure 5-3.

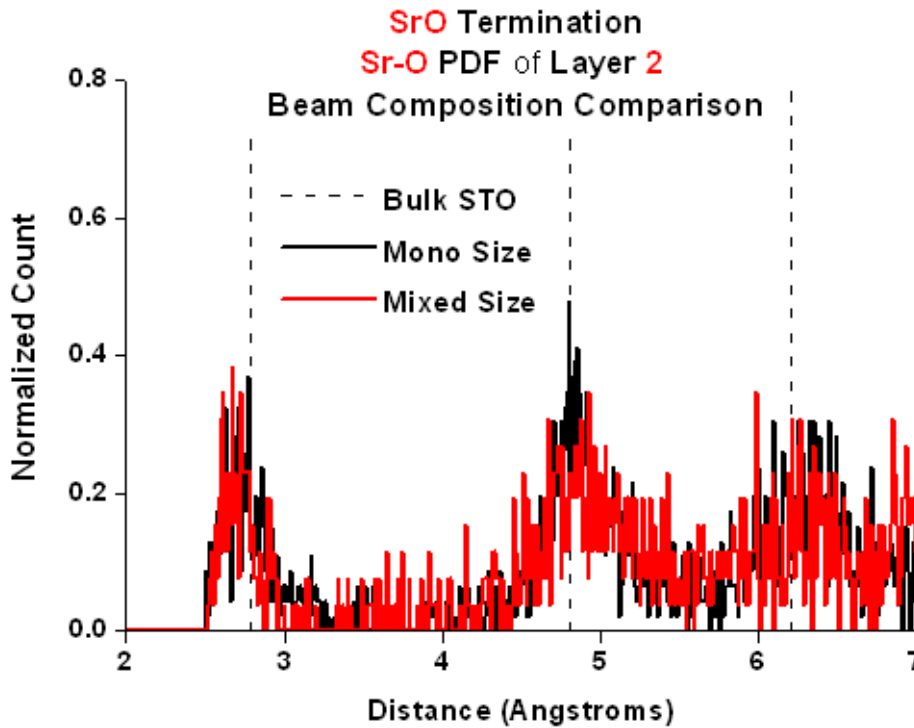


Figure 5-3 Pair distribution function of the second deposited layer comparing mono- and mixed-size cluster deposition on SrO-terminated STO illustrating the similar structural order between the two deposition methods.

Films deposited by all schemes on SrO-terminated STO have similar peaks to the Sr-O layer in bulk STO up to the second nearest neighbor, damping out significantly afterwards. Metal atom percentages, shown in Figure 5-4, also indicate no trend based on the deposition schemes studied with a 9% spread in Ti atom percentages within the first layer (Figure 5-4 A) and a 26% spread of Sr atoms present in the second deposited layer (Figure 5-4 B).

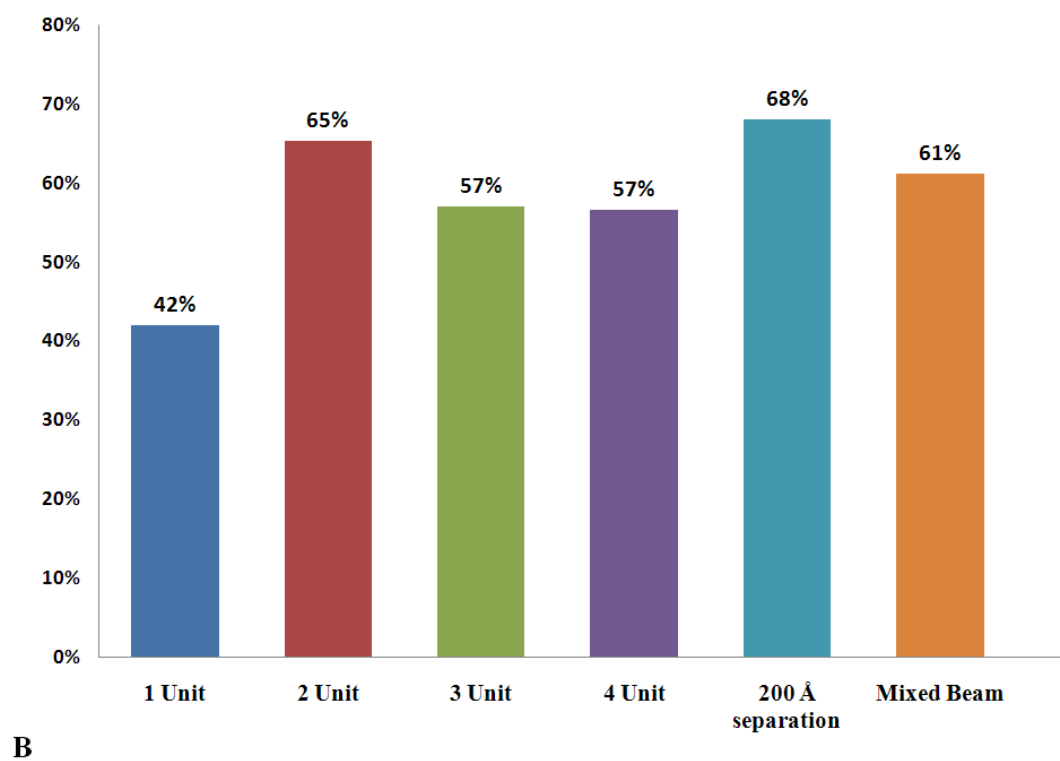
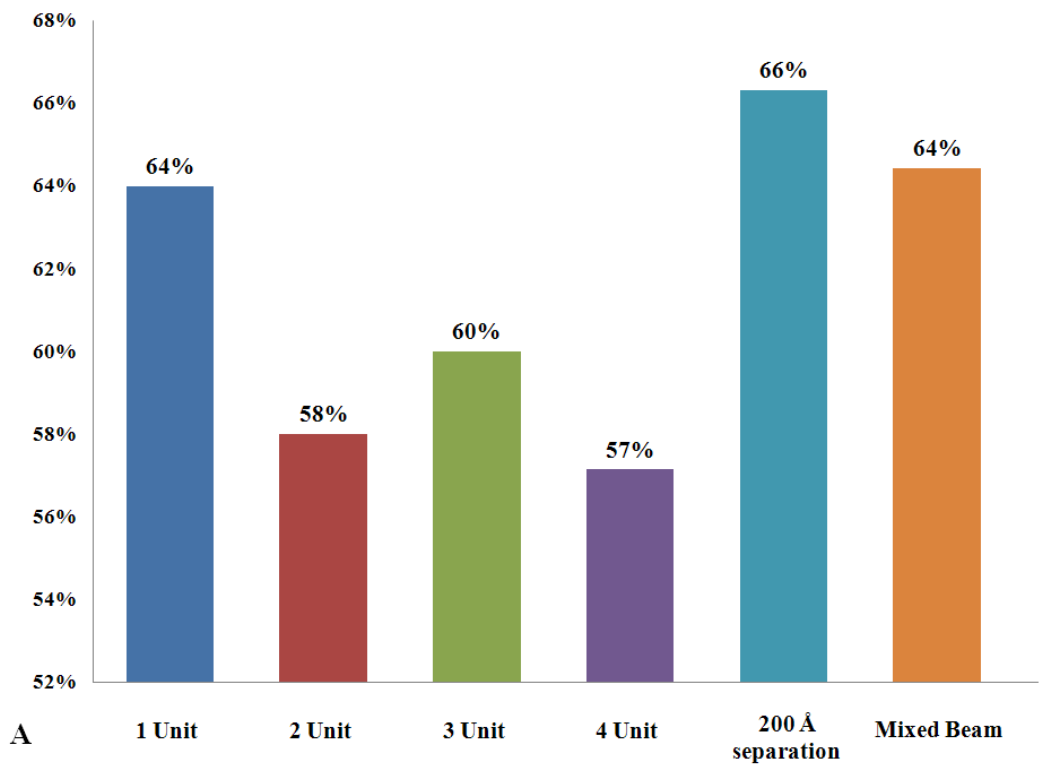


Figure 5-4 Percentage of metal atoms in the first two deposited layers on SrO-terminated STO. A) Ti atoms in first layer, B) Sr atoms in second layer.

Next, we examine films deposited on TiO<sub>2</sub>-terminated STO. A representative snapshot of the film is illustrated in Figure 5-5 where the layers are again separated to illustrate the ordering and composition of each layer. Representative Ti-O PDFs comparing films produced from mono-sized versus mixed-sized beams (shown in Figure 5-6) illustrate similar peak positions, heights and widths for each scheme. The Ti-O peaks describing the second layer are the same as those representing the TiO<sub>2</sub> planes in bulk STO.

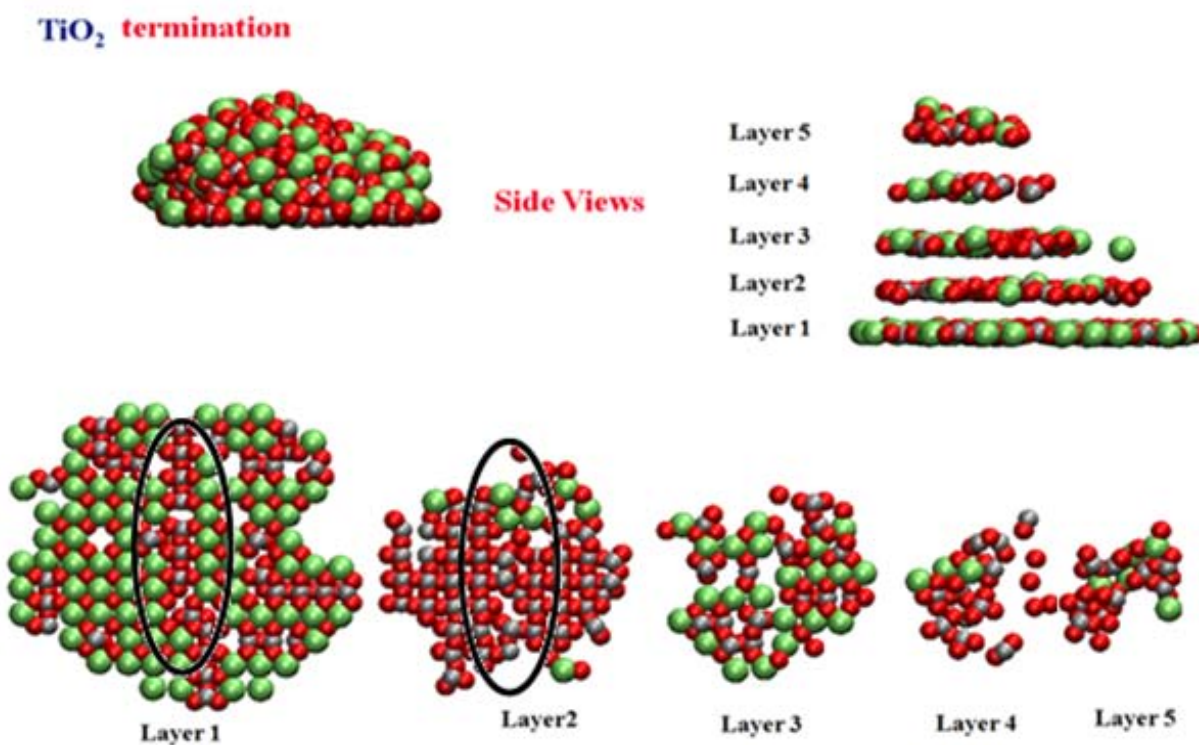


Figure 5-5 Representative snapshots of films deposited on TiO<sub>2</sub>-terminated STO showing layer segregation and order within layers one and two shown in the lower figures. The circled areas depict effect of first layer TiO<sub>2</sub> inclusions on the subsequently deposited second layer.

Metal atom percentages within the first two layers are given in Figure 5-7. The percent of Sr atoms in the first layer and Ti atoms in the second layer deviates 20% between the deposition schemes illustrated with mixed beam deposition having the highest percentage of expected metal atoms for both layers.

Upon further inspection of the snapshots of the first deposited layer of each film on  $\text{TiO}_2$ -terminated STO (Figure 5-8), the most prevalent defects observed are 4-fold site vacancies, Ti substitutions and  $\text{TiO}_2$  inclusions; these are provided in Figure 5-9. To evaluate the impact of deposition scheme on the defects described in Figure 5-9, the percentage of each defect present compared to the total 4-fold sites available is calculated and shown in Figure 5-10. Taking all defects into consideration within the first deposited layer is an indication of its structural quality and can affect the second deposited layer. This is indicated in the circled areas in Figure 5-6 where the  $\text{TiO}_2$  inclusions create regions of disorder in the second layer.

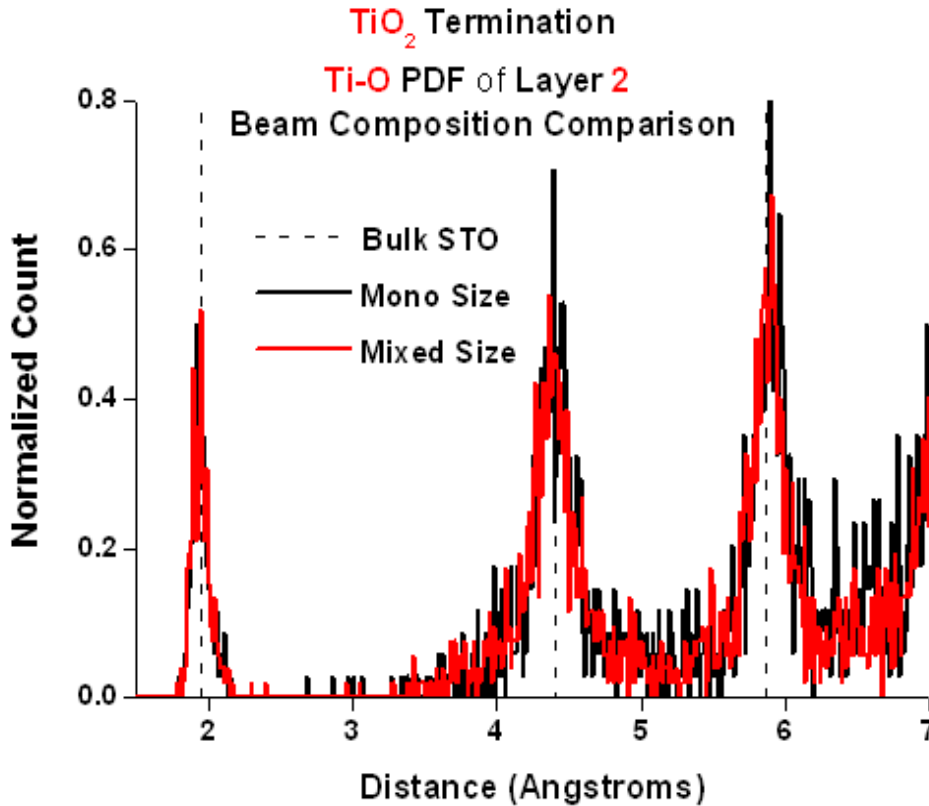


Figure 5-6 Pair distribution function of the second deposited layer comparing mono- and mixed-size cluster deposition on  $\text{TiO}_2$ -terminated STO illustrating the similar structural order between the two deposition methods.

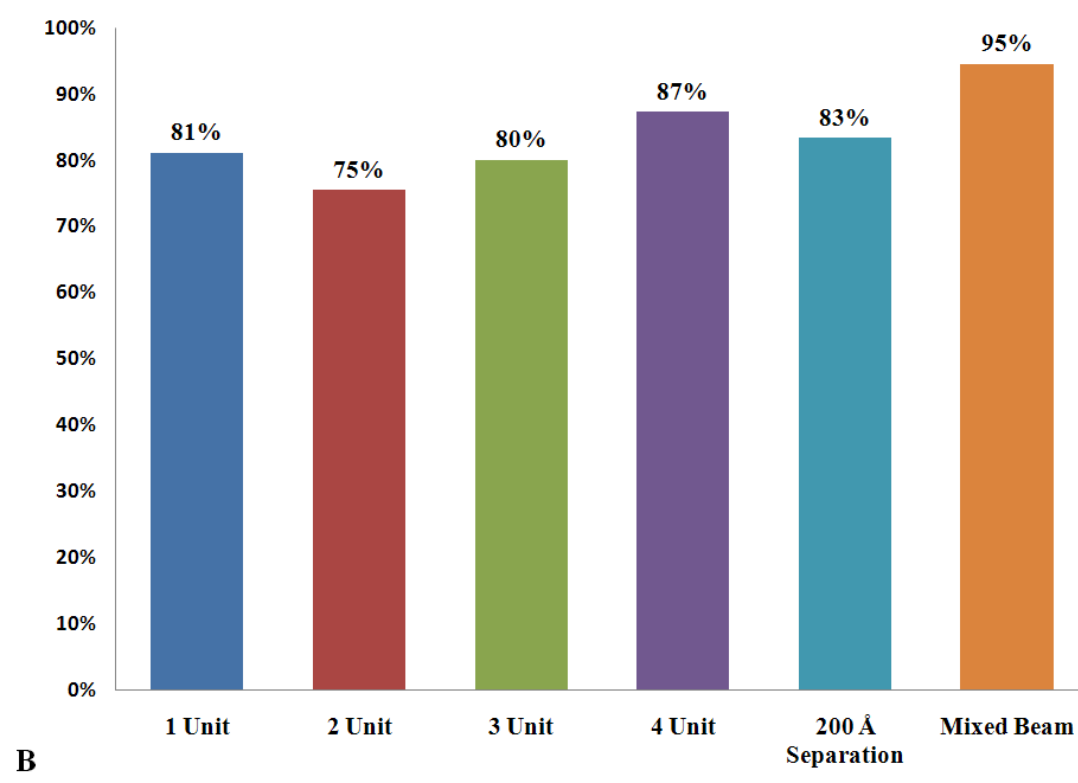
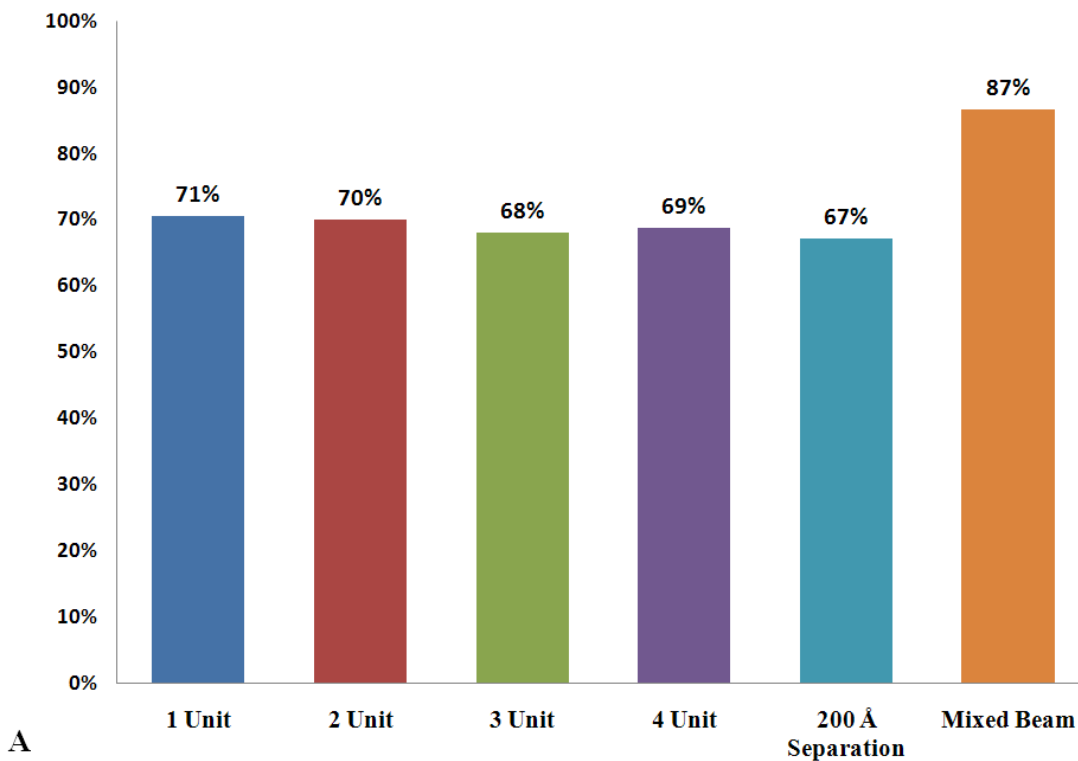


Figure 5-7 Percentages of metal atoms in the first two deposited layers on TiO<sub>2</sub>-terminated STO. A) Sr atoms in first layer, B) Ti atoms in second layer.

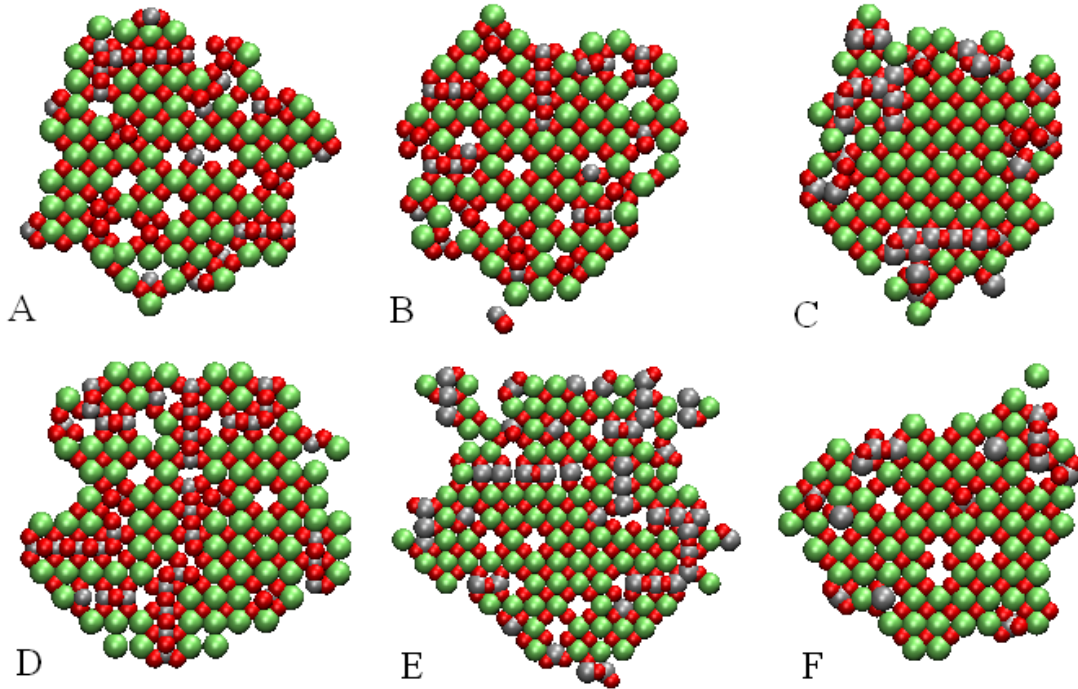


Figure 5-8 First layer of each film deposited on  $\text{TiO}_2$  termination illustrating the 4-fold site vacancies,  $\text{TiO}_2$  inclusions and Ti substitutions. A) 1-Unit STO, B) 2-Unit STO, C) 3-Unit STO, D) 4-Unit STO, E) 3-Unit STO with 200 Å separation, F) Mixed-size distribution beam with SrO and  $\text{TiO}_2$  particles.

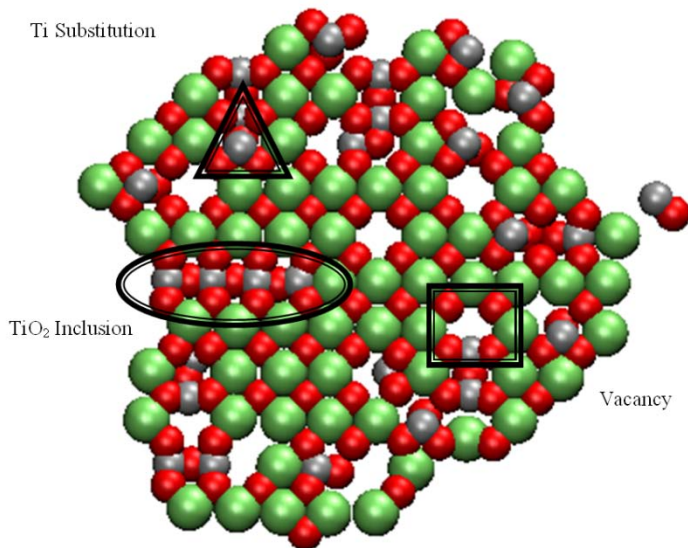


Figure 5-9 Defects present in deposited films on  $\text{TiO}_2$  termination. Triangle: Ti substitution. Oval:  $\text{TiO}_2$  inclusions. Square: 4-fold vacancy.

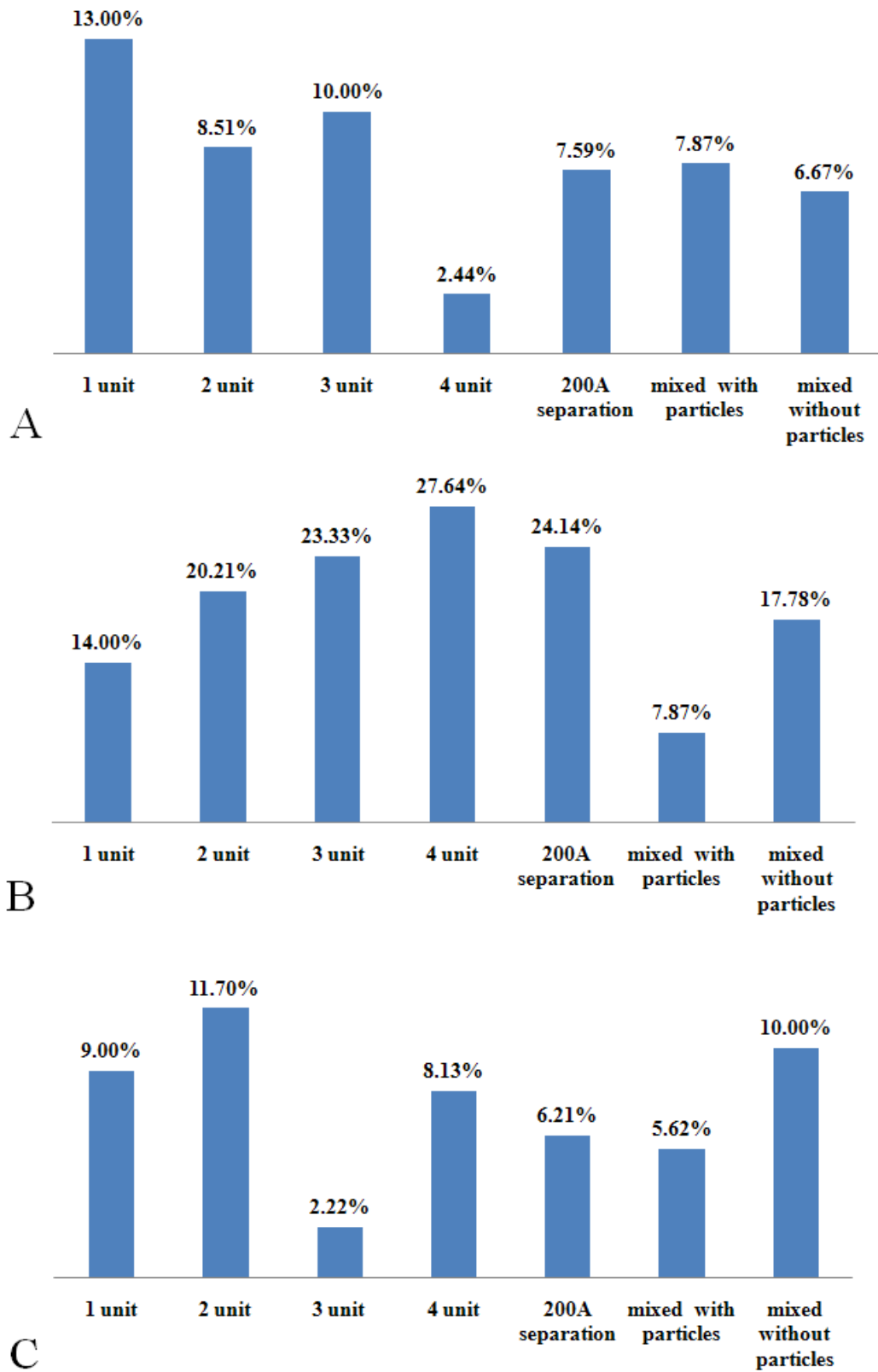


Figure 5-10 Defect percentages. A) Ti substitution. B) 4-fold site vacancy. C) TiO<sub>2</sub> inclusions.

## Discussion

Films deposited on SrO-terminated STO for all schemes investigated yield a partially ordered first layer with very little structural order within the second layer and no dependence on cluster size distribution or deposition rate is predicted. The overall film structure on the TiO<sub>2</sub> termination is described as having regions of order similar to that in bulk STO with three structural defects: Ti substitution for Sr, TiO<sub>2</sub> inclusions, and 4-fold site vacancies. The first deposited layer on both terminations has a structural order comparable to bulk STO, as indicated in the percentage of metal atoms within the layer and the PDFs. STO films deposited on TiO<sub>2</sub>-terminated STO, however, illustrate two ordered (or semi-ordered) layers before its structural order deteriorates making the layers fully disordered, whereas films deposited on SrO-terminated STO only retains structural order in the first deposited layer. The PDFs also indicate films deposited on SrO termination only correspond to the bulk nearest neighbor distances up to the second nearest neighbor whereas the PDFs for the films deposited on TiO<sub>2</sub> termination exhibit longer-ranged order.

Comparing the metal atom percentages with respect to termination indicates films deposited on the TiO<sub>2</sub> termination have an overall higher percentage of expected metal atoms within each layer compared to films deposited on SrO-terminated STO. The impact of deposition scheme on layer composition was not conclusive since the differences are within the statistical variance between repeated simulations. The PDFs comparing mono- and mixed-beam deposition shows the same peak position and width, which also indicates that the differing schemes have minimal effect on the deposited film structure. Looking at the defects observed within the first deposited layer, Ti substitution is the most prevalent defect for the 1-unit STO beam and TiO<sub>2</sub> inclusions dominate with 4-unit STO beam. Also looking at the defect percentages, it appears TiO<sub>2</sub> inclusions increase with increasing cluster size but there is no apparent trend for the

occurrence of Ti substitutions. Four-fold site vacancies are also an indication of the planar density of the deposited films. The cluster size and deposition rate within the ranges studied illustrate no apparent influence on vacancies but the mixed-beam deposition including SrO/TiO<sub>2</sub> particles, contains fewer vacancies compared to the mixed-beam deposition without these particles.

### **Conclusions**

Analyzing the effects of incident particle size was accomplished by differing-sized stoichiometric cluster deposition. To determine the effect of cluster size distribution within the beam, films were also grown by depositing beams comprised of 1 to 4-unit STO clusters with and without SrO and TiO<sub>2</sub> particles. It is apparent that TiO<sub>2</sub>-terminated STO yields films with ordered first and second layers while the SrO-termination only has an ordered first deposited layer. Defects in the first layer deposited on TiO<sub>2</sub> termination showed a slight dependence on deposition scheme with the mixed-sized beam including SrO/TiO<sub>2</sub> particles having the lower overall defects present when compared to both mixed-size beams without SrO/TiO<sub>2</sub> and mono-sized beams.

Analysis of the deposited films reveals that cluster size and deposition rate within the studied ranges does not affect the structure of the deposited film. Termination effect is shown to impact the resulting film structure as was seen in the previous deposition studies where films deposited on TiO<sub>2</sub>-terminated STO exhibit a more highly ordered film as compared to SrO-terminated STO.

## CHAPTER 6 TEMPERATURE ACCELERATED DYNAMICS

Due to the time-scale limitations of MD simulations and the time-scale needed for deposited films to relax, temperature accelerated dynamics (TAD) has been employed to further the relaxation time of deposited thin films. Surface adatom and ad-dimer diffusion mechanisms are also investigated. This work was carried out in collaboration with Blas P. Uberuaga and Arthur F. Voter of Los Alamos National Laboratory.

### Simulation Set-up

As with all of our studies, the Buckingham potential with parameterization from Sekiguchi *et al.*<sup>105</sup> was used to describe the short-range interactions. As discussed in Chapter 2, TAD performs basin constrained MD at a high temperature,  $T_{\text{high}}$ , and records the time at which a transition occurs,  $t_{\text{high}}$ . The  $t_{\text{high}}$  is then interpolated to a corresponding waiting time,  $t_{\text{low}}$ , at  $T_{\text{low}}$  (the temperature of interest) based on Equation 2-11. The transition with the lowest  $t_{\text{low}}$  is accepted after continuing the MD until  $t_{\text{high,stop}}$ , Equation 2-12 is reached. As discussed,  $t_{\text{high,stop}}$  depends on two factors, a minimum pre-exponential factor and an uncertainty,  $\delta$ , where the probability that a transition would occur with a shorter  $t_{\text{low}}$  is less than  $\delta$ . For each system the uncertainty  $\delta$  was 0.05 and the minimum prefactor was chosen to be  $10^{-12}$ . For a sample system, the normal mode frequencies were calculated to obtain the vineyard prefactor for each transition and it was shown to be  $10^{-13}$ . This implies our simulations were a bit less conservative but still adequate since the same events and barriers were predicted with both prefactor values. This means, with a certainty of 95%, continuing the high-temperature MD would not produce a transition which would extrapolate to a shorter, low-temperature, waiting time. The low temperature for most simulations was 1000 K which was the temperature of interest and the high temperature was varied depending on the system under consideration.

Unlike the MD studies discussed in the previous chapters, TAD has system size restrictions due to the complexity and serial nature of the code. Therefore, to extend the time-scale of the relaxation of deposited films, partially deposited films consisting of 2 ML coverage on a smaller surface area is extracted from the MD simulation results, as illustrated in Figure 6-1. This system was chosen due to its simplicity, one ML of SrO was already relaxed with an island of TiO<sub>2</sub> (1ML equivalent) above. To further increase the efficiency of the simulations, only the four layers below the film were allowed to relax during the simulations, while the remaining five layers were held fixed. For this system the high temperature was 3000 K.

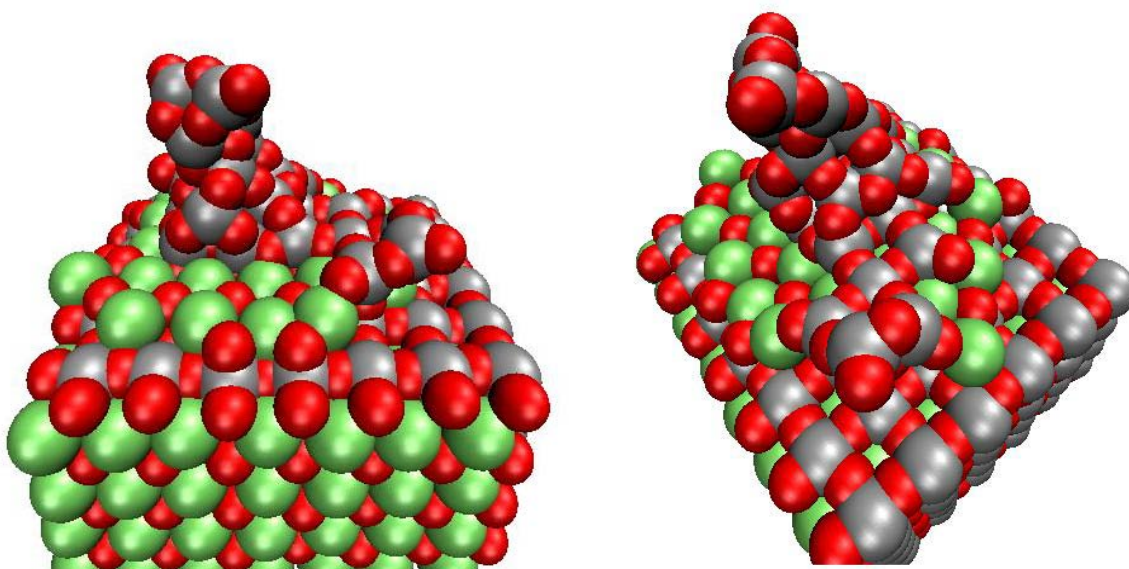


Figure 6-1 Initial 2ML deposited on TiO<sub>2</sub>-terminated STO structure

To determine the mechanisms involved in adatom and ad-dimer surface diffusion, one SrO/Sr/TiO<sub>2</sub>/Ti/TiO/O particle or atom was placed above each STO (001) termination on varying adsorption sites, indicated in Figure 6-2. The high temperature for each simulation depended on the temperature at which transition events were observed. The high temperature for the diffusion of O and SrO was 2400 K and for the Ti containing species a high temperature of 2900 K was

used. The star is noted as a bridge site (Br), triangle is a 4-fold site, and  $T_x$  indicates an adsorption site above x atom. This notation will be utilized throughout the following sections. Multiple adsorption sites were evaluated as the starting position and had no effect on the diffusion barriers and mechanisms observed since each possible adsorption site was also either a minimum or transition state found in the TAD simulations.

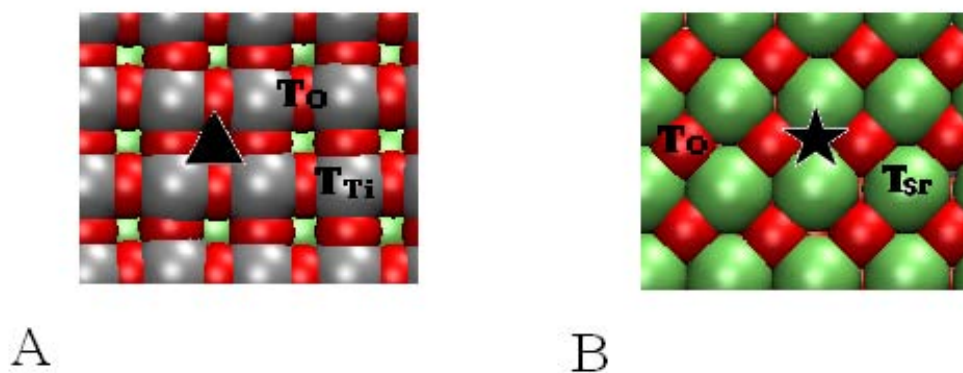


Figure 6-2 Adsorption sites. A)  $\text{TiO}_2$  termination B) SrO Termination

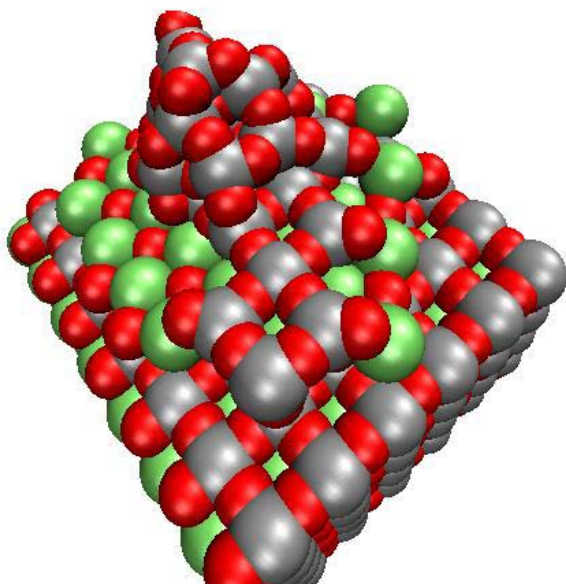


Figure 6-3 Final 2ML relaxed structure.

## Results

Initially, we expected TAD to relax the  $\text{TiO}_2$  island (equivalent to 1ML) above the 1ML SrO, deposited with traditional MD, to a structure similar to bulk STO by overcoming the kinetic limitations of our classical MD simulations. However, increasing the time-scale of the relaxation process proved to be less revolutionary than expected. Due to small barriers associated with many transitions taking place within the film, on the order of a few meV, TAD would become less efficient due to the higher probability of reverse transitions (where state B reverts back to state A). Additional TAD features were utilized that reduces such back and forth from occurring but the system has an overabundance of such small barriers and therefore slows down the simulation. The resulting film is shown in Figure 6-3. The figure indicates that  $\text{TiO}_2$  units comprising the  $\text{TiO}_2$  island atop the SrO deposited layer are beginning to form a  $\text{TiO}_2$  layer and the island has smoothed out such that the height is reduced by approximately 5 Å.

O adatom diffusion proved to be more interesting. The minimum state predicted for both terminations is atop a surface cation,  $\text{T}_{\text{Ti}}$  or  $\text{T}_{\text{Sr}}$ . On the SrO termination, O diffusion occurred through a hopping mechanism while on the  $\text{TiO}_2$  termination, the diffusion mechanism was an exchange of the ad-oxygen with a surface oxygen; the latter mechanism is depicted in Figure 6-4. The O exchange begins by pulling an O from the surface and moving to an intermediate state where both pulled-O and ad-oxygen sit on adjacent  $\text{T}_{\text{Ti}}$  (image 3 in Figure 6-4). The ad-oxygen then moves into the vacancy created by pulling out the surface O and the pulled-O is now the diffusing adatom (image 5). The barrier associated with pulling out a surface O (images 1 to 3) is 1.41 eV while the barrier to put the original ad-oxygen into the vacancy (images 3 to 5) is 0.18 eV, where images 2 and 4 are saddle configurations. In addition to a complete exchange, where translation occurs the surface oxygen pulled out was also put back in its original position with a coinciding barrier of 0.116 eV.

It is important to note that TAD records the transitions which are not accepted (they were not the transitions with the lowest  $T_{low}$  waiting time). In some of these cases, an additional hopping mechanism was attempted where the O adatom moves from  $T_{Ti}$  to an adjacent  $T_O$ , to another  $T_{Ti}$ ; this transition has a barrier of 2.4 eV, or 1 eV higher than the barrier associated with the exchange mechanism.

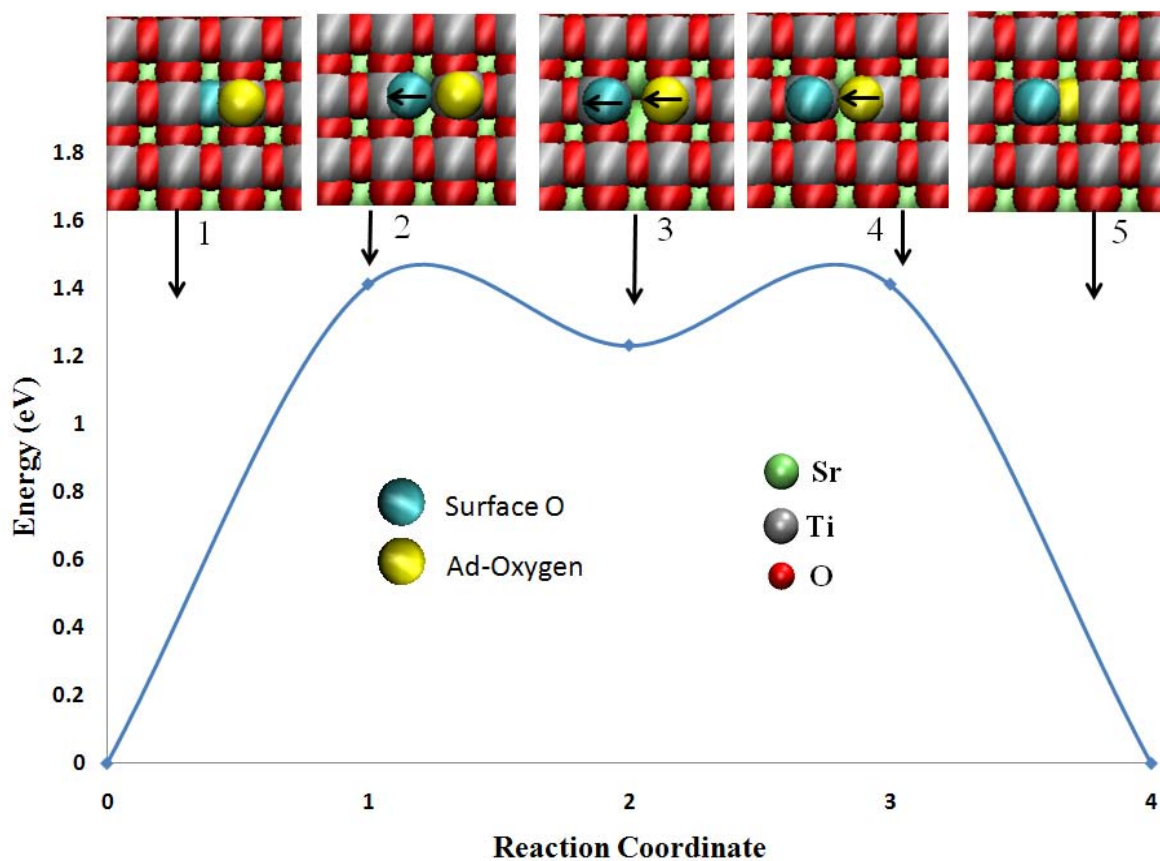


Figure 6-4 Oxygen adatom exchange mechanism on  $TiO_2$ -terminated STO.

The hopping mechanism of the O adatom upon SrO termination is illustrated in Figure 6-5. This mechanism involves the O adatom hopping from  $T_{Sr}$  across a bridge site, Br, to an adjacent  $T_{Sr}$ . The energy barrier associated with the ad-oxygen going from  $T_{Sr}$  to Br (images 1 to 3 in Figure 6-5) is 0.19 eV and, completing the translation, from the Br to an adjacent  $T_{Sr}$  (images 3 to 5), is 0.06 eV where images 2 and 4 are saddle configurations.

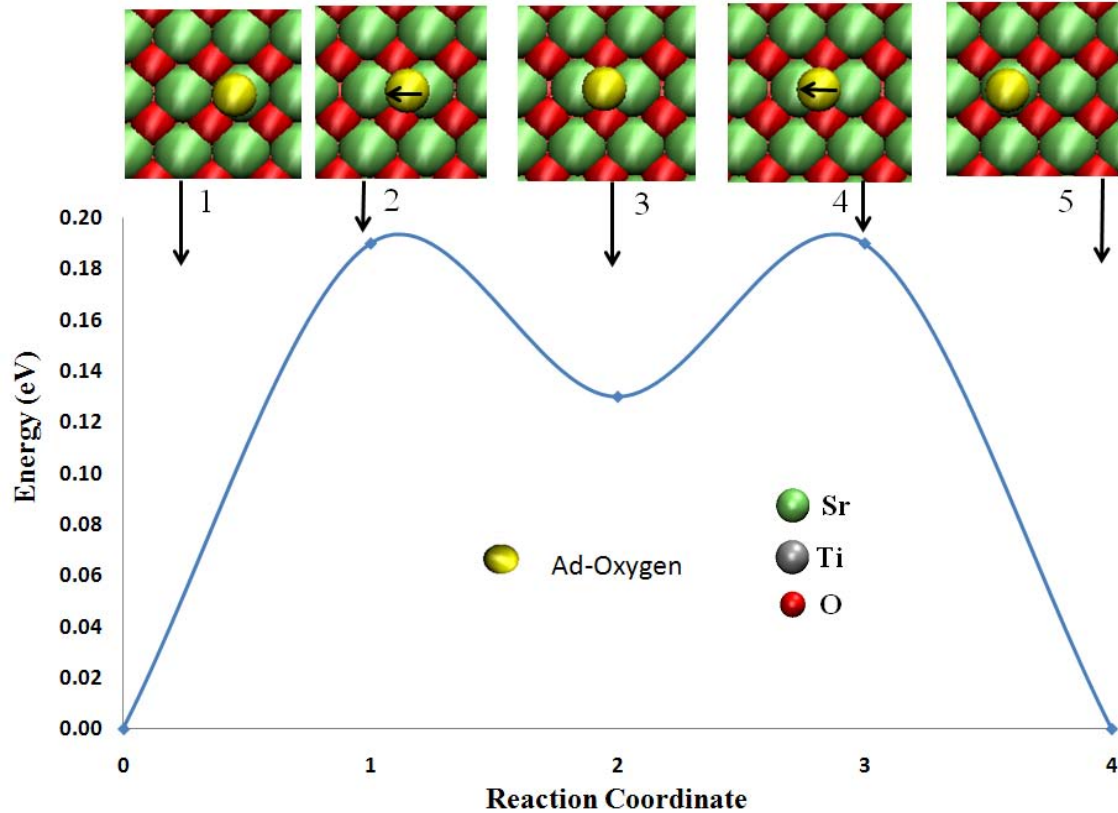


Figure 6-5 Oxygen adatom hop mechanism on SrO-terminated STO.

SrO ad-dimer diffusion also exhibited varying mechanisms between the two STO terminations. SrO atop the  $\text{TiO}_2$  termination diffused via an oxygen exchange mechanism similar to that observed in the O/ $\text{TiO}_2$ -terminated system, illustrated in Figure 6-6. In the minimum energy configuration for SrO atop  $\text{TiO}_2$  termination, the Sr sits at the four-fold site while the O in the dimer rests at  $T_{\text{Ti}}$  (Figure 6-6, image 1). SrO diffusion begins by pulling out a surface O (images 1 to 3) then moving to an intermediate state where both surface O and dimer O sit at adjacent  $T_{\text{Ti}}$  (image 3). The original O associated with the ad-dimer is then placed into the vacancy created and the Sr moves to an adjacent four-fold site (images 3 to 5), making the removed surface O now part of the diffusing dimer. The barrier associated with taking surface oxygen is 1.18 eV and to place the original ad-oxygen in the vacancy from the surface oxygen is 0.18 eV thereby completing the SrO translation.

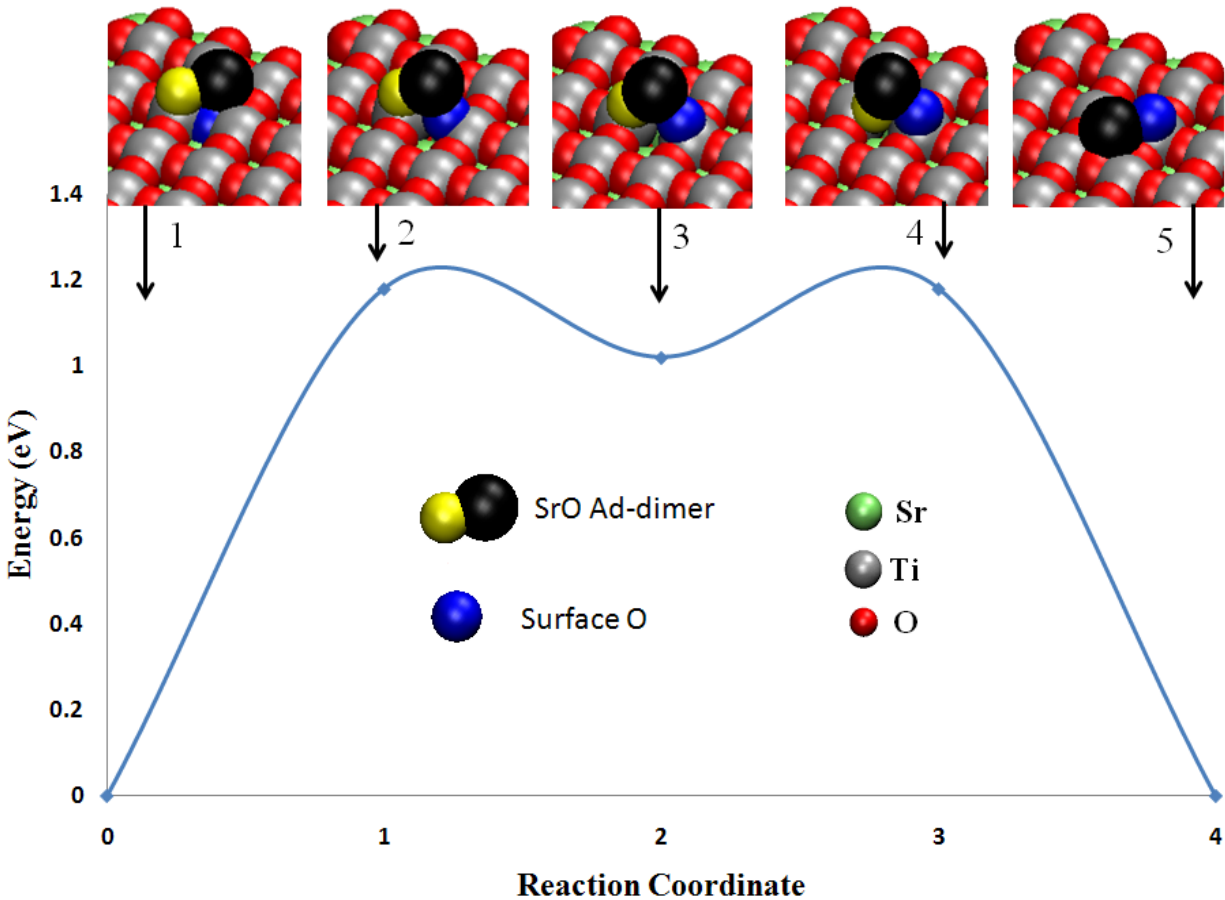


Figure 6-6 SrO diffusion mechanism on  $\text{TiO}_2$ -terminated STO A) initial structure, B) exchange and C) final structure.

The minimum energy configuration of the SrO ad-dimer atop the SrO termination consists of Sr on  $\text{T}_{\text{O}}$  and O on  $\text{T}_{\text{Sr}}$ , which is illustrated as image 1 in Figure 6-7. The ad-dimer diffused atop the surface by a “walking” mechanism, which is simply a combination of two consecutive hops, one by each member of the dimer. The Sr hop (Figure 6-7, A) involves moving the Sr from  $\text{T}_{\text{O}}$  to a Br site (images 1 to 3) having an associated barrier of 0.24 eV then to an adjacent  $\text{T}_{\text{O}}$  (3 to 5) after overcoming a barrier of 0.22 eV. The O hop (Figure 6-7, B) begins by moving from  $\text{T}_{\text{Sr}}$  to a Br site (images 6-8) then back to an adjacent  $\text{T}_{\text{Sr}}$  (images 8 to 10) with a barrier of 0.24 eV. This completes the full translation.

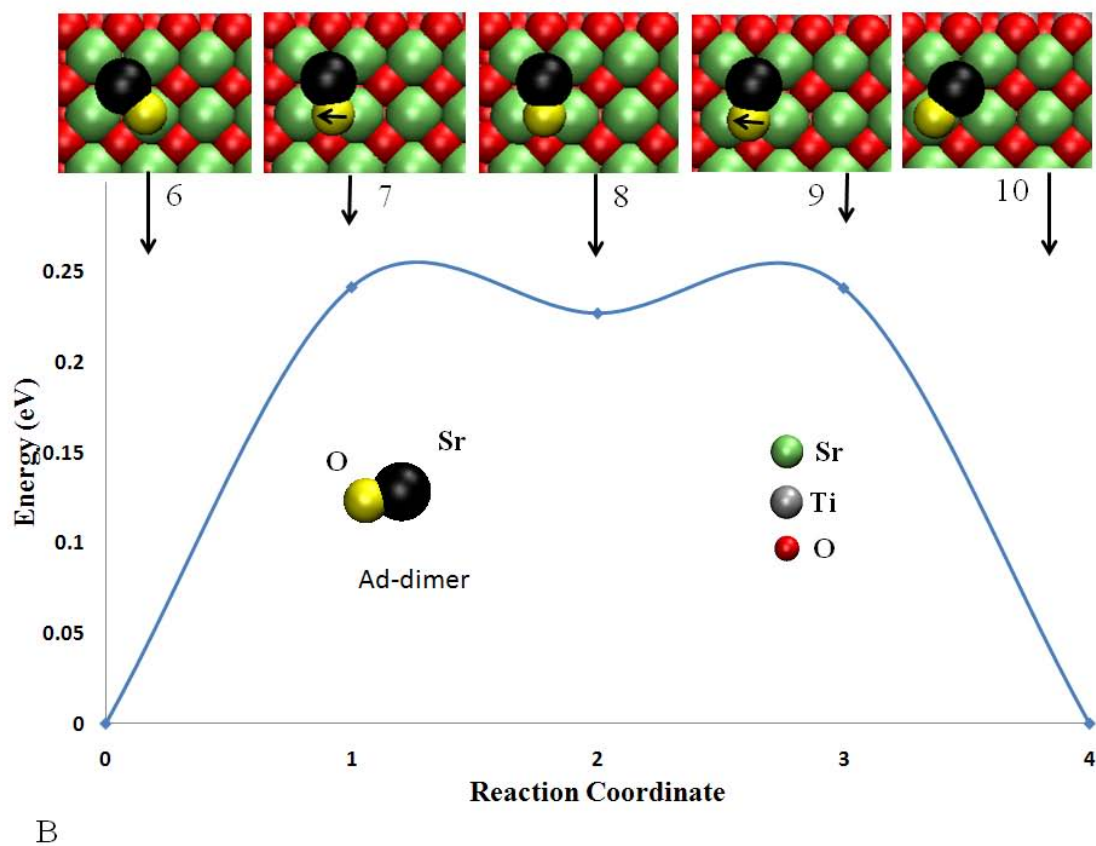
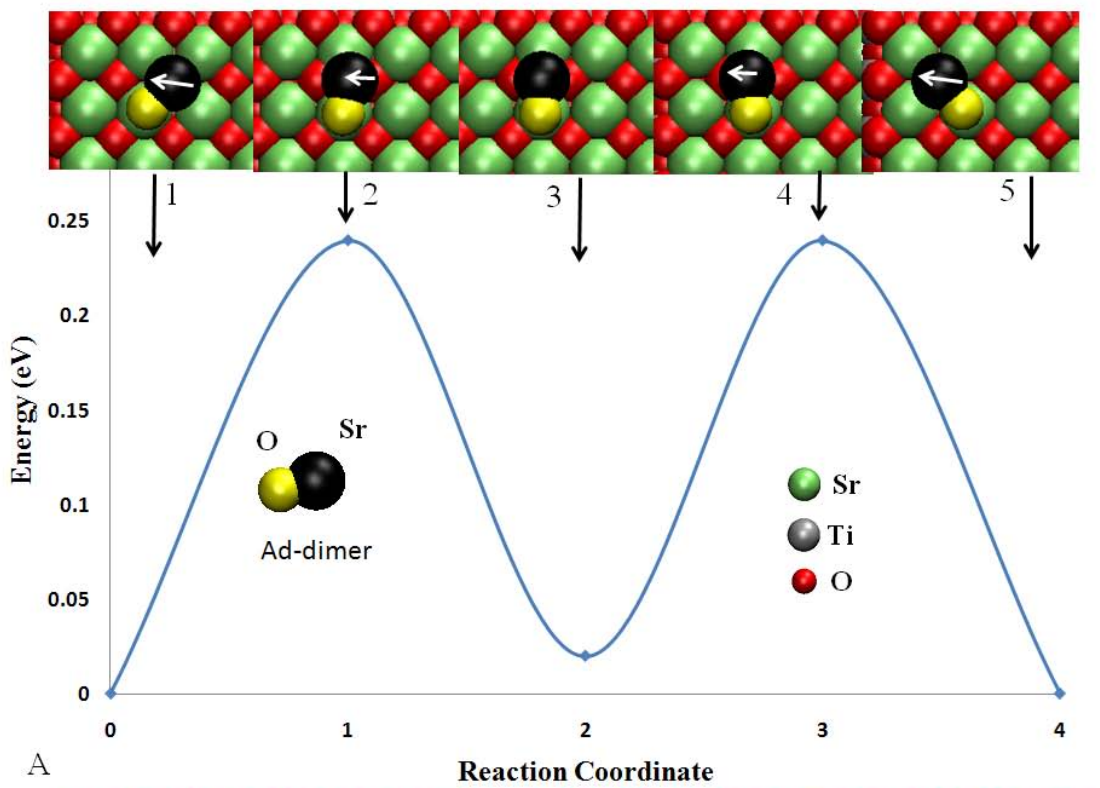


Figure 6-7 SrO ad-dimer surface diffusion on SrO termination. A) Sr hop, B) O hop.

Ti-containing adsorbates were also examined, including Ti, TiO and TiO<sub>2</sub>. However, compared to the other ad-species considered, adsorbates containing Ti did not exhibit any translation. The Ti adatom bonded with four surface oxygen atoms making it four coordinated as in bulk TiO<sub>2</sub>. This was also predicted for TiO and TiO<sub>2</sub> ad-particles, where they bonded with three and two surface oxygen atoms, respectively. The preferred structure is shown in Figure 6-8 where the yellow oxygen atoms are bonded to the adsorbed Ti. It is believed that the additional bonding with the surface leads to the immobility of the Ti-containing ad-species.

### Discussion

The relaxation of the 2 ML film produced using the classical MD simulations discussed in Chapter 4 did not vary appreciably in the TAD simulations. Rather than transforming to bulk-like STO structures, the deposited structures only exhibited the beginning signs of TiO<sub>2</sub> ordering above the SrO deposited layer and some smoothing of TiO<sub>2</sub> islands. The TAD simulations do provide tremendous insight into the mechanisms by which individual deposited particles diffuse on STO surfaces.

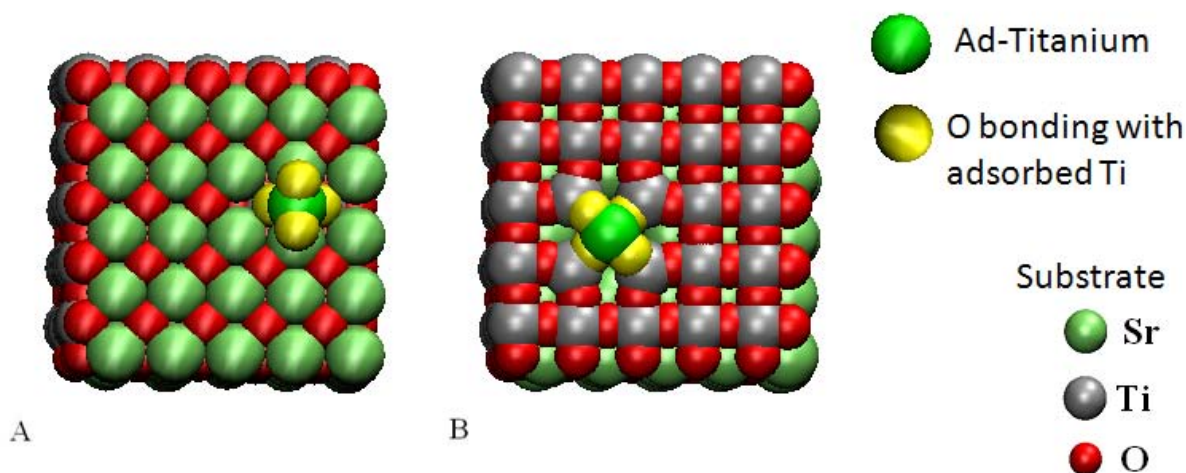


Figure 6-8 Structure formed when Ti, TiO or TiO<sub>2</sub> is adsorbed, surface O bonds with Ti to make Ti 4 coordinated.

Surface diffusion was seen to produce differing mechanisms depending on the termination of the (100) STO surface. Similar to the literature on metal adatoms on MgO(001)<sup>138, 139</sup> and NiO(001)<sup>140</sup>, Sr and Ti sit on T<sub>O</sub> sites in the minimum energy configurations when adsorbed on SrO-terminated STO. On TiO<sub>2</sub> termination, however, the cations prefer the four-fold sites to maximize the distance between the adsorbed cation and surface Ti. Adsorbates on the SrO termination exhibited a hopping mechanism also seen for Au surface self-diffusion along terraces.<sup>141</sup> This is also comparable to Henkelman et al.'s work on MgO ad-dimer diffusion on MgO (001).<sup>142</sup> In their study, the Mg from the ad-dimer exhibits a hop similar our Sr hop in Figure 6-7 A and they also describe a O hop similar to Figure 6-7 B. The advantages of TAD are exploited in this study. The first part of their study involved static calculations minimizing initial, final and intermediate structures. From this standpoint, the collaborative cation and O hop we describe as walking was not verified. However, the second part of the study involved using TAD to describe the MgO ad-dimer diffusion and predicted the same walk outlined in the previous section for the SrO ad-dimer.

The adatoms or ad-particles on TiO<sub>2</sub>-terminated STO diffused via an oxygen exchange mechanism. The presence of an exchange (or replacement) mechanism was first discovered theoretically in 1990 by Feibelman for Al diffusion on Al (001)<sup>81</sup> and experimentally by Kellogg and Feibelman also in 1990 in the surface self-diffusion on Pt (001).<sup>143</sup> The exchange mechanism has an overall higher barrier when compared to the hopping mechanism on SrO termination. This coincides with earlier mobility analysis that showed particulate mobility is higher on the SrO termination seen using traditional MD.<sup>122</sup>

The behavior of Ti containing species can be compared to a theoretical study of Ni<sup>3+</sup> on NiO due to the difference in oxidation state of the adatom with the surface cation. In this case, as

with our study,  $\text{Ni}^{3+}$  pulls oxygen atoms from the surface and, compared to a  $\text{Ni}^{2+}$  adatom on NiO, has a stronger interaction with the surface.<sup>144</sup> The difference in diffusion mechanisms between the two terminations is believed to be due to the difference in atomic density of the two planes. The  $\text{TiO}_2$  terminated surface is more closely packed and contains twice the oxygen present on the SrO termination; therefore instead of O hopping along the surface (and getting nearer to surface O) it forces the surface O to vacate its lattice site to be replaced by the original O. This process is predicted to occur for both SrO and O diffusion. Evidence of this is demonstrated in the attempted O hop on  $\text{TiO}_2$ -terminated STO ( $\text{T}_{\text{Ti}} \rightarrow \text{T}_{\text{O}} \rightarrow \text{T}_{\text{Ti}}$ ) exhibiting a significant energy barrier when compared to the exchange process (1 eV difference).

### Conclusions

Utilizing TAD to extend the relaxation time-scale for the 2ML STO film (1ML SrO and 1 ML  $\text{TiO}_2$ ) produced some smoothing of the  $\text{TiO}_2$  island but, due to the abundance of back-and-forth transitions, the simulation was not able to overcome the kinetic limitations of our traditional MD simulations. O and SrO are predicted to diffuse via exchange on  $\text{TiO}_2$ -terminated STO and via a hopping mechanism on SrO-terminated STO. Overall, ad-species have a lower barrier to diffusion on SrO-terminated (100) STO allowing particles a higher mobility on this surface.

The barriers calculated in this work can be utilized to parameterize the kMC simulations discussed in Chapter 1. These results also complement the classical MD simulations discussed in Chapters 3 through 5 to elucidate the atomistic mechanisms occurring after an initial deposition event. These findings are comparable to the study of SrO and  $\text{TiO}_2$  particulate mobility on each termination discussed in Chapter 3 where it was shown that SrO particles are more mobile overall and that mobility was higher on SrO termination compared to  $\text{TiO}_2$  termination.

An additional benefit of TAD is the ability to capture saddle configurations and possible complex diffusion mechanism since, while a transition from one state to another is infrequent, the actual passing is quite fast and what as appears to be a simple hop in MD could actual be a more complicated “walk”. TAD enables the calculation of energy barriers as well as intermediate and saddle geometries.

In future studies of thin-film deposition it is recommended that classical MD be utilized to deposit a single incident species while TAD be used to describe the relaxation occurring between events. This approach is predicted to make use of the strengths of each approach to most accurately describe the dynamics and relaxation of deposited particles.

## CHAPTER 7 GENERAL CONCLUSIONS

In this dissertation, MD simulations were performed to study the deposition and growth of metal-oxide thin films on STO (100) at the atomistic level. The results obtained for each system were compared to experimental results and elucidate the processes involved in the first stages of deposition.

The first section investigates SrO and TiO<sub>2</sub> thin film growth to gain a fundamental understanding of the different growth modes exhibited by each. These films exhibited significantly different morphologies and proceeded in two different growth modes. While SrO thin films grew in a layer-by-layer fashion and have smooth highly ordered structure, TiO<sub>2</sub> thin films grew in a three-dimensional growth mode producing an island/agglomerate morphology. TiO<sub>2</sub> films in this study are consistent with experimental results for films grown at high deposition rates. Mobility data, work of adhesion results, and particle interaction energies explain the causes of the differing growth modes exhibited in SrO and TiO<sub>2</sub> deposition.

Next, STO thin films were grown using two deposition methods, alternating TiO<sub>2</sub>/SrO particles in an ABAB arrangement, and alternating TiO<sub>2</sub>/SrO monolayers. Alternating monolayer deposition on TiO<sub>2</sub>-terminated STO produced superior films based on the structural analysis performed. As outlined in SrO/TiO<sub>2</sub> thin film deposition, SrO particles exhibit higher mobility and can grow in a layer by layer fashion. Therefore, since the first deposited layer is SrO, it has the higher structural quality. Additionally, subsequent layers deposited in this scheme produce a higher quality film due to the superior quality of the first layer.

While the previous study is more analogous to MBE due to the size of the incident particles, PLD involves species of larger sizes. To better simulate species produced during PLD, stoichiometric STO clusters of varying sizes were created. These clusters were equilibrated in

vacuum and as a result relaxed into structures having little to no bulk-like structural properties. While no particle size dependence was found, substrate termination yet again impacted the resulting thin film. Films deposited on TiO<sub>2</sub>-terminated STO produced the longer ranged ordered films compared to films deposited on SrO-terminated STO; this result was also observed in AMD. Defects present in the first deposited layer on TiO<sub>2</sub>-termination were also analyzed. Three main defects were seen: TiO<sub>2</sub> inclusions, Ti substitution and Sr vacancies. Modifying the incident particle-size distribution resulted in a reduction of the overall occurrence of defects within the first layer.

TAD results on the adatom and ad-dimer surface diffusion revealed the mechanisms involved following each deposition event. As with our thin film deposition studies using classical MD, termination had an important impact on the diffusion mechanisms. Ad-species on SrO termination move along the surface by hopping. SrO diffusion occurs with consecutive hops by each atom in the dimer. On the TiO<sub>2</sub> termination, however, diffusion progresses by oxygen exchange with a higher overall diffusion barrier compared to the hopping observed on SrO termination.

In summary, this is the first study to deposit relaxed STO clusters and investigate surface diffusion on perovskite substrates. In addition to investigating thin film growth, analysis codes were developed to analyze the resulting films, these are included in Appendix A.

In future work to model thin-film growth, the mechanisms and diffusion barriers calculated here can be used to parameterize kMC simulations. Also, a hybrid approach is recommended for the simulation of thin-film growth, combining a classical MD description of the initial deposition event and utilizing TAD to simulate the subsequent relaxation between events.

## APPENDIX ANALYSIS CODES

### Planar pair distribution (Sr-O given as example)

```

c*****
c   Last modified 7/19/08 Jennifer Wohlwend
c   Program to generate the pair distribution function
c   for Strontium-Oxygen for deposited species.
c   PDF is for atom i within layer of upper limit ul
c   and lower limit ll with neighboring j in 3D
c   Language: Fortran
c*****

      implicit real (a-h,o-z)
      parameter (max=50000)

      real::x(max),y(max),z(max),ll,lu
      integer::natoms,counting(3000000),tnrtot,kt(max)
      integer::igo(max),ithermo(max),No,Nti,Nsr
      real::th(3,3),binw,rbd,rx1,ry1,rz1,ro,dvr2,dvr1
      integer::tbin,nn

      open(unit=18,file='SrO_pdf.xls',status='unknown')   !output
      open(unit=35,file='structure_in', status='unknown') !input
      No=0
      Nti=0
      Nsr=0

      ll=63.6   !lower limit of i layer (A)
      ul=66.0   !upper limit of i layer (A)

      read(35,*) natom
      do 5 i=1,natom
        read(35,*) k,kt(k), x(k), y(k), z(k),igo(k), ithermo(k)
          if ((x(k).gt.ll).and.(x(k).lt.ul)) then
            if (kt(k).eq.8) No=No+1
            if (kt(k).eq.22) Nti=Nti+1
            if (kt(k).eq.38) Nsr=Nsr+1
          endif
5      continue

      tnrtot=natom
      binw=0.01
      rbd=7
      tbin=rbd/binw
      nn=0
      do k=1,tbin
        counting(k)=0
      enddo
      do i=1,tnrtot
        if (kt(i).eq.38) then      !sr
          if ((x(i).gt.ll).and.(x(i).lt.ul)) then
            nn=nn+1
          do j=1,tnrtot

```

```

        if (i.ne.j) then
          if (kt(j).eq.8) then !OXYGEN
          if (ithermo(j).eq.0) then
            rx1=x(j)-x(i)
            ry1=y(j)-y(i)
            rz1=z(j)-z(i)
c*****periodic boundary conditions if analyzing bulk
c          if (rx1.gt.(th(1,1)/2)) rx1=rx1-th(1,1)
c          if (rx1.lt.(-th(1,1)/2)) rx1=rx1+th(1,1)
c          if (ry1.gt.(th(2,2)/2)) ry1=ry1-th(2,2)
c          if (ry1.lt.(-th(2,2)/2)) ry1=ry1+th(2,2)
c          if (rz1.gt.(th(3,3)/2)) rz1=rz1-th(3,3)
c          if (rz1.lt.(-th(3,3)/2)) rz1=rz1+th(3,3)
c*****
          r3=((rx1*rx1)+(ry1*ry1)+(rz1*rz1))
          r2=sqrt(r3)

          do k=1,tbin
            if (((k-1)*binw.Lt.r2).and.(r2.LE.(k*binw)))then
              counting(k)=counting(k)+1
            endif
          enddo
        endif
      endif
    enddo
  endif
endif
write(18,*) Nsr,nn
do k=1,tbin
  write(18,*)(k*0.01),float(counting(k))/Nsr
enddo

stop
end program

```

## Coordination Analysis

```

c*****
c   Last modified 3/12/09 Jennifer Wohlwend
c   Program to calculate the coordination of O, Sr, and Ti atoms
c   coordination is planar, i is within each layer j is 3D
c   Language: Fortran
c*****
   parameter (max=40000)
   parameter (max2=40000)
   parameter (max4=6)

   implicit real*8 (a-h)
   real      x(max),y(max),z(max)
   integer   iOTi(max),nOTi(max4),iOSr(max),nOSr(max4),nCNOTi8(max4),
1  nCNOTi7(max4),nCNOTi6(max4),nCNOTi5(max4),nCNOTi4(max4),
1  nCNOTi3(max4),nCNOTi2(max4),nCNOTi1(max4),nCNOTi0(max4),
1  nCNOSr14(max4),nCNOSr13(max4),nCNOSr12(max4),nCNOSr11(max4),
1  nCNOSr10(max4),nCNOSr9(max4),nCNOSr8(max4),nCNOSr7(max4),
1  nCNOSr6(max4),nCNOSr5(max4),nCNOSr4(max4),nCNOSr3(max4),
1  nCNOSr2(max4),nCNOSr1(max4),nCNOSr0(max4)
   real      blat,diagonal,dx,dy,dz
   integer   kt(max),natom,nframe,ithermo(max),igo(max),nl,
1  iSrO(max),iTio(max),nSrO(max4),nTiO(max4),p
   integer   ncellx,ncelly,ncellz,maxdist,No,Nti,Nsr
   integer   nCNTi6(max4),nCNTi8(max4),nCNTi7(max4),
1  nCNTi5(max4),nCNTi4(max4),nCNTi3(max4),nCNTi2(max4),
1  nCNTi1(max4),nCNTi0(max4),layer(max)
   integer   nCNSr12(max4),nCNSr11(max4),nCNSr10(max4),
1  nCNSr9(max4),nCNSr8(max4),nCNSr7(max4),nCNSr6(max4),
1  nCNSr5(max4),nCNSr4(max4),nCNSr3(max4),nCNSr2(max4),
1  nCNSr1(max4),nCNSr13(max4),nCNSr14(max4),nCNSr0(max4)
   real      dist,temp
   integer   count,lay,CNOTI(max),CNOSR(max),CNSRO(max),
1  CNTIO(max),osr,oti,sro,tio
   integer   Nolayer6,Nsrlayer6,Ntilayer6
   integer   Nolayer1,Nsrlayer1,Ntilayer1
   integer   Nolayer2,Nsrlayer2,Ntilayer2
   integer   Nolayer3,Nsrlayer3,Ntilayer3
   integer   Nolayer4,Nsrlayer4,Ntilayer4
   integer   Nolayer5,Nsrlayer5,Ntilayer5

   open (unit=11, file='structure_in', status='old')
   open (unit=6, file='output1', status='unknown')   !verbose
   open (unit=7, file='outputlist',status='unknown') !short
   open (unit=10, file='pos_CN_layer',status='unknown') !surface atomic positions with corresponding
coordination numb
      write (10,*) ' i ',' kt ',' x ',' y ',' z ',
1  ' OTi ',' OSr ',' TiO ',' SrO '
   No=0
   Nti=0
   Nsr=0
   layer1=0
   layer2=0
   layer3=0

```

```

        layer4=0
        layer5=0
        layer6=0
c*****
c reads the input file
c*****
read(11,*) natom
do 10 i=1,na
  read(11,*) k,kt(k), x(k), y(k), z(k), igo(k),ithermo(k)
  igo(k)=6
  if (imass(k).eq.3) kt(k)=8
  if (imass(k).eq.2) kt(k)=22
  if (imass(k).eq.1) kt(k)=38
c*****Input layer parameters, coordination is found for each deposited layer
  if(x(k)*blat.ge.68.2) igo(k)=0          !top layers
  if((x(k)*blat.ge.62.0).and.(x(k)*blat.lt.64.2)) igo(k)=1  !layer(k)=1
  if((x(k)*blat.ge.64.2).and.(x(k)*blat.lt.66.2)) igo(k)=2  !layer(k)=2
  if((x(k)*blat.ge.66.2).and.(x(k)*blat.lt.68.2)) igo(k)=3  !layer(k)=3
  if((x(k)*blat.lt.60.0).and.(x(k)*blat.gt.58.5)) igo(k)=4  !Sub-surface layer
  if((x(k)*blat.lt.62.0).and.(x(k)*blat.gt.60.0)) then
    if ((y(k)*blat.gt.-15.0).and.(y(k)*blat.lt.20)) then
      if ((z(k)*blat.gt.-20.0).and.(z(k)*blat.lt.19)) igo(k)=5      !layer=surface
  if (kt(k).eq.8) No=No+1
  if (kt(k).eq.22) Nti=Nti+1
  if (kt(k).eq.38) Nsr=Nsr+1
  if ((igo(k).eq.0).AND.(ithermo(k).eq.0)) layer(k)=5  !top
  if ((igo(k).eq.1).AND.(ithermo(k).eq.0)) layer(k)=1  !first layer deposited film
  if ((igo(k).eq.2).AND.(ithermo(k).eq.0)) layer(k)=2  !second layer deposited film
  if ((igo(k).eq.3).AND.(ithermo(k).eq.0)) layer(k)=3  !third layer deposited film
  if ((igo(k).eq.4).AND.(ithermo(k).eq.0)) layer(k)=4  !sub-surface layer
  if ((igo(k).eq.5).AND.(ithermo(k).eq.0)) layer(k)=6  !THIS IS THE SURFACE ATOMS
  if ((igo(k).eq.0).AND.(ithermo(k).eq.0)) layer5=layer5+1
  if ((igo(k).eq.1).AND.(ithermo(k).eq.0)) layer1=layer1+1
  if ((igo(k).eq.2).AND.(ithermo(k).eq.0)) layer2=layer2+1
  if ((igo(k).eq.3).AND.(ithermo(k).eq.0)) layer3=layer3+1
  if ((igo(k).eq.4).AND.(ithermo(k).eq.0)) layer4=layer4+1
  if ((igo(k).eq.5).AND.(ithermo(k).eq.0)) layer6=layer6+1      !TO CHECK THE SURFACE
COORDINATION
  endif
endif
10 Continue
write(6,*)'No=',No,' Nti=',Nti,' Nsr=',Nsr
write(6,*)'Reading is done'
write(6,*)'layer1= ',layer1,' ',layer2= '
1  layer2,' ',layer3= ',layer3,' ',layer4= ',layer4,
1 'layer5= ',layer5
write(7,*)'layer1= ',layer1,' ',layer2= '
1 layer2,' ',layer3= ',layer3,' ',layer4= ',layer4,
1 'layer5= ',layer5
nframe=1
blat=3.9087
ncellx=16
ncellz=ncellx
ncelly=ncellx
c*****
c initializes all the varibales to zero

```

c\*\*\*\*\*

```
do k=1,6
nCNOTi8(k)=0
nCNOTi7(k)=0
nCNOTi6(k)=0
nCNOTi5(k)=0
nCNOTi4(k)=0
nCNOTi3(k)=0
nCNOTi2(k)=0
nCNOTi1(k)=0
nCNOTi0(k)=0
nCNOSr14(k)=0
nCNOSr13(k)=0
nCNOSr12(k)=0
nCNOSr11(k)=0
nCNOSr10(k)=0
nCNOSr9(k)=0
nCNOSr8(k)=0
nCNOSr7(k)=0
nCNOSr6(k)=0
nCNOSr5(k)=0
nCNOSr4(k)=0
nCNOSr3(k)=0
nCNOSr2(k)=0
nCNOSr1(k)=0
nCNOSr0(k)=0
nCNTi8(k)=0
nCNTi7(k)=0
nCNTi6(k)=0
nCNTi5(k)=0
nCNTi4(k)=0
nCNTi3(k)=0
nCNTi2(k)=0
nCNTi1(k)=0
nCNTi0(k)=0
nCNSr14(k)=0
nCNSr13(k)=0
nCNSr12(k)=0
nCNSr11(k)=0
nCNSr10(k)=0
nCNSr9(k)=0
nCNSr8(k)=0
nCNSr7(k)=0
nCNSr6(k)=0
nCNSr5(k)=0
nCNSr4(k)=0
nCNSr3(k)=0
nCNSr2(k)=0
nCNSr1(k)=0
nCNSr0(k)=0
enddo
Nolayer1=0
Nolayer2=0
Nolayer3=0
Nolayer4=0
Nolayer5=0
```

```

Nolayer6=0
Nsrlayer1=0
Nsrlayer2=0
Nsrlayer3=0
Nsrlayer4=0
Nsrlayer5=0
Nsrlayer6=0
Ntilayer1=0
Ntilayer2=0
Ntilayer3=0
Ntilayer4=0
Ntilayer5=0
Ntilayer6=0
do i=1,natom
    iOTi(i)=0
    iOSr(i)=0
    iTiO(i)=0
    iSrO(i)=0
    if (layer(i).EQ.1) then
        if(kt(i).EQ.8) Nolayer1=Nolayer1+1
        if(kt(i).EQ.22) Ntilayer1=Ntilayer1+1
        if(kt(i).EQ.38) Nsrlayer1=Nsrlayer1+1
    elseif (layer(i).EQ.2) then
        if(kt(i).EQ.8) Nolayer2=Nolayer2+1
        if(kt(i).EQ.22) Ntilayer2=Ntilayer2+1
        if(kt(i).EQ.38) Nsrlayer2=Nsrlayer2+1
    elseif (layer(i).EQ.3) then
        if(kt(i).EQ.8) Nolayer3=Nolayer3+1
        if(kt(i).EQ.22) Ntilayer3=Ntilayer3+1
        if(kt(i).EQ.38) Nsrlayer3=Nsrlayer3+1
    elseif (layer(i).EQ.4) then
        if(kt(i).EQ.8) Nolayer4=Nolayer4+1
        if(kt(i).EQ.22) Ntilayer4=Ntilayer4+1
        if(kt(i).EQ.38) Nsrlayer4=Nsrlayer4+1
    elseif (layer(i).EQ.5) then
        if(kt(i).EQ.8) Nolayer5=Nolayer5+1
        if(kt(i).EQ.22) Ntilayer5=Ntilayer5+1
        if(kt(i).EQ.38) Nsrlayer5=Nsrlayer5+1
    elseif (layer(i).EQ.6) then
        if(kt(i).EQ.8) Nolayer6=Nolayer6+1
        if(kt(i).EQ.22) Ntilayer6=Ntilayer6+1
        if(kt(i).EQ.38) Nsrlayer6=Nsrlayer6+1
    endif
enddo

write(6,*)"
write(6,*)"Total Number of atoms of each type in layer1'
write(6,*)'O = ',Nolayer1,' Sr= ',Nsrlayer1,' Ti= ',Ntilayer1
write(6,*)"
write(6,*)"Total Number of atoms of each type in layer2'
write(6,*)'O = ',Nolayer2,' Sr= ',Nsrlayer2,' Ti= ',Ntilayer2
write(6,*)"
write(6,*)"Total Number of atoms of each type in layer3'
write(6,*)'O = ',Nolayer3,' Sr= ',Nsrlayer3,' Ti= ',Ntilayer3
write(6,*)"
write(6,*)"Total Number of atoms of each type in layer4'

```

```

write(6,*)'O = ',Nolayer4,' Sr= ',Nsrlayer4,' Ti= ',Ntilayer4
write(6,*)"
write(6,*)"Total Number of atoms of each type in layer5'
write(6,*)'O = ',Nolayer5,' Sr= ',Nsrlayer5,' Ti= ',Ntilayer5
write(6,*)"
write(6,*)"Total Number of atoms of each type in surface layer'
write(6,*)'O = ',Nolayer6,' Sr= ',Nsrlayer6,' Ti= ',Ntilayer6

c*****
c calculates the coordination of Oxygen with Sr and Ti
c*****
do lay=1,6
do i=1,natom
  if (layer(i).eq.lay) then
  if (kt(i).EQ.8)then
    nOTi(lay)=0          !
    nOSr(lay)=0         !
    count=0
    do j=1,natom
      if(layer(j).eq.lay) then
      if ((i.NE.j).AND.(kt(j).NE.8)) then
        dx=ABS(x(j)-x(i))
        dy=ABS(y(j)-y(i))
        dz=ABS(z(j)-z(i))
c      IF (dx.GT.0.5*ncellx) dx=ncellx-dx !PBC if looking at bulk
c      IF (dy.GT.0.5*ncelly) dy=ncelly-dy
c      IF (dz.GT.0.5*ncellz) dz=ncellz-dz
        temp=dx*dx+dy*dy+dz*dz
        dist=sqrt(temp)
        if (kt(j).EQ.22) then          !for O-Ti
          if (dist.LE.0.55*blat) then
            nOTi(lay)=nOTi(lay)+1
            iOTi(i)=iOTi(i)+1
          endif
        elseif (kt(j).eq.38) then      !for O-Sr
          if (dist.LE.0.80*blat) then
            nOSr(lay)=nOSr(lay)+1
            iOSr(i)=iOSr(i)+1
          endif
        endif
      endif
    endif
  enddo
  if (nOTi(lay).eq.8) nCNOTi8(lay)=nCNOTi8(lay)+1
  if (nOTi(lay).eq.7) nCNOTi7(lay)=nCNOTi7(lay)+1
  if (nOTi(lay).eq.6) nCNOTi6(lay)=nCNOTi6(lay)+1
  if (nOTi(lay).eq.5) nCNOTi5(lay)=nCNOTi5(lay)+1
  if (nOTi(lay).eq.4) nCNOTi4(lay)=nCNOTi4(lay)+1
  if (nOTi(lay).eq.3) nCNOTi3(lay)=nCNOTi3(lay)+1
  if (nOTi(lay).eq.2) nCNOTi2(lay)=nCNOTi2(lay)+1
  if (nOTi(lay).eq.1) nCNOTi1(lay)=nCNOTi1(lay)+1
  if (nOTi(lay).eq.0) nCNOTi0(lay)=nCNOTi0(lay)+1

  if (nOSr(lay).eq.14) nCNOSr14(lay)=nCNOSr14(lay)+1
  if (nOSr(lay).eq.13) nCNOSr13(lay)=nCNOSr13(lay)+1
  if (nOSr(lay).eq.12) nCNOSr12(lay)=nCNOSr12(lay)+1

```

```

if (nOSr(layer).eq.11) nCNOSr11(layer)=nCNOSr11(layer)+1
if (nOSr(layer).eq.10) nCNOSr10(layer)=nCNOSr10(layer)+1
if (nOSr(layer).eq.9) nCNOSr9(layer)=nCNOSr9(layer)+1
if (nOSr(layer).eq.8) nCNOSr8(layer)=nCNOSr8(layer)+1
if (nOSr(layer).eq.7) nCNOSr7(layer)=nCNOSr7(layer)+1
if (nOSr(layer).eq.6) nCNOSr6(layer)=nCNOSr6(layer)+1
if (nOSr(layer).eq.5) nCNOSr5(layer)=nCNOSr5(layer)+1
if (nOSr(layer).eq.4) nCNOSr4(layer)=nCNOSr4(layer)+1
if (nOSr(layer).eq.3) nCNOSr3(layer)=nCNOSr3(layer)+1
if (nOSr(layer).eq.2) nCNOSr2(layer)=nCNOSr2(layer)+1
if (nOSr(layer).eq.1) nCNOSr1(layer)=nCNOSr1(layer)+1
if (nOSr(layer).eq.0) nCNOSr0(layer)=nCNOSr0(layer)+1

elseif (kt(i).eq.22) then          li is a Ti
  nTiO(layer)=0
  do j=1,natom
    if (layer(j).eq.lay) then
      if ((i.NE.j).AND.(kt(j).NE.22)) then
        if (kt(j).EQ.8) then      !Ti-O
          dx=ABS(x(j)-x(i))
          dy=ABS(y(j)-y(i))
          dz=ABS(z(j)-z(i))
c          IF (dx.GT.0.5*ncellx) dx=ncellx-dx
c          IF (dy.GT.0.5*ncelly) dy=ncelly-dy
c          IF (dz.GT.0.5*ncellz) dz=ncellz-dz
          temp=dx*dx+dy*dy+dz*dz
          dist=sqrt(temp)
          if (dist.LE.0.55*blat) then
            nTiO(layer)=nTiO(layer)+1
            iTiO(i)=iTiO(i)+1
          endif
        endif
      endif
    endif
  enddo
  if (nTiO(layer).eq.8) nCNTi8(layer)=nCNTi8(layer)+1
  if (nTiO(layer).eq.7) nCNTi7(layer)=nCNTi7(layer)+1
  if (nTiO(layer).eq.6) nCNTi6(layer)=nCNTi6(layer)+1
  if (nTiO(layer).eq.5) nCNTi5(layer)=nCNTi5(layer)+1
  if (nTiO(layer).eq.4) nCNTi4(layer)=nCNTi4(layer)+1
  if (nTiO(layer).eq.3) nCNTi3(layer)=nCNTi3(layer)+1
  if (nTiO(layer).eq.2) nCNTi2(layer)=nCNTi2(layer)+1
  if (nTiO(layer).eq.1) nCNTi1(layer)=nCNTi1(layer)+1
  if (nTiO(layer).eq.0) nCNTi0(layer)=nCNTi0(layer)+1

c*****
elseif (kt(i).EQ.38)then          li is Sr
  nSrO(layer)=0
  do j=1,natom
    if (layer(j).eq.lay) then
      if ((i.NE.j).AND.(kt(j).NE.38)) then
        if (kt(j).EQ.8) then      ! Sr-O
          dx=ABS(x(j)-x(i))
          dy=ABS(y(j)-y(i))
          dz=ABS(z(j)-z(i))
c          IF (dx.GT.0.5*ncellx) dx=ncellx-dx

```

```

c      IF (dy.GT.0.5*ncelly) dy=ncelly-dy
c      IF (dz.GT.0.5*ncellz) dz=ncellz-dz
temp=dx*dx+dy*dy+dz*dz
dist=sqrt(temp)
if (dist.LE.0.80*blat) then
      nSrO(lay)=nSrO(lay)+1
      iSrO(i)=iSrO(i)+1
endif
endif
endif
endif
enddo
if (nSrO(lay).eq.14) nCNSr14(lay)=nCNSr14(lay)+1
if (nSrO(lay).eq.13) nCNSr13(lay)=nCNSr13(lay)+1
if (nSrO(lay).eq.12) nCNSr12(lay)=nCNSr12(lay)+1
if (nSrO(lay).eq.11) nCNSr11(lay)=nCNSr11(lay)+1
if (nSrO(lay).eq.10) nCNSr10(lay)=nCNSr10(lay)+1
if (nSrO(lay).eq.9) nCNSr9(lay)=nCNSr9(lay)+1
if (nSrO(lay).eq.8) nCNSr8(lay)=nCNSr8(lay)+1
if (nSrO(lay).eq.7) nCNSr7(lay)=nCNSr7(lay)+1
if (nSrO(lay).eq.6) nCNSr6(lay)=nCNSr6(lay)+1
if (nSrO(lay).eq.5) nCNSr5(lay)=nCNSr5(lay)+1
if (nSrO(lay).eq.4) nCNSr4(lay)=nCNSr4(lay)+1
if (nSrO(lay).eq.3) nCNSr3(lay)=nCNSr3(lay)+1
if (nSrO(lay).eq.2) nCNSr2(lay)=nCNSr2(lay)+1
if (nSrO(lay).eq.1) nCNSr1(lay)=nCNSr1(lay)+1
if (nSrO(lay).eq.0) nCNSr0(lay)=nCNSr0(lay)+1
endif
if((igo(i).eq.5).and.(ithermo(i).eq.0)) then
write(10,104)j,kt(i),x(i),y(i),z(i),
&      iOTi(i),iOSr(i),iTio(i),iSrO(i)
endif
endif
enddo

c*****
write(6,*)'layer ',lay
write(6,*)'Coordination of Oxy with Ti and Sr'
write(6,*) '# Ti 8 coordinated (around Oxy) = ',nCNOTi8(lay)
write(6,*) '# Ti 7 coordinated (around Oxy) = ',nCNOTi7(lay)
write(6,*) '# Ti 6 coordinated (around Oxy) = ',nCNOTi6(lay)
write(6,*) '# Ti 5 coordinated (around Oxy) = ',nCNOTi5(lay)
write(6,*) '# Ti 4 coordinated (around Oxy) = ',nCNOTi4(lay)
write(6,*) '# Ti 3 coordinated (around Oxy) = ',nCNOTi3(lay)
write(6,*) '# Ti 2 coordinated (around Oxy)** = ',nCNOTi2(lay)
write(6,*) '# Ti 1 coordinated (around Oxy) = ',nCNOTi1(lay)
write(6,*) '# unbonded Ti (around Oxy) = ',nCNOTi0(lay)

write(6,*) '# Sr 14 coordinated (around Oxy) = ',nCNOSr14(lay)
write(6,*) '# Sr 13 coordinated (around Oxy) = ',nCNOSr13(lay)
write(6,*) '# Sr 12 coordinated (around Oxy) = ',nCNOSr12(lay)
write(6,*) '# Sr 11 coordinated (around Oxy) = ',nCNOSr11(lay)
write(6,*) '# Sr 10 coordinated (around Oxy) = ',nCNOSr10(lay)
write(6,*) '# Sr 9 coordinated (around Oxy) = ',nCNOSr9(lay)
write(6,*) '# Sr 8 coordinated (around Oxy) = ',nCNOSr8(lay)
write(6,*) '# Sr 7 coordinated (around Oxy) = ',nCNOSr7(lay)

```

```

write(6,*) # Sr 6 coordinated (around Oxy) = ',nCNOsr6(layer)
write(6,*) # Sr 5 coordinated (around Oxy) = ',nCNOsr5(layer)
write(6,*) # Sr 4 coordinated (around Oxy)** = ',nCNOsr4(layer)
write(6,*) # Sr 3 coordinated (around Oxy) = ',nCNOsr3(layer)
write(6,*) # Sr 2 coordinated (around Oxy) = ',nCNOsr2(layer)
write(6,*) # Sr 1 coordinated (around Oxy) = ',nCNOsr1(layer)
write(6,*) # unbonded Sr (around Oxy) = ',nCNOsr0(layer)

write(6,*) ''
write(6,*)'Coordination of Ti with Oxygen'
write(6,*) # Ti 8 coordinated (Ti with Oxy) = ',nCNTi8(layer)
write(6,*) # Ti 7 coordinated (Ti with Oxy)= ',nCNTi7(layer)
write(6,*) # Ti 6 coordinated (Ti with Oxy)=** ',nCNTi6(layer)
write(6,*) # Ti 5 coordinated (Ti with Oxy)= ',nCNTi5(layer)
write(6,*) # Ti 4 coordinated (Ti with Oxy)= ',nCNTi4(layer)
write(6,*) # Ti 3 coordinated (Ti with Oxy)= ',nCNTi3(layer)
write(6,*) # Ti 2 coordinated (Ti with Oxy)= ',nCNTi2(layer)
write(6,*) # Ti 1 coordinated (Ti with Oxy)= ',nCNTi1(layer)
write(6,*) # unbonded Ti (Ti with Oxy)= ',nCNTi0(layer)
write(6,*) ''

write(6,*) ''
write(6,*)'Coordination of Sr with Oxygen'
write(6,*) # Sr 14 coordinated (Sr with Oxy)= ',nCNSr14(layer)
write(6,*) # Sr 13 coordinated (Sr with Oxy)= ',nCNSr13(layer)
write(6,*) # Sr 12 coordinated (Sr with Oxy)=** ',nCNSr12(layer)
write(6,*) # Sr 11 coordinated (Sr with Oxy)= ',nCNSr11(layer)
write(6,*) # Sr 10 coordinated (Sr with Oxy)= ',nCNSr10(layer)
write(6,*) # Sr 9 coordinated (Sr with Oxy)= ',nCNSr9(layer)
write(6,*) # Sr 8 coordinated (Sr with Oxy)= ',nCNSr8(layer)
write(6,*) # Sr 7 coordinated (Sr with Oxy)= ',nCNSr7(layer)
write(6,*) # Sr 6 coordinated (Sr with Oxy)= ',nCNSr6(layer)
write(6,*) # Sr 5 coordinated (Sr with Oxy)= ',nCNSr5(layer)
write(6,*) # Sr 4 coordinated (Sr with Oxy)= ',nCNSr4(layer)
write(6,*) # Sr 3 coordinated (Sr with Oxy)= ',nCNSr3(layer)
write(6,*) # Sr 2 coordinated (Sr with Oxy)= ',nCNSr2(layer)
write(6,*) # Sr 1 coordinated (Sr with Oxy)= ',nCNSr1(layer)
write(6,*) # unbonded Sr (Sr with Oxy)= ',nCNSr0(layer)
write(6,*) ''

enddo      !*****finished each layer

write(7,100)'O-Ti 6',float(nCNOTi6(6))/Nolayer6,
& float(nCNOTi6(1))/Nolayer1,
& float(nCNOTi6(2))/Nolayer2,float(nCNOTi6(3))/Nolayer3,
& float(nCNOTi6(4))/Nolayer4,float(nCNOTi6(5))/Nolayer5

write(7,100)'O-Ti 5',float(nCNOTi5(6))/Nolayer6,
& float(nCNOTi5(1))/Nolayer1,
& float(nCNOTi5(2))/Nolayer2,float(nCNOTi5(3))/Nolayer3,
& float(nCNOTi5(4))/Nolayer4,float(nCNOTi5(5))/Nolayer5

write(7,100)'O-Ti 4',float(nCNOTi4(6))/Nolayer6,
& float(nCNOTi4(1))/Nolayer1,
& float(nCNOTi4(2))/Nolayer2,float(nCNOTi4(3))/Nolayer3,
& float(nCNOTi4(4))/Nolayer4,float(nCNOTi4(5))/Nolayer5

```

```

write(7,100)'O-Ti 3',float(nCNOTi3(6))/Nolayer6,
& float(nCNOTi3(1))/Nolayer1,
& float(nCNOTi3(2))/Nolayer2,float(nCNOTi3(3))/Nolayer3,
& float(nCNOTi3(4))/Nolayer4,float(nCNOTi3(5))/Nolayer5

write(7,100)'O-Ti 2',float(nCNOTi2(6))/Nolayer6,
& float(nCNOTi2(1))/Nolayer1,
& float(nCNOTi2(2))/Nolayer2,float(nCNOTi2(3))/Nolayer3,
& float(nCNOTi2(4))/Nolayer4,float(nCNOTi2(5))/Nolayer5

write(7,100)'O-Ti 1',float(nCNOTi1(6))/Nolayer6,
& float(nCNOTi1(1))/Nolayer1,
& float(nCNOTi1(2))/Nolayer2,float(nCNOTi1(3))/Nolayer3,
& float(nCNOTi1(4))/Nolayer4,float(nCNOTi1(5))/Nolayer5

write(7,100)'O-Ti 0',float(nCNOTi0(6))/Nolayer6,
& float(nCNOTi0(1))/Nolayer1,
& float(nCNOTi0(2))/Nolayer2,float(nCNOTi0(3))/Nolayer3,
& float(nCNOTi0(4))/Nolayer4,float(nCNOTi0(5))/Nolayer5

write(7,*)'
write(7,101)'O-Sr 13',float(nCNOSr13(6))/Nolayer6,
& float(nCNOSr13(1))/Nolayer1,
& float(nCNOSr13(2))/Nolayer2,float(nCNOSr13(3))/Nolayer3,
& float(nCNOSr13(4))/Nolayer4,float(nCNOSr13(5))/Nolayer5

write(7,101)'O-Sr 12',float(nCNOSr12(6))/Nolayer6,
& float(nCNOSr12(1))/Nolayer1,
& float(nCNOSr12(2))/Nolayer2,float(nCNOSr12(3))/Nolayer3,
& float(nCNOSr12(4))/Nolayer4,float(nCNOSr12(5))/Nolayer5

write(7,101)'O-Sr 11',float(nCNOSr11(6))/Nolayer6,
& float(nCNOSr11(1))/Nolayer1,
& float(nCNOSr11(2))/Nolayer2,float(nCNOSr11(3))/Nolayer3,
& float(nCNOSr11(4))/Nolayer4,float(nCNOSr11(5))/Nolayer5

write(7,101)'O-Sr 10',float(nCNOSr10(6))/Nolayer6,
& float(nCNOSr10(1))/Nolayer1,
& float(nCNOSr10(2))/Nolayer2,float(nCNOSr10(3))/Nolayer3,
& float(nCNOSr10(4))/Nolayer4,float(nCNOSr10(5))/Nolayer5

write(7,101)'O-Sr 9',float(nCNOSr9(6))/Nolayer6,
& float(nCNOSr9(1))/Nolayer1,
& float(nCNOSr9(2))/Nolayer2,float(nCNOSr9(3))/Nolayer3,
& float(nCNOSr9(4))/Nolayer4,float(nCNOSr9(5))/Nolayer5

write(7,101)'O-Sr 8',float(nCNOSr8(6))/Nolayer6,
& float(nCNOSr8(1))/Nolayer1,
& float(nCNOSr8(2))/Nolayer2,float(nCNOSr8(3))/Nolayer3,
& float(nCNOSr8(4))/Nolayer4,float(nCNOSr8(5))/Nolayer5

write(7,101)'O-Sr 7',float(nCNOSr7(6))/Nolayer6,
& float(nCNOSr7(1))/Nolayer1,

```

& float(nCNOSr7(2))/Nolayer2,float(nCNOSr7(3))/Nolayer3,  
& float(nCNOSr7(4))/Nolayer4,float(nCNOSr7(5))/Nolayer5

write(7,101)'O-Sr 6',float(nCNOSr6(6))/Nolayer6,  
& float(nCNOSr6(1))/Nolayer1,  
& float(nCNOSr6(2))/Nolayer2,float(nCNOSr6(3))/Nolayer3,  
& float(nCNOSr6(4))/Nolayer4,float(nCNOSr6(5))/Nolayer5

write(7,101)'O-Sr 5',float(nCNOSr5(6))/Nolayer6,  
& float(nCNOSr5(1))/Nolayer1,  
& float(nCNOSr5(2))/Nolayer2,float(nCNOSr5(3))/Nolayer3,  
& float(nCNOSr5(4))/Nolayer4,float(nCNOSr5(5))/Nolayer5

write(7,101)'O-Sr 4',float(nCNOSr4(6))/Nolayer6,  
& float(nCNOSr4(1))/Nolayer1,  
& float(nCNOSr4(2))/Nolayer2,float(nCNOSr4(3))/Nolayer3,  
& float(nCNOSr4(4))/Nolayer4,float(nCNOSr4(5))/Nolayer5

write(7,101)'O-Sr 3',float(nCNOSr3(6))/Nolayer6,  
& float(nCNOSr3(1))/Nolayer1,  
& float(nCNOSr3(2))/Nolayer2,float(nCNOSr3(3))/Nolayer3,  
& float(nCNOSr3(4))/Nolayer4,float(nCNOSr3(5))/Nolayer5

write(7,101)'O-Sr 2',float(nCNOSr2(6))/Nolayer6,  
& float(nCNOSr2(1))/Nolayer1,  
& float(nCNOSr2(2))/Nolayer2,float(nCNOSr2(3))/Nolayer3,  
& float(nCNOSr2(4))/Nolayer4,float(nCNOSr2(5))/Nolayer5

write(7,101)'O-Sr 1',float(nCNOSr1(6))/Nolayer6,  
& float(nCNOSr1(1))/Nolayer1,  
& float(nCNOSr1(2))/Nolayer2,float(nCNOSr1(3))/Nolayer3,  
& float(nCNOSr1(4))/Nolayer4,float(nCNOSr1(5))/Nolayer5

write(7,101)'O-Sr 0',float(nCNOSr0(6))/Nolayer6,  
& float(nCNOSr0(1))/Nolayer1,  
& float(nCNOSr0(2))/Nolayer2,float(nCNOSr0(3))/Nolayer3,  
& float(nCNOSr0(4))/Nolayer4,float(nCNOSr0(5))/Nolayer5

write(7,\*)'

write(7,102)'Ti-O 8',float(nCNTi8(6))/Ntilayer6,  
& float(nCNTi8(1))/Ntilayer1,  
& float(nCNTi8(2))/Ntilayer2,float(nCNTi8(3))/Ntilayer3,  
& float(nCNTi8(4))/Ntilayer4,float(nCNTi8(5))/Ntilayer5

write(7,102)'Ti-O 7',float(nCNTi7(6))/Ntilayer6,  
& float(nCNTi7(1))/Ntilayer1,  
& float(nCNTi7(2))/Ntilayer2,float(nCNTi7(3))/Ntilayer3,  
& float(nCNTi7(4))/Ntilayer4,float(nCNTi7(5))/Ntilayer5

write(7,102)'Ti-O 6',float(nCNTi6(6))/Ntilayer6,  
& float(nCNTi6(1))/Ntilayer1,  
& float(nCNTi6(2))/Ntilayer2,float(nCNTi6(3))/Ntilayer3,  
& float(nCNTi6(4))/Ntilayer4,float(nCNTi6(5))/Ntilayer5

write(7,102)'Ti-O 5',float(nCNTi5(6))/Ntilayer6,  
& float(nCNTi5(1))/Ntilayer1,

```

& float(nCNTi5(2))/Ntilayer2,float(nCNTi5(3))/Ntilayer3,
& float(nCNTi5(4))/Ntilayer4,float(nCNTi5(5))/Ntilayer5

write(7,102)'Ti-O 4',float(nCNTi4(6))/Ntilayer6,
& float(nCNTi4(1))/Ntilayer1,
& float(nCNTi4(2))/Ntilayer2,float(nCNTi4(3))/Ntilayer3,
& float(nCNTi4(4))/Ntilayer4,float(nCNTi4(5))/Ntilayer5

write(7,102)'Ti-O 3',float(nCNTi3(6))/Ntilayer6,
& float(nCNTi3(1))/Ntilayer1,
& float(nCNTi3(2))/Ntilayer2,float(nCNTi3(3))/Ntilayer3,
& float(nCNTi3(4))/Ntilayer4,float(nCNTi3(5))/Ntilayer5

write(7,102)'Ti-O 2',float(nCNTi2(6))/Ntilayer6,
& float(nCNTi2(1))/Ntilayer1,
& float(nCNTi2(2))/Ntilayer2,float(nCNTi2(3))/Ntilayer3,
& float(nCNTi2(4))/Ntilayer4,float(nCNTi2(5))/Ntilayer5

write(7,*)'
write(7,103)'Sr-O 14',float(nCNSr14(6))/Nsrlayer6,
& float(nCNSr14(1))/Nsrlayer1,
& float(nCNSr14(2))/Nsrlayer2,float(nCNSr14(3))/Nsrlayer3,
& float(nCNSr14(4))/Nsrlayer4,float(nCNSr14(5))/Nsrlayer5

write(7,103)'Sr-O 13',float(nCNSr13(6))/Nsrlayer6,
& float(nCNSr13(1))/Nsrlayer1,
& float(nCNSr13(2))/Nsrlayer2,float(nCNSr13(3))/Nsrlayer3,
& float(nCNSr13(4))/Nsrlayer4,float(nCNSr13(5))/Nsrlayer5

write(7,103)'Sr-O 12',float(nCNSr12(6))/Nsrlayer6,
& float(nCNSr12(1))/Nsrlayer1,
& float(nCNSr12(2))/Nsrlayer2,float(nCNSr12(3))/Nsrlayer3,
& float(nCNSr12(4))/Nsrlayer4,float(nCNSr12(5))/Nsrlayer5

write(7,103)'Sr-O 11',float(nCNSr11(6))/Nsrlayer6,
& float(nCNSr11(1))/Nsrlayer1,
& float(nCNSr11(2))/Nsrlayer2,float(nCNSr11(3))/Nsrlayer3,
& float(nCNSr11(4))/Nsrlayer4,float(nCNSr11(5))/Nsrlayer5

write(7,103)'Sr-O 10',float(nCNSr10(6))/Nsrlayer6,
& float(nCNSr10(1))/Nsrlayer1,
& float(nCNSr10(2))/Nsrlayer2,float(nCNSr10(3))/Nsrlayer3,
& float(nCNSr10(4))/Nsrlayer4,float(nCNSr10(5))/Nsrlayer5

write(7,103)'Sr-O 9',float(nCNSr9(6))/Nsrlayer6,
& float(nCNSr9(1))/Nsrlayer1,
& float(nCNSr9(2))/Nsrlayer2,float(nCNSr9(3))/Nsrlayer3,
& float(nCNSr9(4))/Nsrlayer4,float(nCNSr9(5))/Nsrlayer5

write(7,103)'Sr-O 8',float(nCNSr8(6))/Nsrlayer6,
& float(nCNSr8(1))/Nsrlayer1,
& float(nCNSr8(2))/Nsrlayer2,float(nCNSr8(3))/Nsrlayer3,
& float(nCNSr8(4))/Nsrlayer4,float(nCNSr8(5))/Nsrlayer5

write(7,103)'Sr-O 7',float(nCNSr7(6))/Nsrlayer6,
& float(nCNSr7(1))/Nsrlayer1,

```

```

& float(nCNSr7(2))/Nsrlayer2,float(nCNSr7(3))/Nsrlayer3,
& float(nCNSr7(4))/Nsrlayer4,float(nCNSr7(5))/Nsrlayer5

write(7,103)'Sr-O 6',float(nCNSr6(6))/Nsrlayer6,
& float(nCNSr6(1))/Nsrlayer1,
& float(nCNSr6(2))/Nsrlayer2,float(nCNSr6(3))/Nsrlayer3,
& float(nCNSr6(4))/Nsrlayer4,float(nCNSr6(5))/Nsrlayer5

write(7,103)'Sr-O 5',float(nCNSr5(6))/Nsrlayer6,
& float(nCNSr5(1))/Nsrlayer1,
& float(nCNSr5(2))/Nsrlayer2,float(nCNSr5(3))/Nsrlayer3,
& float(nCNSr5(4))/Nsrlayer4,float(nCNSr5(5))/Nsrlayer5

write(7,103)'Sr-O 4',float(nCNSr4(6))/Nsrlayer6,
& float(nCNSr4(1))/Nsrlayer1,
& float(nCNSr4(2))/Nsrlayer2,float(nCNSr4(3))/Nsrlayer3,
& float(nCNSr4(4))/Nsrlayer4,float(nCNSr4(5))/Nsrlayer5

write(7,103)'Sr-O 3',float(nCNSr3(6))/Nsrlayer6,
& float(nCNSr3(1))/Nsrlayer1,
& float(nCNSr3(2))/Nsrlayer2,float(nCNSr3(3))/Nsrlayer3,
& float(nCNSr3(4))/Nsrlayer4,float(nCNSr3(5))/Nsrlayer5

100 format(1A6,1X,6F15.6)
101 format(1A6,1X,6F15.6)
102 format(1A6,1X,6F15.6)
103 format(1A6,1X,6F15.6)
104 format(i7,1x,i5,3(1x,f11.6),4(i5,1x))
c,5F15.6)

c100 format(1X,1X,5(I12,1X))
stop
end

```

## REFERENCE LIST

1. C. Zhou, D. M. News: Intrinsic dead layer effect and the performance of ferroelectric thin film capacitors. *Journal of Applied Physics* **82**, 3081 (1997).
2. F. Rinaldi: Basics of Molecular Beam Epitaxy (MBE), (Annual Report, Optoelectronics Department, University of Ulm, 2002) pp 1-8.
3. P. Petrov, E. F. Carlsson: Improved SrTiO<sub>3</sub> multilayers for microwave application: Growth and properties. *Journal of Applied Physics* **84**, 3134 (1998).
4. R. E. Treece, J. B. Thompson, C. H. Mueller, T. Riykin, M. W. Cromar: Optimization of SrTiO<sub>3</sub> for applications in tunableresonant circuits. *Applied Superconductivity, IEEE Transactions* **7**, 2363 (1997).
5. D. Roy, C. J. Peng, S. B. Krupanidhi: Excimer laser ablated strontium titanate thin films for dynamic random access memory applications. *Applied Physics Letters* **60**, 2478 (1992).
6. R. Tsuchiya, M. Kawasaki, H. Kubota, J. Nishino, H. Sato, H. Akoh, H. Koinuma: YBa<sub>2</sub>-Cu<sub>3</sub>O<sub>7</sub>-delta trilayer junction with nm thick PrGaO<sub>3</sub> barrier. *Applied Physics Letters* **71**, 1570 (1997).
7. E. Heifets, R. I. Eglitis, E. A. Kotomin, J. Maier, G. Borstel: First-Principles calculations for SrTiO<sub>3</sub>(100) surface structure. *Surface Science* **513**, 211 (2002).
8. T. Nakamura, H. Inada, M. Iiyama: In situ surface characterization of SrTiO<sub>3</sub>(100) substrates and homoepitaxial SrTiO<sub>3</sub> thin films grown by molecular beam epitaxy and pulsed laser deposition. *Applied Surface Science* **130-132**, 576 (1998).
9. A. G. Schrott, J. A. Misewich, M. Copel, D. W. Abraham, Y. Zhang: A-site surface termination in strontium titanate single crystals. *Applied Physics Letters* **79**, 1786 (2001).
10. D.-W. Kim, D.-H. Kim, B.-S. Kang, T. W. Noh, S. Shin, Z. G. Khim: Atomic control of homoepitaxial SrTiO<sub>3</sub> films using laser molecular beam epitaxy. *Physica C* **313**, 246 (1999).
11. A. J. Moulson, J. M. Herbert: *Electroceramics: Materials, Properties, Applications*, 2nd ed. (John Wiley & Sons Ltd, West Sussex, England, 2003), p 557.
12. R. A. Cowley: Lattice Dynamics and Phase Transitions of Strontium Titanate. *Physical Review* **134**, A981 (1964).
13. D. Vanderbilt: First-principles based modelling of ferroelectrics. *Current Opinion in Solid State & Materials Science* **2**, 701 (1997).

14. G. Shirane, Y. Yamada: Lattice-Dynamical Study of the 110K Phase Transition in SrTiO<sub>3</sub>. *Physical Review* **177**, 858 (1969).
15. T. Kubo, H. Nozoye: Surface structure of SrTiO<sub>3</sub> (100). *Surface Science* **542**, 177 (2003).
16. K. Szot, W. Speier, U. Breuer, R. Meyer, J. Szade, R. Waser: Formation of micro-crystals on the (100) surface of SrTiO<sub>3</sub> at elevated temperatures. *Surface Science* **460**, 112 (2000).
17. D. Roy, C. J. Peng, S. B. Krupanidhi: Excimer laser ablated strontium titanate thin films for dynamic random access memory applications. *Applied Physics Letters* **60**, 2478 (1992).
18. W. Wu, K. H. Wong, C. L. Choy: Epitaxial growth of SrTiO<sub>3</sub> films with different orientations on TiN buffered Si(001) by pulsed laser deposition. *Thin Solid Films* **360**, 103 (2000).
19. P. C. Joshi, S. B. Krupanidhi: Structural and electrical characteristics of SrTiO<sub>3</sub> thin films for dynamic random access memory applications. *Journal of Applied Physics* **73**, 7627 (1993).
20. Y. Kido, T. Nishimura, Y. Hoshino, H. Namba: Surface structures of SrTiO<sub>3</sub>(001) and Ni/SrTiO<sub>3</sub>(001) studied by medium-energy ion scattering and SR-photoelectron spectroscopy. *Nuclear Instruments and Methods in Physics Research B* **161-163**, 371 (2000).
21. D. Bao, H. Yang, L. Zhang, X. Yao: Structure and Optical Properties of SrTiO<sub>3</sub> Thin Films Prepared by a Sol-Gel Technique. *Physica Status Solidi (a)* **169**, 227 (1998).
22. O. Moran, R. Hott, D. Fuchs: Study of SrTiO<sub>3</sub> thin films grown by sputtering technique for tunnel barriers in quasiparticle injection contacts. *Thin Solid Films* **517**, 1908 (2009).
23. M. Lippmaa, K. Takahashi, A. Ohtomo, S. Ohashi, T. Ohnishi, N. Nakagawa, T. Sato, M. Iwatsuki, H. Koinuma, M. Kawasaki: Atom technology for Josephson tunnel junctions: SrTiO<sub>3</sub> substrate surface. *Materials Science and Engineering B* **56**, 111 (1998).
24. M. Matvejeff, T. Chikyow, M. Lippmaa: Interface growth of La<sub>1.2</sub>Sr<sub>1.8</sub>Mn<sub>1.7</sub>Ru<sub>0.3</sub>O<sub>7</sub> Ruddlesden-Popper films on SrTiO<sub>3</sub>. *Journal of Crystal Growth* **311**, 1201 (2009).
25. H. Asaoka, K. Saiki, A. Koma, H. Yamamoto: Heteroepitaxial growth of SrO on hydrogen-terminated Si(100) surface. *Thin Solid Films* **369**, 273 (2000).
26. C.-J. Xian, N.-J. Seong, S.-G. Yoon: Epitaxial SrRuO<sub>3</sub> Thin Films Deposited on SrO Buffered-Si(001) Substrates for Ferroelectric Pb(Zr<sub>0.2</sub>Ti<sub>0.8</sub>)O<sub>3</sub> Thin Films. *Metals and Materials International* **15**, 89 (2009).

27. J. Schwarzkopf, R. Fornari: Epitaxial growth of ferroelectric oxide films. *Progress in Crystal Growth and Characterization of Materials* **52**, 159 (2006).
28. R. W. G. Wyckoff: Crystal Structure (John Wiley & Sons, New York, London, 1963), Vol. 1.
29. K. I. Hadjiivanov, D. G. Klissurski: Surface Chemistry of Titania (Anatase) and Titania-supported Catalysts. *Chemical Society Reviews* **25**, 61 (1996).
30. S. Yamamoto, T. Sumita, T. Yamaki, A. Miyashita, H. Naramoto: Characterization of epitaxial TiO<sub>2</sub> films prepared by pulsed laser deposition. *Journal of Crystal Growth* **237-239**, 569 (2002).
31. M. Murakami, Y. Matsumoto, K. Nakajima, T. Makino, Y. Segawa, T. Chikyow, P. Ahmet, M. Kawasaki, H. Koinuma: Anatase TiO<sub>2</sub> thin films grown on lattice-matched LaAlO<sub>3</sub> substrate by laser molecular-beam epitaxy. *Applied Physics Letters* **78**, 2664 (2001).
32. N.-G. Park, J. v. d. Lagemaat, A. J. Frank: Comparison of Dye-Sensitized Rutile- and Anatase-Based TiO<sub>2</sub> Solar Cells. *Journal of Physical Chemistry B* **104**, 8989 (2000).
33. S.-H. Jeong, J.-K. Kim, B.-S. Kim, S.-H. Shim, B.-T. Lee: Characterization of SiO<sub>2</sub> and TiO<sub>2</sub> films prepared using rf magnetron sputtering and their application to anti-reflection coating. *Vacuum* **76**, 507 (2004).
34. W. Kern, K. K. Schuegraf, Deposition Technologies and Applications: Introduction and Overview in Handbook of Thin-Film Deposition Processes and Techniques - Principles, Methods, Equipment and Applications, 2nd ed. edited by K. Seshan (William Andrew Publishing, Noyes, 2002) pp 11-43.
35. J. Peña, A. Martinez, F. Conde, J. M. Gonzalez-Calbet, M. Vallet-Regi: In situ growth of SrTiO<sub>3</sub> thin films prepared by AACVD from strontium and titanium oxide bisdipivaloylmethanates. *Solid State Ionics* **101-103**, 183 (1997).
36. B.-C. Kang, S.-B. Lee, J.-H. Boo: Growth of TiO<sub>2</sub> thin films on Si(100) substrates using single molecular precursors by metal organic chemical vapor deposition. *Surface and Coatings Technology* **131**, 88 (2000).
37. J.-P. Lu, R. Raj: Ultra-high vacuum chemical vapor deposition and in situ characterization of titanium oxide thin films. *Journal of Materials Research* **6**, 1913 (1991).
38. H. O. Pierson, Handbook of Chemical Vapor Deposition: Principles, Technology and Applications, 2nd ed. (William Andrew Publishing, Noyes, 1999), pp 3-4.

39. H.-A. Durand, J.-H. Brimaud, O. Hellman, H. Shibata, S. Sakuragi, Y. Makita, D. Gesbert, P. Meyrueis: Excimer laser sputtering deposition of TiO<sub>2</sub> optical coating for solar cells. *Applied Surface Science* **86**, 122 (1995).
40. N. Martin, A. M. E. Santo, R. Sanjines, F. Levy: Energy distribution of ions bombarding TiO<sub>2</sub> thin films during sputter deposition. *Surface & Coatings Technology* **138**, 77 (2001).
41. L. D. Madsen, N. L. Johnson, S. N. Jacobsen, U. Helmersson, S. Rudner, I. Ivanov, L.-D. Wernlund, L. Ryen, E. Olsson: Structural and Electrical Characterization of Sputter-Deposited SrTiO<sub>3</sub> Thin Films. *Microelectronic Engineering* **29**, 123 (1995).
42. C.-Y. Liu, T.-Y. Tseng: Electrical properties of sputter deposited SrTiO<sub>3</sub> gate dielectrics. *Journal of the European Ceramic Society* **24**, 1449 (2004).
43. C. Li, Z. Zheng, F. Zhang, S. Yang, H. Wang, L. Chen, F. Zhang, X. Wang, X. Liu: TiO<sub>2-x</sub> films prepared by ion beam assisted deposition. *Nuclear Instruments and Methods in Physics Research B* **169**, 21 (2000).
44. D. P. Norton, D. H. Lowndes, J. D. Budai, B. C. Chakoumakos: Artificially-layered and metastable thin-film materials development utilizing pulsed-laser deposition. *Materials Science and Engineering B* **41**, 374 (1996).
45. J. Brannon: Excimer Laser Ablation and Etching, edited by W. Weed (AVS Monograph Series, The Education Committee American Vacuum Society, New York, 1993), pp 72-77.
46. J. M. Lackner: Industrially-styled room-temperature pulsed laser deposition of titanium-based coatings. *Vacuum* **78**, 73 (2005).
47. T. Ohnishi, M. Lippmaa, T. Yamamoto, S. Meguro, H. Koinuma: Improved stoichiometry and misfit control in perovskite thin film formation at a critical fluence by pulsed laser deposition. *Applied Physics Letters* **87**, 241919 (2005).
48. T. Ohnishi, K. Shibuya, T. Yamamoto, M. Lippmaa: Defects and transport in complex oxide thin films. *Journal of Applied Physics* **103**, 103703 (2008).
49. R. F. C. Farrow: Molecular Beam Epitaxy: Applications to Key Materials (William Andrew Publishing, Noyes, 1995), pp 505-532.
50. T. Hikita, T. Hanada, M. Kudo, M. Kawai: Surface structure of SrTiO<sub>3</sub>(001) with various surface treatments. *Journal of Vacuum Science and Technology A* **11**, 2649 (1993).
51. R. Takahashi, Y. Matsumoto, T. Ohsawa, M. Lippmaa, M. Kawasaki, H. Koinuma: Growth dynamics of the epitaxial SrO film on SrTiO<sub>3</sub>(001). *Journal of Crystal Growth* **234**, 505 (2002).

52. C. K. Ong, S. J. Wang: In situ RHEED monitor of the growth of epitaxial anatase TiO<sub>2</sub> thin films. *Applied Surface Science* **185**, 47 (2001).
53. T. Ohsawa, I. V. Lyubinetzky, M. A. Henderson, S. A. Chambers: Hole-Mediated Photodecomposition of Trimethyl Acetate on a TiO<sub>2</sub>(001) Anatase Epitaxial Thin Film Surface. *Journal of Physical Chemistry C* **112**, 20050 (2008).
54. M. C. Barnes, A. R. Gerson, S. Kumar, N.-M. Hwang: The mechanism of TiO<sub>2</sub> deposition by direct current magnetron reactive sputtering. *Thin Solid Films* **446**, 29 (2004).
55. A. N. Khodan, S. Guyard, J.-P. Contour, D.-G. Crete, E. Jacquet, K. Bouzouane: Pulsed Laser Deposition of epitaxial SrTiO<sub>3</sub> films: Growth, structure and functional properties. *Thin Solid Films* **515**, 6422 (2007).
56. A. Ohtomo, H. Y. Hwang: Growth mode control of the free carrier density in SrTiO<sub>3</sub> films. *Journal of Applied Physics* **102**, 083704 (2007).
57. M. Kubo, Y. Oumi, R. Miura, A. Stirling, A. Miyamoto, M. Kawasaki, M. Yoshimoto, H. Koinuma: Atomic control of layer-by-layer epitaxial growth on SrTiO<sub>3</sub>(001): Molecular-dynamics simulations. *Physical Review B* **56**, 13535 (1997).
58. N. Baguer, V. Georgieva, L. Calderin, I. T. Todorov, S. V. Gils, A. Bogaerts: Study of the nucleation and growth of TiO<sub>2</sub> and ZnO thin films by means of molecular dynamics simulations. *Journal of Crystal Growth* **Accepted Manuscript**, doi:10.1016/j.jcrysgro.2009.06.034 (2009).
59. A. Miyamoto, K. Takeichi, T. Hattori, M. Kubo, T. Inui: Mechanism of Layer-by-layer Homoepitaxial Growth of SrTiO<sub>3</sub> (100) as Investigated by Molecular Dynamics and Computer Graphics. *Japanese Journal of Applied Physics* **31**, 4463 (1992).
60. E. I. Tochitsky, R. N. Gritskevich, V. E. Obukhov: Structure and adhesion of vapour deposits, partially ionized vapour deposits, cluster deposits and partially ionized cluster deposits. *Thin Solid Films* **131**, 289 (1985).
61. H. Bönnemann, K. S. Nagabhushana, B. Corain, G. Schmid, N. Toshima: Metal Nanoclusters: Synthesis and Strategies for their Size Control in Metal Nanoclusters in Catalysis and Materials Science (Elsevier, Amsterdam, 2008), pp 21-48.
62. S. C. Hendy, B. D. Hall: Molecular dynamics simulations of lead clusters. *Physical Review B* **64**, 085425 (2001).
63. T. T. Jarvi, A. Kuronen, K. Meinander, K. Nordlund, K. Albe: Contact epitaxy by deposition of Cu, Ag, Au, Pt, and Ni nanoclusters on (100) surfaces: Size limits and mechanisms. *Physical Review B* **75**, 115422 (2007).

64. K. Nordlund, T. T. Jarvi, K. Meinander, J. Samela: Cluster ion-solid interactions from meV to MeV energies. *Applied Physics A: Materials Science & Processing* **91**, 561 (2008).
65. R. Y. Rubinstein, D. P. Kroese: Simulation and the Monte Carlo Method, 2nd ed. (John Wiley & Sons, Inc., Hoboken, New Jersey, 2007), p 345.
66. J. A. Purton, G. D. Barrera, N. L. Allan, J. D. Blundy: Monte Carlo and Hybrid Monte Carlo/Molecular Dynamics Approaches to Order-Disorder in Alloys, Oxides, and Silicates. *Journal of Physical Chemistry B* **102**, 5202 (1998).
67. J.-i. Takano, O. Takai, Y. Kogure, M. Doyama: Molecular dynamics, Monte Carlo and their hybrid methods: applications to thin film growth dynamics. *Thin Solid Films* **334**, 209 (1998).
68. A. F. Voter, Introduction to the Kinetic Monte Carlo Method in Radiation Effects in Solids, edited by K. E. Sickafus, E. A. Kotomin (Springer, NATO Publishing Unit: Dordrecht, The Netherlands, 2005), pp 1-24.
69. A. F. Voter, F. Montalenti, T. C. Germann: Extending the time scale in atomistic simulation of materials. *Annual Review of Materials Research* **32**, 321 (2002).
70. Q. Zhang, J. Zhu, J. Tan, G. Yu, J. Wu, J. Zhu, D. Xiao: Monte Carlo simulation of the growth of SrTiO<sub>3</sub> thin film with molecular source. *Vacuum* **81**, 539 (2006).
71. C. H. Grein, R. Benedek, T. d. I. Rubia: Epitaxial growth simulation employing a combined molecular dynamics and Monte Carlo approach. *Computational Materials Science* **6**, 123 (1996).
72. N. Metropolis, A. W. Rosenbluth, M. N. Rosenbluth, A. H. Teller, E. Teller: Equation of State Calculations by Fast Computing Machines. *Journal of Chemical Physics* **21**, 1087 (1953).
73. L. Guan, D. Zhang, X. Li, Z. Li: Role of pulse repetition rate in film growth of pulsed laser deposition. *Nuclear Instruments & Methods in Physics Research, Section B: Beam Interactions with Materials and Atoms* **266**, 57 (2008).
74. X. H. Xu, R. Q. Zhang, X. Z. Dong, G. A. Gehring: A study of the optimization of parameters for pulsed laser deposition using Monte Carlo simulation. *Thin Solid Films* **515**, 2754 (2006).
75. X. Tan, Y. C. Zhou, X. J. Zheng: Dependence of morphology of pulsed-laser deposited coatings on temperature: a kinetic Monte Carlo Simulation. *Surface and Coatings Technology* **197**, 288 (2005).

76. C.-C. Chou, M. L. Falk: Multiscale diffusion Monte Carlo simulation of epitaxial growth. *Journal of Computational Physics* **217**, 519 (2006).
77. L. Wang, P. Clancy: Kinetic Monte Carlo simulation of the growth of polycrystalline Cu films. *Surface Science* **473**, 25 (2001).
78. H. Huang, G. H. Gilmer, T. D. d. I. Rubia: An atomistic simulator for film deposition in three dimensions. *Journal of Applied Physics* **84**, 3636 (1998).
79. S. W. Levine, J. R. Engstrom, P. Clancy: A kinetic Monte Carlo study of the growth of Si on Si(100) at varying angles of incident deposition. *Surface Science* **401**, 112 (1998).
80. X.-j. Zheng, B. Yang, Z. Zhu, B. Wu, Y.-l. Mao: Kinetic Monte Carlo simulation of growth of BaTiO<sub>3</sub> thin film via pulsed laser deposition. *Transactions of Nonferrous Metals Society of China* **17**, 1441 (2007).
81. P. J. Feibelman: Diffusion Path for an Al Adatom on Al (001). *Physical Review Letters* **65**, 729 (1990).
82. A. F. Voter: A method for accelerating the molecular dynamics simulation of infrequent events. *Journal of Chemical Physics* **106**, 4655 (1997).
83. S. Pal, K. A. Fichthorn: Accelerated molecular dynamics of infrequent events. *Chemical Engineering Journal* **74**, (1999).
84. D. Hamelberg, J. Mongan, J. A. McCammon: Accelerated molecular dynamics: A promising and efficient simulation method for biomolecules. *Journal of Chemical Physics* **120**, 11919 (2004).
85. S. Birner, J. Kim, D. A. Richie, J. W. Wilkins, A. F. Voter, T. Lenosky: Accelerated dynamics simulations of interstitial-cluster growth. *Solid State Communications* **120**, 279 (2001).
86. M. Kubo, Y. Oumi, R. Miura, A. Stirling, A. Miyamoto, M. Kawasaki, M. Yoshimoto, H. Koinuma: Molecular dynamics simulation on a layer-by-layer homoepitaxial growth process of SrTiO<sub>3</sub>(001). *Journal of Chemical Physics* **109**, 8601 (1998).
87. J. H. Neave, P. J. Dobson, B. A. Joyce, J. Zhang: Reflection high-energy electron diffraction oscillations from vicinal surfaces--a new approach to surface diffusion measurements. *Applied Physics Letters* **47**, 100 (1985).
88. D. D. Vvedensky, S. Clarke: Recovery kinetics during interrupted epitaxial growth. *Surface Science* **225**, 373 (1990).
89. Z. Zhu, X. J. Zheng, W. Li: Kinetic Monte Carlo simulation of RHEED from BaTiO<sub>3</sub> thin films. *Physica B: Condensed Matter* **403**, 4074 (2008).

90. G. H. Gilmer, H. Huang, C. Roland: Thin film deposition: fundamentals and modeling. *Computational Materials Science* **12**, 354 (1998).
91. Z. Zhang, M. G. Lagally: Atomistic Processes in the Early Stages of Thin-Film Growth. *Science* **276**, 377 (1997).
92. Y. R. Li, J. L. Li, Y. Zhang, X. H. Wei, X. W. Deng, X. Z. Liu: Control of growth mode in SrTiO<sub>3</sub> homoepitaxy under 500C. *Journal of Applied Physics* **96**, 1640 (2004).
93. J. H. Song, Y. H. Jeong: SrTiO<sub>3</sub> homoepitaxy by the pulsed laser deposition method: island, layer-by-layer, and step-flow growth. *Solid State Communications* **125**, 563 (2003).
94. M. Lippmaa, N. Nakagawa, M. Kawasaki, S. Ohashi, H. Koinuma: Growth mode mapping of SrTiO<sub>3</sub> epitaxy. *Applied Physics Letters* **76**, 2439 (2000).
95. Y. Y. Tse, Y. Koutsonas, T. J. Jackson, G. Passerieux, I. P. Jones: Microstructure of homoepitaxial strontium titanate films grown by pulsed laser deposition. *Thin Solid Films* **515**, 1788 (2006).
96. B. J. Alder, T. E. Wainwright: Phase transition for a Hard Sphere System. *Journal of Chemical Physics* **27**, 1208 (1957).
97. G. Sutmann: Classical Molecular Dynamics in Quantum Simulations of Complex Many-Body Systems: From Theory to Algorithms, edited by J. Grotendorst, D. Marx, A. Muramatsu (John von Neumann Institute for Computing, Julich, 2002), pp 211-254.
98. W. K. Liu, E. G. Karpov, S. Zhang, H. S. Park: An introduction to computational nanomechanics and materials. *Computer Methods in Applied Mechanics and Engineering* **193**, 1529 (2004).
99. J. Li: Basic Molecular Dynamics in Handbook of materials modeling, edited by S. Yip (Springer, Dordrecht, The Netherlands, 2005), p 256.
100. M. P. Allen, D. J. Tildesley: Computer Simulation of Liquids (Oxford University Press Inc., New York, 1987), pp 155-162.
101. M. P. Allen, D. J. Tildesley: Computer Simulation of Liquids (Oxford University Press Inc., New York, 1987), pp 73-83.
102. A. D. Buckingham: Intermolecular Forces. *Philosophical Transactions of the Royal Society of London, Series B, Biological Sciences* **272**, 5 (1975).
103. M. A. McCoy, R. W. Grimes, W. E. Lee: Phase stability and interfacial structures in the SrO-SrTiO<sub>3</sub> system. *Philosophical Magazine A* **75**, 833 (1997).

104. J. D. Gale: Interatomic potential models for ionic materials in Handbook of materials modeling, edited by S. Yip (Springer, Dordrecht, The Netherlands, 2005), pp 479-497.
105. S. Sekiguchi, M. Fujimoto, M. Nomura, S.-B. Cho, J. Tanaka, T. Nishihara, M.-G. Kang, H.-H. Park: Atomic force microscopic observation of SrTiO<sub>3</sub> polar surface. *Solid State Ionics* **108**, 73 (1998).
106. P. Ewald: Die Berechnung optischer und elektrostatischer Gitterpotentiale. *Annals of Physics* **64**, 253 (1921).
107. D. Wolf, P. Keblinski, S. R. Phillpot, J. Eggebrecht: Exact method for the simulation of Coulombic systems by spherically truncated, pairwise  $r^{-1}$  summation. *Journal of Chemical Physics* **110**, 8254 (1999).
108. V. Swamy, J. D. Gale, L. S. Dubrovinsky: Atomistic simulation of the crystal structures and bulk moduli of TiO<sub>2</sub> polymorphs. *Journal of Physics and Chemistry of Solids* **62**, 887 (2001).
109. K. Lagarec, S. Desgreniers: Raman study of single crystal anatase TiO<sub>2</sub> up to 70 GPa. *Solid State Communications* **94**, 519 (1995).
110. F. Z. Aoumeur-Benkabou, B. Belgoumene: Structural and dynamical properties of SrO in the rock-salt phase. *Calphad* **28**, 65 (2004).
111. M. Lazzeri, A. Vittadini, A. Selloni: Structure and energetics of stoichiometric TiO<sub>2</sub> anatase surfaces. *Physical Review B* **63**, 155409 (2001).
112. N. V. Skorodumova, K. Hermansson, B. Johansson: Structural and electronic properties of the (100) surface and bulk of alkaline-earth metal oxides. *Physical Review B* **72**, 125414 (2005).
113. P. R. Son, R. A. Bartels: CaO and SrO single crystal elastic constants and their pressure derivatives. *Journal of Physics and Chemistry of Solids* **33**, 819 (1972).
114. P. Cortona, A. V. Monteleone: *Ab initio* calculations of cohesive and structural properties of the alkali-earth oxides. *Journal of Physics: Condensed Matter* **8**, 8983 (1996).
115. G. Cappellini, F. Finocchi, S. Bouette-Russo, C. Noguera: Ground-state properties and excitation energies of cubic SrO and MgO. *Computational Materials Science* **20**, 401 (2001).
116. B. P. Uberuaga, A. F. Voter: Accelerated Molecular Dynamics Methods in Radiation Effects in Solids, edited by K. E. Sickafus, E. A. Kotomin (Springer, Dordrecht, The Netherlands, 2007), pp 25-43.

117. M. R. Sorensen, A. F. Voter: Temperature-accelerated dynamics for simulation of infrequent events. *Journal of Chemical Physics* **112**, 9599 (2000).
118. A. F. Voter: Parallel replica method for dynamics of infrequent events. *Physical Review B* **57**, R13985 (1998).
119. L. T. Kong, L. J. Lewis: Transition state theory of the preexponential factors for self-diffusion on Cu, Ag, and Ni surfaces. *Physical Review B* **74**, 073412 (2006).
120. H. Yildirim, A. Kara, S. Durukanoglu, T. S. Rahman: Calculated pre-exponential factors and energetics for adatom hopping on terraces and steps of Cu(100) and Cu(110). *Surface Science* **600**, 484 (2006).
121. B. P. Uberuaga, F. Montalenti, T. C. Germann, A. F. Voter: Accelerated Molecular Dynamics Methods in Handbook of Materials Modeling, edited by S. Yip (Springer, Dordrecht, The Netherlands, 2005), pp 629-648.
122. J. L. Wohlwend, R. K. Behera, I. Jang, S. R. Phillpot, S. B. Sinnott: Morphology and Growth Modes of Metal-Oxides Deposited on SrTiO<sub>3</sub>. *Surface Science* **603**, 873 (2009).
123. R. J. Kennedy, P. A. Stampe: The influence of lattice mismatch and film thickness on the growth of TiO<sub>2</sub> on LaAlO<sub>3</sub> and SrTiO<sub>3</sub> substrates. *Journal of Crystal Growth* **252**, 333 (2003).
124. P. Fisher, O. Maksimov, H. Du, V. D. Heydemann, M. Skowronski, P. A. Salvador: Growth, structure, and morphology of TiO<sub>2</sub> films deposited by molecular beam epitaxy in pure ozone ambients. *Microelectronics Journal* **37**, 1493 (2006).
125. C. K. Ong, S. J. Wang: In situ RHEED monitor of the growth of epitaxial anatase TiO<sub>2</sub> thin films. *Applied Surface Science* **185**, 47 (2001).
126. S. H. Cheung, P. Nachimuthu, M. H. Engelhard, C. M. Wang, S. A. Chambers: N incorporation, composition and electronic structure in N-doped TiO<sub>2</sub>(001) anatase epitaxial films grown on LaAlO<sub>3</sub>(001). *Surface Science* **602**, 133 (2008).
127. S. A. Chambers, C. M. Wang, S. Thevuthasan, T. Droubay, D. E. McCready, A. S. Lea, V. Shutthanandan, C. F. W. Jr: Epitaxial growth and properties of MBE-grown ferromagnetic Co-doped TiO<sub>2</sub> anatase films on SrTiO<sub>3</sub>(001) and LaAlO<sub>3</sub>(001). *Thin Solid Films* **418**, 197 (2002).
128. G. Koster, G. Rijnders, D. H. A. Blank, H. Rogalla: Surface morphology determined by (001) single-crystal SrTiO<sub>3</sub> termination. *Physica C* **339**, 215 (2000).
129. L. Liu, H. Lu, Y. Fei, H. Guo, W. Xiang, Z. Chen: Formation of atomically smooth surfaces on SrTiO<sub>3</sub> substrates for epitaxial film growth. *Journal of Crystal Growth* **253**, 374 (2003).

130. D. H. A. Blank, G. Rijnders, G. Koster, H. Rogalla: In-situ monitoring during pulsed laser deposition using RHEED at high pressure. *Applied Surface Science* **127-129**, 633 (1998).
131. Y. R. Li, S. W. Jiang, Y. Zhang, X. W. Deng, X. H. Wei: Surface diffusion during layer growth of SrTiO<sub>3</sub> films with pulsed laser molecular beam epitaxy. *Journal of Crystal Growth* **278**, 629 (2005).
132. E. Giglio, P.-G. Reinhard, E. Suraud: Semiclassical approach to metal cluster dynamics. *Journal of Physics B: Atomic, Molecular and Optical Physics* **33**, L333 (2000).
133. N. Tanaka, D. L. Peng, K. Sumiyama, T. Hihara: Structural and optical properties of Ti oxide cluster-assembled films prepared by plasma-gas-condensation. *Thin Solid Films* **516**, 1677 (2008).
134. Y. Li, E. Blaisten-Barojas, D. A. Papaconstantopoulos: Structure and dynamics of alkali-metal clusters and fission of highly charged clusters. *Physical Review B* **57**, 15519 (1998).
135. U. Kreibig, H. Bonnemann, J. Hormes: Nanostructured Metal Clusters and Colloids in Handbook of Surfaces and Interfaces of Materials, edited by H. S. Nalwa (Academic Press, San Diego, California, 2001) Vol. 3, pp 1-85.
136. V. N. Popok, S. V. Prasalovich, E. E. B. Campbell: Surface nanostructuring by implantation of cluster ions. *Vacuum* **76**, 265 (2004).
137. C.-C. Chang, P. H. Kydd, S. L. Bernasek, H. A. Rabitz: Interactions of energetic clusters with surfaces at glancing incidence. *Surface Science* **239**, 333 (1990).
138. G. Geneste, J. Morillo, F. Finocchi: Ab initio study of Mg adatom and MgO molecule adsorption and diffusion on the MgO (001) surface. *Applied Surface Science* **188**, 122 (2002).
139. C. Li, R. Wu, A. J. Freeman, C. L. Fu: Energetics, bonding mechanism, and electronic structure of metal-ceramic interfaces: Ag/MgO(001). *Physical Review B* **48**, 8317 (1993).
140. T. E. Karakasidis, D. G. Papageorgiou, G. A. Evangelakis: Structure and dynamics of NiO(001) and Ni/NiO(001) surfaces by molecular dynamics simulation. *Applied Surface Science* **162-163**, 233 (2000).
141. U. Kurpick, T. S. Rahman: Diffusion processes and pre-exponential factors in homo-epitaxial growth on Ag(100). *Materials Research Society Symposia Proceedings* **492**, 263 (1998).

142. G. Henkelman, B. P. Uberuaga, D. J. Harris, J. H. Harding, N. L. Allan: MgO addimer diffusion on MgO(100): A comparison of *ab initio* and empirical models. *Physical Review B* **72**, 115437 (2005).
143. G. L. Kellogg, P. J. Feibelman: Surface self-diffusion on Pt(001) by an atomic exchange mechanism. *Physical Review Letters* **64**, 3143 (1990).
144. T. E. Karakasidis, E. Vamvakopoulos: Ni<sup>3+</sup> adsorbate dynamics on a NiO(001) surface. *Surface Science* **600**, 1952 (2006).

## BIOGRAPHICAL SKETCH

Jennifer Wohlwend was born and predominately raised in Summerville, South Carolina. She attended Clemson University in Clemson, South Carolina where she attained a Bachelor of Science in ceramic and materials science and engineering, in 2004. In the fall of 2004, she arrived at the University of Florida under the advisory of Dr. Susan B. Sinnott and became part of the Computational Materials Science Focus Group (CMSFG). Jennifer worked on the simulation of particulate and cluster deposition of SrTiO<sub>3</sub>.